Karlsruhe Institute of Technology

IONISATION MECHANISMS OF ^{206}PB INDUCED RYDBERG ATOMS

MSc thesis D.Hinz by

Dominic Fabian Hinz

at the Department of Physics
Institute of Experimental Particle Physics (ETP)

Reviewer:	Prof. Dr. Guido Drexlin
Second reviewer:	Prof. Dr. Christian Weinheimer
Advisor:	Dr. Florian Fränkle

1st November 2017 – 31st October 2018

Fakultät für Physik
Karlsruher Institut für Technologie
Wolfgang-Gaede-Str. 1
76131 Karlsruhe

I declare that I have developed and written the enclosed thesis completely by myself, and have not used sources or means without declaration in the text.

Karlsruhe, 29th October 2018 . . . .
(**Dominic Fabian Hinz**)

Accepted as **examination exemplar**.

Karlsruhe, 29th October 2018 . . . .
(**Prof. Dr. Guido Drexlin**)

Abstract

The **Ka**rlsruhe **Tri**tium **N**eutrino experiment (KATRIN) aims to measure the effective mass of the electron anti neutrino in a model-independent way by precise determination of the electron kinematics from tritium β decays. This task will be achieved by a windowless gaseous tritium source of high luminosity paired with a high resolution MAC-E filter spectrometer system. To achieve the sensitivity of $0.2\,\mathrm{eV/c^2}$ on the effective neutrino mass, knowledge of statistical and systematic uncertainties as well as the verification of background processes is essential. The sensitivity of the KATRIN experiment is currently limited by an higher than anticipated background, therefore, an understanding of the remaining background processes is of high relevance.

Previous measurements revealed features of the remaining background processes, whose characteristics are not consistent with previously observed ones. Based on the small dependence on the inner electrode potential, and the independence on pressure and magnetic field, a novel background model had to be developed.

The KATRIN main spectrometer was exposed to ambient air for several years during the installation of the inner wire electrode system. During this time, the inner surface of the spectrometer was contaminated by daughter isotopes of the naturally occurring ^{222}Rn isotope. Of particular interest is ^{210}Pb which has a half-life of about 22 years. The activity of ^{210}Pb is estimated to be on the order of 1 kBq and its decay in the main spectrometer vessel wall causes the sputtering of atoms by the generated recoil ion $^{206}\mathrm{Pb}^{2+}$, propagating through the material. The background events from the inner main spectrometer surface are correlated with the background events within the entire volume. To give rise to this correlation, a neutral messenger must be formed, which can pass unhindered by the inner electrodes into the spectrometer volume and release electrons via homogeneously distributed ionisation.

These messenger particles are assumed to be Rydberg atoms, highly excited atoms with long lifetimes, which are ionised by black body radiation (BBR) or collisions with residual gas atoms. The Rydberg background model combines the implications of intrinsic radioactivity by ^{210}Pb with the sputtering of atoms in Rydberg states as the assumed main background contribution.

This thesis focuses on the theoretical description of sputtering by ions from the main spectrometer vessel wall and different ionisation mechanisms of Rydberg atoms. The consideration of the surface treatment leads to a model of the chemical composition of the main spectrometer steel and its passivation layer. Completed by sputtering simulation with the SRIM code, which allows derivation of the characteristics of the sputtered atoms such as their kinematics, conclusions for the Rydberg background model are also drawn.

Indirect measurements of the initial energy spectrum of background electrons in the volume of the spectrometer showed higher than expected energies on the order of several eV. BBR-induced ionisation of highly excited atoms is not sufficient as a production mechanism, since electron energies of up to only 0.2 eV are possible. Therefore, other, more unusual, ionisation mechanisms of these excited atoms are considered in this thesis. For this purpose, Penning ionisation, ionisation by electric and magnetic fields, as well as autoionization are investigated. It was discovered that in fact no ionisation mechanism is appropriate, except for the less likely configuration of planetary atoms. These doubly highly excited atoms might be long-living if their outer electrons are in a non-resonant-interacting ensemble. Due to radiative transitions the electrons can reach a resonant state and the atom or molecule dissociates with electron emission.

In order to further examine the Rydberg background model, measurements with a radioactive ^{223}Ra source were performed. Rydberg-induced background has to be investigated directly at the radium source and also from the deliberate contamination of the inner spectrometer surface by short-living isotopes from the ^{223}Ra decay chain. However, radon emanation from the radium source was much higher than anticipated. Therefore, the Rydberg background could only be studied after closing the valve to the radium source by observing the natural decay of the induced radioactivity inside the main spectrometer. The measurement time was limited because the longest half-life of any daughter isotope is about 36 minutes. Nevertheless, the activation saturation of surface contamination by volume radioactivity of emanating radon was observed, as well as the background rate dependency on the inner electrode potential of the induced background. These measurements showed background behaviour like that of the remaining KATRIN background and therefore showed conclusively that processes following the decay of ^{210}Pb at the inner surface of the main spectrometer are responsible for the remaining background in the KATRIN experiment.

Zusammenfassung

Das **Ka**rlsruhe **Tri**tium **N**eutrino Experiment misst modell-unabhängig die effektive Neutrinomasse des Elektronantineutrinos, indem die Kinematik von Elektronen aus Tritium β-Zerfällen präzise bestimmt wird. Dies wird mithilfe einer fensterlosen gasförmigen Tritiumquelle von hoher Luminosität, gepaart mit einem hochauflösenden MAC-E-Filter-Spektrometersystem erreicht. Um die Sensitivität von $0{,}2\,\mathrm{eV}/c^2$ auf die effektive Neutrinomasse zu erreichen, ist die Kenntnis über die statistischen und systematischen Fehler sowie die Verifizierung der Untergrundprozesse unabdingbar. Die Sensitivität des KATRIN Experiments ist momentan durch Untergrund, der höher ist als erwartet, limitiert, weshalb das Verständnis über die vorherrschenden Untergrundprozesse von großer Bedeutung ist.

Frühere Messungen haben Merkmale dieser vorherrschenden Untergrundprozesse offenbart, deren Charakteristik allerdings nicht mit den Erwartungen aus früheren Experimenten übereinstimmt. Basierend auf der geringen Abhängigkeit von dem Potential der inneren Elektrode und der Unabhängigkeit von Druck und magnetischem Feld musste ein neues Untergrundmodell entwickelt werden.

Das KATRIN Hauptspektrometer war für einige Jahre, während des Einbaus der inneren Drahtelektrode, der Umgebungsluft ausgesetzt. Währenddessen wurde die innere Oberfläche mit Tochterisotopen des natürlich vorkommenden ^{222}Rn kontaminiert. Von besonderem Interesse ist hierbei ^{210}Pb mit einer Halbwertszeit von 22 Jahren. Die ^{210}Pb-Aktivität wird auf 1 kBq geschätzt und dessen radioaktiver Zerfall in der Hauptspektrometeroberfläche führt zur Zerstäubung von Atomen durch das entstehende Rückstoßion $^{206}\mathrm{Pb}^{2+}$, welches durch das Material propagiert. Die Untergrundereignisse von der inneren Oberfläche stehen in direktem Zusammenhang mit denen im gesamten Volumen. Um diese Korrelation zu erklären, bedarf es einem neutralen Boten, der die innere Elektrode nahezu ungehindert passieren kann und innerhalb des Spektrometervolumens, über homogen verteilte Ionisation, Elektronen freisetzt.

Es wird angenommen, dass diese neutralen Boten Rydbergatome sind, hoch angeregte Atome mit langer Lebenszeit, die über Wechselwirkung mit der Schwarzkörperstrahlung (BBR) oder über Kollisionen mit Restgasatomen ionisieren. Das Rydberguntergrundmodell kombiniert die Implikationen der intrinsischen ^{210}Pb Radioaktivität mit der Zerstäubung von Atomen in Rydbergzustände zu dem angenommenen Hauptuntergrundbeitrag.

Diese Arbeit bezieht sich auf die theoretische Beschreibung der Zerstäubung von Atomen aus der Hauptspektrometeroberfläche und verschiedenen Ionisationsmechanismen von Rydbergatomen. Unter Berücksichtigung der Oberflächenbehandlung wird ein Modell der chemischen Zusammensetzung des Hauptspektrometerstahls und dessen Passivierungsschicht erstellt. Dies wird mit Simulationen der Zerstäubung von Atomen mit der SRIM Software ergänzt, aus denen Eigenschaften der zerstäubten Atome, wie ihre Kinematik,

abgeleitet werden können. Darüber hinaus werden Folgerungen für das Rydberguntergrundmodell aufgezeigt.

Indirekte Messungen des Anfangsenergiespektrums der Untergrundelektronen im Volumen des Spektrometers offenbarten Elektronenenergien bis zu einigen Elektronenvolt, die höher als erwartet sind. BBR-induzierte Ionisation von hoch angeregten Atomen genügt deshalb nicht als Produktionsmechanismus, da lediglich Elektronenenergie bis zu 0,2 eV möglich sind. Deshalb werden in dieser Arbeit andere, spezielle Ionisationsmechanismen dieser hoch angeregten Atomen berücksichtigt. Für diesen Zweck wurde Penning Ionisation, Ionisation über elektrische und magnetische Felder sowie Autoionisation untersucht. Es stellte sich heraus, dass im Prinzip kein Ionisationsmechanismus geeignet ist, mit Ausnahme des weniger wahrscheinlichen Vorkommens von planetaren Atomen. Diese zweifach hoch angeregten Atome können langlebig sein, wenn ihre Außenelektronen sich in einem nicht-resonant-wechselwirkenden Ensemble befinden. Über Strahlungsübergänge der Elektronen kann allerdings ein resonanter Zustand erreicht werden, woraufhin das Atom oder Molekül unter Elektronenemission dissoziiert.

Um das Rydberguntergrundmodell weiter zu untersuchen, wurden Messungen mit einer radioaktiven ^{223}Ra Quelle durchgeführt. Dabei wird Rydberg-induzierter Untergrund sowohl von der Quelle selbst als auch von der inneren Oberfläche des Spektrometers untersucht, die gezielt mit kurzlebigen Isotopen der ^{223}Ra Zerfallskette kontaminiert wurde. Jedoch war die Radonemanation von der Radiumquelle viel höher als erwartet, wodurch der Rydberguntergrund nur untersucht werden konnte, nachdem das Ventil zur Quelle geschlossen war. Hierbei wurde der natürliche Zerfall der induzierten Radioaktivität innerhalb des Spektrometers beobachtet, der die Messzeit limitierte, da die langlebigste Tochter eine Halbwertszeit von 36 Minuten aufweist. Nichtsdestotrotz konnte sowohl die Aktivierungssättigung von Oberflächenkontamination durch Volumenradioaktivität des emanierten Radons als auch die Abhängigkeit des induzierten Untergrunds von dem Potential der inneren Elektrode beobachtet werden. Diese Messungen bekunden, dass der induzierte Untergrund gleiches Verhalten wie der vorherrschende KATRIN Untergrund aufweist und demnach eindeutig zeigen, dass Prozesse aufgrund der Zerfälle von ^{210}Pb an der inneren Oberfläche des Hauptspektrometers für den vorherrschenden Untergrund des KATRIN Experiments verantwortlich sind.

Contents

1. Introductions to neutrino physics

Neutrino physics has developed into a large area of research in recent decades. Nowadays physics is filled with different experiments to study the behaviour of neutrinos. Starting in 1930 with the postulation by W. Pauli [1] and the first proof of existence 26 years later by C. Cowan and F. Reines [2, 3], no one could imagine that there are three types of neutrino at this time. But some years later L. Lederman, M. Schwartz, and J. Steinberger discovered the muon-neutrino by decays of pi-mesons in 1962 [4]. After these discoveries more neutrino experiments were set up to study neutrinos from reactors, the atmosphere, or the sun. In the middle of the 20th century they identified a deficit in the solar neutrino flux. Thus, fewer neutrinos were detected than expected, leading to the solar neutrino problem first observed by the Homestake experiment [5, 6]. This observation leads to the prediction of neutrino oscillation which was discovered in the late 1990s by SNO and Super-Kamiokande [7, 8]. To fully understand the mechanism of neutrino oscillation it is necessary to know the mass-scale of neutrinos. One can obtain model-dependent mass limits via cosmology or earlier experiments measured model-independent mass limits via the electron energy of β decays to $m_\nu < 2\ \mathrm{eV}/c^2$ [9]. Measuring a model-independent neutrino mass with high precision is essential for further investigations of our universe.

1.1. The postulation and discovery of neutrinos

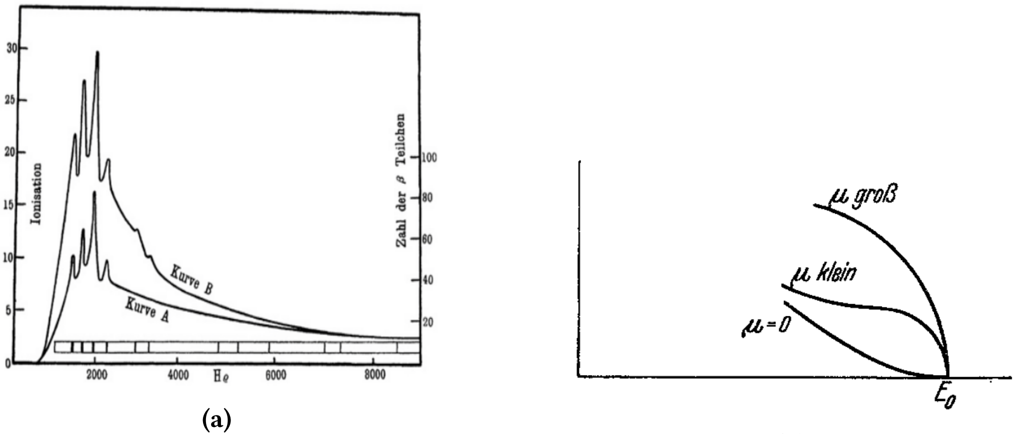

(a)

(b)

Figure 1.1.: (**a**): Continuous β spectrum by Chadwick 1914 [10]. (**b**): Shape of theoretical beta spectrum near the endpoint E_0 depending on the neutrino mass μ [11].

The history of the neutrino [12] starts with the first measurements of β spectra of radium by Chadwick in 1914 [10]. He had expected a monoenergetic spectrum, but observed a continuous one (see fig. 1.1a). In 1922 Lise Meitner [13] measured groups of different velocities from β decaying radioactive elements. She proposed the idea that the β-rays got produced by a secondary process involving γ-rays. The different energies would correspond to different electron shells of the radioactive and their daughter element. That was not wrong, because she measured Auger electrons. Later the continuous spectrum by Chadwick lead Wolfgang Pauli to the contradiction that energy would not be conserved anymore. And so he wrote the famous letter [1] in which he postulated an additional neutral particle - the "neutron". His reasoning was that the energy of the decay products is always constant due to the additional particle, but the individual energies vary. It is described by a three-body decay so the contradiction is solved.

After discovering the neutron as part of the atomic nucleus, E. Fermi set up a theory of β decays [11] in which he gave the additional particle the name "neutrino", whose mass must be less than or equal to that of the electron. The transition probability determines the shape of the spectrum (fig. 1.1b). A comparison of the recorded spectra with his theory revealed that the neutrino mass must be either zero or very small.

F. Reines and C. Cowan proposed an experiment to detect neutrinos in 1953 [14] based on liquid scintillator technique. Near a reactor, the neutrino flux was estimated to be very high, so the prediction was for ten events per minute. Due to cadmium loading in the scintillator solution, they were sensitive to neutron capture and corresponding γ-pulses. The neutrino signal by inverse beta decay Eq. 1.1 is a coincidence of a neutron-induced γ, followed by the positron annihilation radiation [2, 3]

$$\overline{\nu}_{\mathrm{e}} + \mathrm{p} \rightarrow \mathrm{n} + \mathrm{e}^{+} \quad . \tag{1.1}$$

Introduced by a theory of μ meson decay by G. Feinberg [15] the way to another neutrino flavour was levelled. Lokanathan and Steinberger searched in vain for the muon decay into electron and photon. The general assumption was the decay to an electron, a neutrino, and an antineutrino. But if the neutrinos were their mutual antiparticles, they should have annihilated to gammas. However, Feinberg calculated a significantly higher branching ratio for this decay than was measured by Steinberger and Lokanathan [12]. In 1962 L. Lederman, M. Schwartz, and J. Steinberger succeeded in proving the existence of the muon neutrino ν_{μ} [4]. For this discovery they received the Nobel Prize in 1988.

In the late 1980s the ALEPH Collaboration extended the neutrino family. Through measuring the total width Γ_Z of Z boson decays, the physicist were able to estimate the number of neutrinos. The comparison of their data with the model for 2, 3, and 4 neutrinos yielded to a best fit result of $\mathrm{N}_{\nu} = 3.27 \pm 0.30$ [16].

Since the evidence of the existence of τ leptons in 1975 [17], the assumptions have also moved to a third neutrino. Finally the third neutrino was observed by the DONUT collaboration in the year 2000 [18]. The experiment is based at the FermiLab and was designed to observe the tau neutrino ν_{τ} using an 800 GeV proton beam from Fermilab Tevatron as neutrino source. The protons shower off in a tungsten target releasing particles which decay into tau leptons and tau neutrinos. The ν_{τ} itself interacts in a lead emulsion producing again τ's with a specific signature.

1.2. Neutrinos beyond the Standard Model (SM) - ν-oscillation

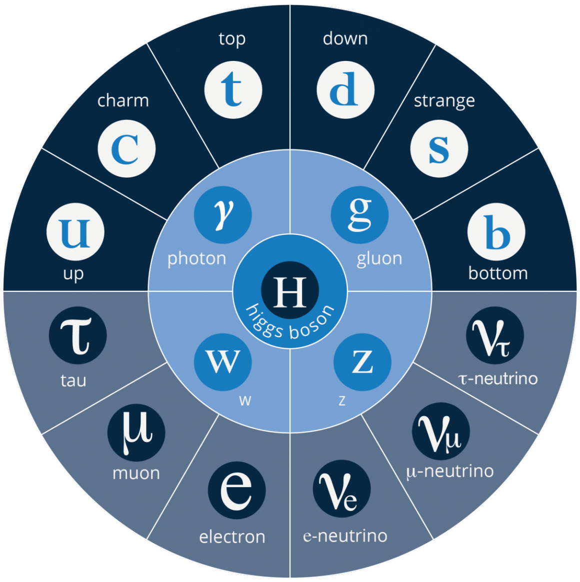

Figure 1.2.: The Standard Model of Particle Physics: upper outer semicircle - quarks; lower outer semicircle - leptons; inner circle - gauge bosons and center - higgs boson [19].

The Standard Model of Paticle Physics (SM) [20] is the very successfull theory of our matter and its interactions. However, in the early days of the theory, there shock when evidence of neutrino oscillation came up. The solar neutrino problem, first observed at the Homestake Experiment [5], measured a lower electron neutrino flux than expected by the pp-chain and the CNO cycle in our sun. Their data matched the results of the Kamiokande-II experiment very well [21] so the solar neutrino deficit was observed but not understood. Only new experiments such as Sudbury Neutrino Observatory (SNO) [22] and Super-Kamiokande [8] were able to take a closer look at this problem. The first evidence of oscillating neutrinos was claimed by the Super-Kamiokande experiment due to a detected deficit of atmospheric muon neutrinos. The data were inconsistent with the predicted atmospheric neutrino flux and not explainable with the current state of knowledge. SNO could separately measure the flux of ν_e in comparison to the overall flux of all flavours. Finally the composite results with the Super-Kamiokande experiment revealed the discovery of neutrino oscillation with 90% confidence level. Proof of neutrino oscillation is a milestone in neutrino physics, as it implies that neutrinos must have mass. For this major effort the directors of these experiments Takaaki Kajita and Arthur B. McDonald were awarded with the Nobel Prize in 2015.

The theory of neutrino oscillation is analogous to the mixture of different quarks invented by Cabibbo [23] with their extension by Kobayashi and Magawa [24]. There are three neutrino flavour eigenstates $\alpha = \mathrm{e}, \mu, \tau$ and three neutrino mass eigenstates $j = 1, 2, 3$ which are not equal. Each flavour eigenstate thus consists of a superposition of the three mass eigenstates to specific portions. The neutrino flavour eigenstate is described by

$$|\nu_\alpha\rangle = \sum_{j=1,2,3} U^*_{\alpha j}\,|\nu_j\rangle = U^*_{\alpha 1}\,|\nu_1\rangle + U^*_{\alpha 2}\,|\nu_2\rangle + U^*_{\alpha 3}\,|\nu_3\rangle \tag{1.2}$$

with the Pontecorvo-Maki-Nakagawa-Sakata matrix (PMNS)

$$\begin{aligned} U &= \begin{pmatrix} U_{\mathrm{e}1} & U_{\mathrm{e}2} & U_{\mathrm{e}3} \\ U_{\mu 1} & U_{\mu 2} & U_{\mu 3} \\ U_{\tau 1} & U_{\tau 2} & U_{\tau 3} \end{pmatrix} \\ &= \begin{pmatrix} 1 & 0 & 0 \\ 0 & c_{23} & s_{23} \\ 0 & -s_{23} & c_{23} \end{pmatrix} \begin{pmatrix} c_{13} & 0 & s_{13}\mathrm{e}^{-i\delta} \\ 0 & 1 & 0 \\ -s_{13}\mathrm{e}^{i\delta} & 0 & c_{13} \end{pmatrix} \begin{pmatrix} c_{12} & s_{12} & 0 \\ -s_{12} & c_{12} & 0 \\ 0 & 0 & 1 \end{pmatrix} \begin{pmatrix} \mathrm{e}^{\frac{i\alpha_1}{2}} & 0 & 0 \\ 0 & \mathrm{e}^{\frac{i\alpha_2}{2}} & 0 \\ 0 & 0 & 1 \end{pmatrix} . \end{aligned} \tag{1.3}$$

Here is $c_{ik} = \cos(\theta_{ik})$, $s_{ik} = \sin(\theta_{ik})$ and $\alpha_{1,2}$ are phase factors which demonstrate the possibility that neutrinos may be Majorana particles - particles that are identical to their antiparticles. The phase factor δ indicates a CP-violation of neutrino oscillation, if its not zero. The parameters of the theory are the mixing angles θ_{ik}, which must be determined in order to quantify the mixture between the states. The physical states - eigenstates of the free Hamiltonian - are the mass eigenstates ν_j. These propagate through space while the flavour state evolves in time [25]. Propagation through matter changes the oscillation properties due to a different effective mass of the neutrino, which is called the MSW effect [26].

Considering an electron neutrino in time, its condition is given by

$$|\nu_\mathrm{e}(t>0)\rangle = U^*_{\mathrm{e}1}\mathrm{e}^{-iE_1 t}\,|\nu_1\rangle + U^*_{\mathrm{e}2}\mathrm{e}^{-iE_2 t}\,|\nu_2\rangle + U^*_{\mathrm{e}3}\mathrm{e}^{-iE_3 t}\,|\nu_3\rangle \neq |\nu_\mathrm{e}(t=0)\rangle\ . \tag{1.4}$$

Now one can estimate the mixing angle by deriving the probability to find a specific flavour state ν_β by the projection of $|\nu_\alpha(t)\rangle$ onto the flavour eigenstate $|\nu_\beta\rangle$. The general expression for P reads

$$P(\nu_{\alpha\to\beta}\left(\frac{L}{E}\right)) = \sum_{k,j} U^*_{\alpha k} U_{\beta k} U_{\alpha j} U^*_{\beta j}\,\mathrm{e}^{-i\frac{\Delta m^2_{jk} L}{2E}}\ , \tag{1.5}$$

with L the distance between detector and source, E the energy of the neutrino, and $\Delta m^2_{jk} = m_i^2 - m_k^2$ the mass splitting. Several experiments extract these parameters from their data such as Super-Kamiokande for θ_{23} [8], DoubleChooz and Daya Bay for θ_{13} [27, 28], and KamLand for θ_{12} [29] to values of

$$\sin^2(\theta_{12}) = 3.20^{+0.20}_{-0.16}\cdot 10^{-1} \tag{1.6}$$

$$\sin^2(\theta_{23}) = 5.47^{+0.20}_{-0.30}\cdot 10^{-1} \tag{1.7}$$

$$\sin^2(\theta_{13}) = 2.160^{+0.0083}_{-0.069}\cdot 10^{-2} \tag{1.8}$$

$$\Delta m^2_{12} = 7.55^{+0.20}_{-0.16}\cdot 10^{-5}\,\mathrm{eV}^2 \tag{1.9}$$

$$|\Delta m^2_{31}| = 2.50^{+0.03}_{-0.03}\cdot 10^{-3}\,\mathrm{eV}^2 \tag{1.10}$$

$$\delta/\pi = 1.21^{+0.21}_{-0.15} \tag{1.11}$$

by Salas [30, 31].

1.3. Motivation and implementation of neutrino mass determination

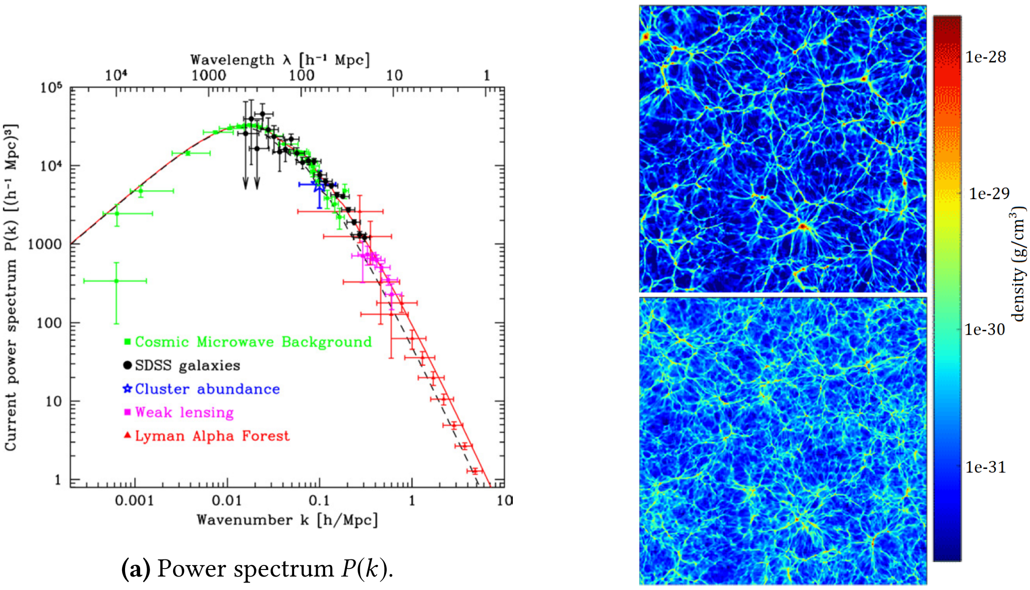

(a) Power spectrum $P(k)$.

(b) Density map.

Figure 1.3.: (**a**): Cosmological constraints in the current matter power spectrum $P(k)$. The *solid* curve represents the theoretical prediction for a scale-invariant model with a neutrino mass sum $M_\nu = 0$. The *dashed* curve illustrates the effect on the power spectrum for a non-zero neutrino mass of about 1 eV corresponding to 7% of the dark matter density [32, 33]. (**b**): Density distributions of large scale structures in the universe for massive (bottom) and massless (top) neutrinos. On the bottom the neutrino mass sum is $M_\nu = 1.9$ eV, showing that the density has less contrast [34].

Cosmological data provides the main motivation for studying the neutrino mass due to the observations of the structures of the universe, such as the CMB, gravitational lensing or the Ly-α-forest. 336 relic neutrinos per cm^3, remnants of the Big Bang, fill the entire universe. Although neutrinos are very light, they have a noticeable effect on the total density of dark matter. If their mass were 0.05 eV, they would make up about one percent of the total mass of the universe. The relic neutrinos decoupled from the thermal equilibrium in the very early universe about 1 second after the Big Bang at a temperature of $\propto 10^9$ K. This process is called "freeze-out" and takes place when the Hubble parameter is greater than the annihilation rate [35].

The power spectrum of matter fig. 1.3a demonstrates the density contrast of the universe as a function of the scale. It demonstrates the effects of the neutrino mass on the size of structures. For a neutrino mass of 1 eV, small structures are suppressed by a factor of 2 - *dashed* line. One can estimate an upper limit on the neutrino mass within the measurement uncertainty. From simulation of large scale structure, more precisely of density of matter on large scales, one can distinguish the influence of a massive neutrino (see fig. 1.3b). Small

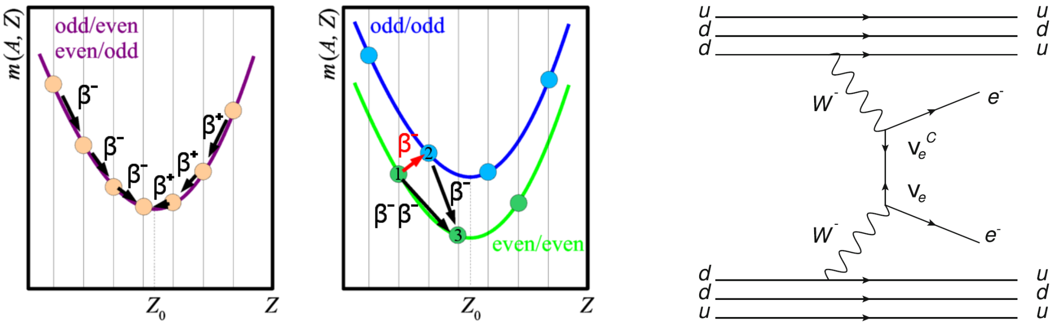

(a)

(b)

Figure 1.4.: (a) Mass spectrum of possible single beta decays. On the right side the energetically forbidden case for an element to decay by single beta decay [36].
(b) Feynman graph of neutrinoless double beta decay (0νββ) [25].

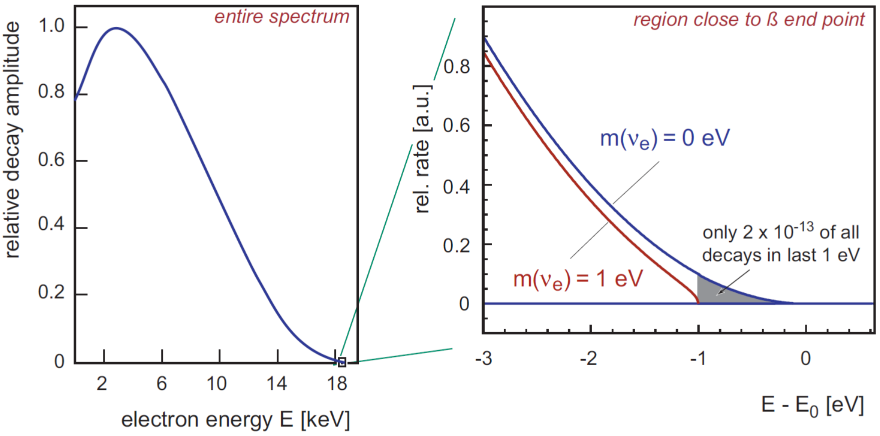

Figure 1.5.: The β spectrum of tritium: the entire spectrum (left) and the end point region with the neutrino mass influence of $m_\nu = 1$ eV (right) [37].

structures get thinned, resulting in less contrast in the shape due to collisions with massive neutrinos. Knowing the absolute neutrino mass therefore leads to better understanding of our universe and is essential for research.

There are several ways to measure the neutrino mass, but only two that are associated with beta decay. On the one hand, there is the theory of neutrinoless double beta decay (fig. 1.4b). And on the other hand by measuring the kinematics of electrons from single beta decays (fig. 1.5).

Neutrinoless double beta decay (0νββ) is a hypothetical decay channel of double beta decaying elements such as ^{76}Ge and ^{136}Xe (fig. 1.4b). In general, double beta takes place when the atomic nuclei has an even/even configuration. One β decay converts a neutron into a proton so the nucleus gets from even/even to odd/odd. Sometimes the energy of the daughter nucleus is higher so single beta decay is energetically forbidden and double beta decay occurs as a second order process (fig. 1.4a). The process only can take place under the assumption that neutrinos are Majorana particles - the neutrino is its own antiparticle. Therefore the neutrinos from the two decays can absorb each other. By measuring the lifetime $T_{1/2}$ of the elements, one can calculate the decay amplitude Γ which directly depends on the neutrino mass. Present experiments are GERDA [38], EXO [39], and MAJORANA [40] without evidence of existence of $0\nu\beta\beta$ to date.

In a single β^- decay of nuclei, a neutron converts into a proton, an electron, and an electron anti neutrino:

$$X(A, Z) \longrightarrow X(A, Z-1) + \mathrm{p} + \mathrm{e}^- + \overline{\nu}_\mathrm{e} \quad . \tag{1.12}$$

The kinematics of the electron contains information about the neutrino mass, as the decay represents a 3-body problem and energy has to be conserved. The neutrino mass affects the entire spectrum, but the effect is most noticeable near the endpoint energy E_0 (see fig. 1.5). One can see the small variation in the spectrum that corresponds to the prediction by Fermi (fig. 1.1b), for a small mass. Past measurements with experiments in Mainz and Troitsk set an upper limit of the neutrino mass of $m_\nu < 2\,\mathrm{eV}/c^2$ [9].

Following these measurements, the KATRIN experiment was designed and built [41]. Officially launched on 11th June 2018, it will reach an unmatched sensitivity of $\propto 240\,\mathrm{meV}$ after 5 years of data collection.

2. The KATRIN experiment

2.1. Arrangement of the KATRIN experiment

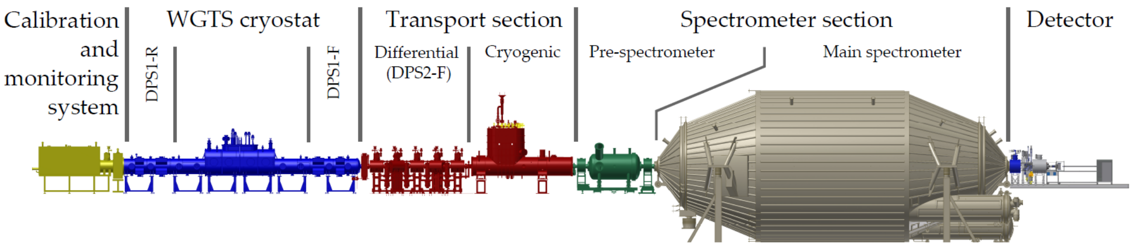

Figure 2.1.: Setup of the KATRIN experiment. From left to right: Yellow - Rear section, Blue - Windowless Gaseous Tritium Source (WGTS), Red - Transport section consisting of Differential Pumping Section (DPS) and Cryogenic Pumping Section (CPS), Green - Pre-spectrometer, Grey - Main spectrometer (excluding air coils) and Detector [42].

The Karlsruhe Tritium Neutrino (KATRIN) experiment aims to determine the absolute mass scale of the electron anti neutrino in a model-independent way by measuring the beta spectrum of molecular tritium with high precision. To achieve the sensitivity of $\propto 240\,\text{meV}$, an high resolution energy device is needed. This device is the main spectrometer, which acts as a MAC-E filter (Magnetic Adiabatic Collimation combined with Electrostatic filter). Gaseous tritium is introduced into the WGTS and kept at a constant level by supply and removal. Inside the WGTS, the tritium decays, whereupon the electrons are guided magnetically to the main spectrometer. DPS and CPS filter resulting ions and lower the tritium flow by more than 14 orders of magnitude. Neither ions nor tritium should be able to get into the main spectrometer, only electrons, otherwise an increased background is created. The pre-spectrometer is used for the first separation of high-energy electrons with energies above 18 keV. As a result, the electron density in the main spectrometer does not become so high that residual gas ionisation would become more likely. In the main spectrometer, the electrons are further separated by the retardation potential. By controlling the high voltage of the retarding potential, the electrons are recorded in an integrated beta spectrum. In the following chapters, the individual components of the experiment as well as the measuring principle are explained in more detail.

2.1.1. The source and transport section (STS)

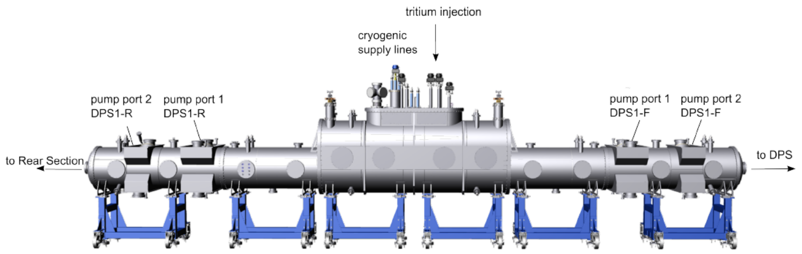

Figure 2.2.: WGTS: Windowsless gaseous tritium source of the KATRIN experiment [43].

The windowsless gaseous tritium source (WGTS) fig. 2.2 forms the central starting point of neutrino mass measurement. Here, the molecular tritium is continously supplied by injection of gas, and then removed via four turbo molecular pumps at both ends, so that the concentration of the radioactive substance always remains constant. This constituent must be operated very accurately, so the column density of tritium molecules ($5 \cdot 10^{17}\,\text{cm}^{-2}$) is stable on a 0.1 % level. For this purpose, injection pressure and temperature must also be stable within very small variations of the same order. The 10 m long beam tube is operated at a temperature of 30 K, which is achieved by a neon cooling system. The injection pressure is about $3.35 \cdot 10^{-3}$ mbar and during the diffusion to the ends of the WGTS, an activity of 10^{11} Bq is reached, sufficient for study of the tritium endpoint E_0 (see fig. 1.5). In addition to pressure and temperature, the amount of tritium and its activity and purity are monitored by the Forward Beam Monitor (FBM) [44]. The FBM is the only device that measurements within the β-electron flux tube can be performed. The detector board consits of two PIN diodes of different size which can determine the relative β-electron flux with a precision of 0.1% in less than 60 s or a differential spectrum with an energy resolution of 2 keV. The gas composition is monitored by a laser Raman system, while the activity is checked by β-induced X-ray spectrometry (BIXS) in the rear section [45]. The electrons generated at the source are magnetically guided to the spectrometers. On their

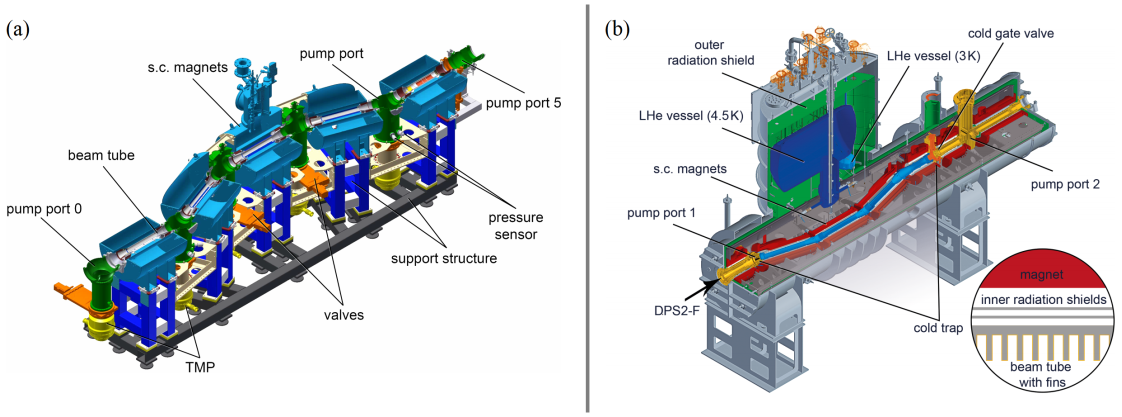

Figure 2.3.: (**a**): Differential Pumping Section (DPS). (**b**): Cryogenic Pumping Section (CPS)[46].

way through the transport section, they pass through two chicanes, where the tritium flow is drastically reduced, as no tritium should enter the spectrometer section. This task is performed by the Differential and Cryogenic Pumping Sections (see fig. 2.3), which reduce the tritium flow by 14 orders of magnitude.

Within the DPS, the β-electrons are guided though a strong magnetic field of 5.6 T, overcoming four bends of 20° each. Turbo molecular pumps installed on these bends reduce tritium flow with an increased effective pumping rate by 7 orders of magnitude. Other molecules are efficiently removed from the beam tube as well, which would flow on a straight path to the spectrometers. The Cryogenic Pumping Section additionally includes a liquid-helium cooled 3 K cold inner surface, which is covered by an adsorbed argon frost layer. This argon frost cryosorbs any molecules that contain tritium and reduces the tritium flow by another 7 orders of magnitude [25, 47].

2.1.2. The spectrometer and detector section (SDS)

Both the pre-spectrometer and the main spectrometer are operated as MAC-E filters [49](see fig. 2.4). A MAC-E (Magnetic Adiabatic Collimation with Electrostatic) filter acts as a high pass filter for electrons. Strong magnetic fields, provided by superconducting solenoids, adiabatically guide electrons, which are emitted isotropically at the source, through the spectrometer onto the detector. While travelling through the magnetic and electric fields of the spectrometer, electrons experience the Lorentz force due to the magnetic field and move on cyclotron trajectories. The electric field acts the filter component because the electrons must overcome a potential barrier. The electrons are generated isotropically in the source, so that their momentum vector is at a polar angle θ to the magnetic field lines. This leads to the splitting of parallel and transverse component of momentum or energy, respectively. The filtering electric field only affects the longitudinal component. To achieve a good energy resolution it is necessary to transform the transverse component $E_\perp$ into the longitudinal one $E_{||}$. This is achieved by the MAC-E filter principle,

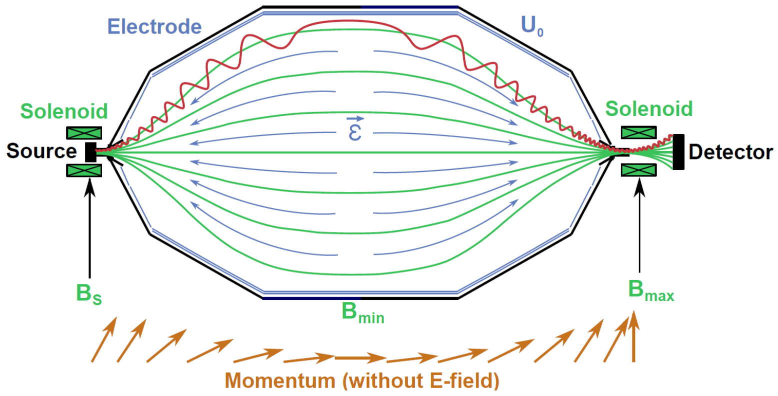

Figure 2.4.: The MAC-E filter principle. On each side of the spectrometer is a superconducting magnet that generates the magnetic guiding field (green) of the electrons. The red curvature shows a cyclotron trajectory of an electron, exaggerated in size. The blue arrows demonstrate the electric field $\vec{\varepsilon}$ produced by the electrode with potential U_0 [48].

the magnetic field drops several orders of magnitude from the source to the analysing plane, which is located at the center of the spectrometer, where the magnetic field is minimal (see fig. 2.4 B_{min}). Due to the slow change of the magnetic field the momentum transforms adiabatically, so the magnetic moment $\mu = \frac{E_{\perp}}{B}$ remains constant. Since a small transversal part is always present, the energy resolution

$$\Delta E = E^{A}_{\perp,\text{max}} = \frac{B_{\text{min}}}{B_{\text{max}}} \cdot E_{\text{kin}} \tag{2.1}$$

depends on the maximum transversal energy an electron can still have in the analysing plane. For the reference values of $E_{\text{kin}} = 18.6\,\text{keV}$, $B_{\text{min}} = 3 \cdot 10^{-4}\,\text{T}$ and $B_{\text{max}} = 6\,\text{T}$ one obtains $\Delta E = 0.93\,\text{eV}$.

The main spectrometers dimensions are established by the conservation of the magnetic flux $\Phi \approx A \cdot B$. Since the magnetic field drops by several orders of magnitude to the analysing plane, the area of the flux tube must increase to the same extent. Accordingly, the main spectrometer was built with a length of 23.8 m and a diameter of 9.8 m.

The entire spectrometer is set to high voltage, which is changed in steps of $\Delta U \sim 0.5 - 1\,\text{V}$ to record the spectrum. Additionally it is equipped with an inner electrode system that has a higher voltage than the vessel, so secondary electrons from the wall are shielded and can not produce background. To prevent residual gas scattering of the β-electrons both spectrometers are operated at Ultra High Vacuum (UHV) conditions of about 10^{-11} mbar guaranteed by several getter and turbo molecular pumps (TMP). So that the magnetic field inside is not influenced by the earth's magnetic field from the outside, large coils surround the spectrometer, which also allow a fine tuning of the magnetic field at the analysing plane.

After passing the spectrometer and the pinch magnet (6 T), the electrons arrive, guided by the detector magnet (3.6 T), at the detector. The Focal Plane Detector (FPD) counts the electrons by a silicon PIN-diode array with high effiency and nearly free of background. It is divided into 148 pixels arranged in 12 concentric rings, which are azimuthally subdivided into 12 pixels plus 4 center pixels. The electrons will pass the analysing plane at different radii, so they experience slightly different potentials due to inhomogeneities. By this arrangement, a spatial resolution can be obtained and irregularities of the retarding potential can be detected.[25, 41, 48, 50]

2.1.3. Measuring principle of neutrino mass determination

The KATRIN experiment aims to determine the effective electron anti neutrino mass $m_{\overline{\nu}_e}$ by precisely measuring the β-spectrum of tritium near the endpoint E_0 (see fig. 1.5). This chapter gives the design parameters, which has to be fullfilled to achieve the sensitivity of $m_{\overline{\nu}_e} \leq 240\,\text{meV}$ (90% C.L.).

A source with high luminosity is essential, as it is directly linked to the signal strength at the end point. For this purpose an optimal column density of tritium of $\rho d = 5 \cdot 10^{17}$ molecules per cm^2 has been chosen, which provides enough activity by manageable scattering probability. The source magnetic field $B_S = 3.6\,\text{T}$ and the maximum magnetic field at the pinch magnet $B_{\text{max}} = 6\,\text{T}$ limits the the maximally allowed polar angle to

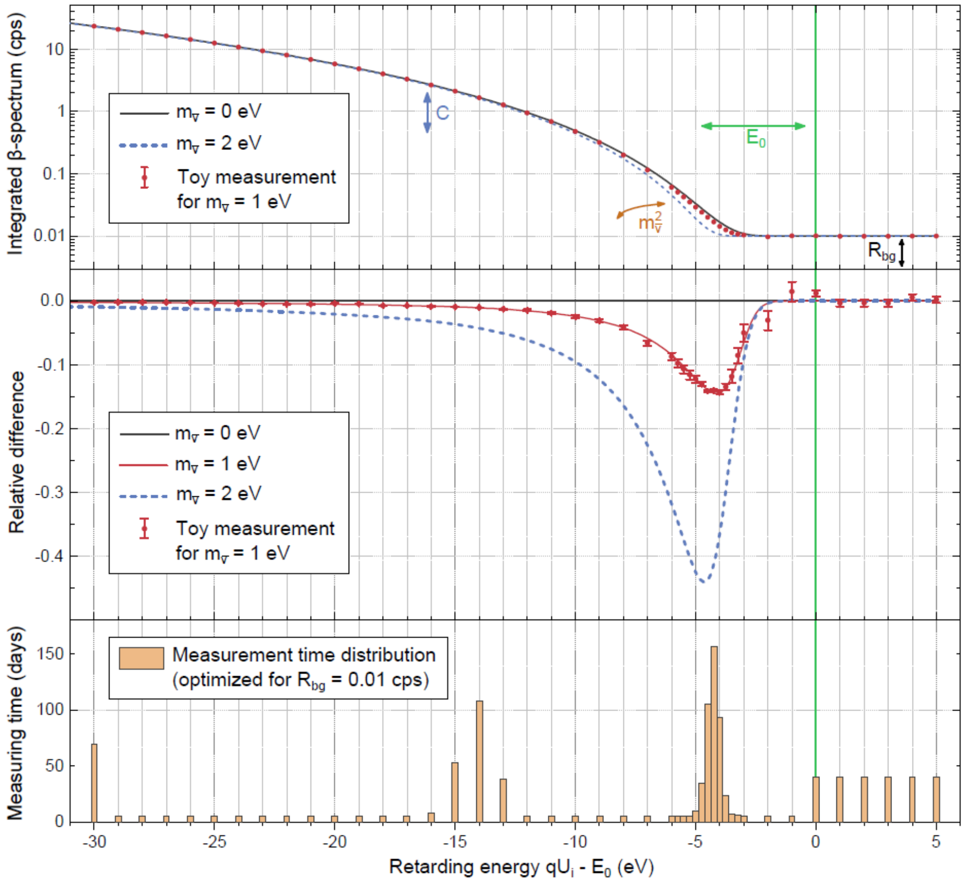

Figure 2.5.: Integral tritium β-spectra (top) with their relative count rate differences (middle), and the measurement-time distribution (bottom). Demonstration of the spectrum with different neutrino masses of 0 and 2 eV and a toy measurement with 1 eV and the design background rate $R_{bg} = 0.01$ cps. The measuring-time distribution gives the measuring time per voltage setting around the endpoint [48].

$\theta_{\max} = 51°$. Therefore only the fraction $T = 1 - \cos(\theta_{\max})$ of electrons can be analysed [25].

In contrast to the Mainz (Troitsk) experiment [9] the KATRIN setup reached significantly better performance. The effective source area has increased by a factor of 40 (20) to $A_S^{\text{eff}} = A_S \cdot B_S/B_{\max} = 31.8\,\text{cm}^2$. A_S and B_S define the sensitive magnetic flux tube to $\Phi = 191\,\text{Tcm}^2$, which is not allowed to collide with beam tube elements. In comparison to the Mainz (Troitsk) experiment the improvement is an energy resolution factor of 5 (4) to the value of $\Delta E = 0.93$ eV, which requires a minimum magnetic field in the analysing plane of $B_{\min} = 3 \cdot 10^{-4}$ T. As mentioned before this design requirement increased the spectrometer significantly to a diameter of 9.8 m, where the analysing plane has the size of 63.6 m^2.

Figure 2.5 shows spectra of simulated KATRIN data. At the top one can see the expected count rates of the integrated β-spectrum in cps as a function of the retarding energy $qU_i - E_0$. The black line symbolises the spectrum with a vanishing neutrino mass, while the dotted blue curve shows the spectrum with a neutrino mass of $m_\nu = 2$ eV. This results in a slight difference near of the endpoint E_0. The red dots demonstrate a toy measurement with a neutrino mass of 1 eV with a net KATRIN run time of 3 years, calculated by a Monte-Carlo simulation. At the bottom the optimised measurement time distribution shown, corresponding to the best possible exclusion of a vanishing neutrino mass. The middle part clarifies the most sensitive region on the neutrino mass by directly comparing the theoretical spectra for 0, 1, and 2 eV neutrino masses with the measurement. The statistical fluctuations depend on the time spent at a specific retarding potential U_i, in addition to the decay β-electron rate.[48]

The overall background rate was designed to be $R_{\mathrm{bg}} < 0.01$ cps (counts per second), to gather large signal-to-background ratios. This is the most challenging design goal for the spectrometer and would correspond to an effective background reduction factor of ≈ 50 (≈ 400) in comparison to the Mainz (Troitsk) experiment.[9, 41]

2.2. KATRIN backgrounds

The background sources or more precisely their origin mechanism at the KATRIN experiment are constantly evolving. According to the analyses of the Mainz and Troitsk experiments, whose spectrometer dimensions differed by a factor of 4, no increased background was detected due to the size. This assumption led to the design background of 0.01 cps which is of the same order of magnitude as the previous experiments. Before the KATRIN main spectrometer was built, some sources were already known or predicted to be very probable.

Based on the data from Mainz and Troitsk, they expected secondary electrons originate inside the spectrometer by ionisation. If these low energy electrons are emitted between the analysing plane and the detector, they get accelerated onto the detector with energies in the region of interest. In addition, if their polar angle is too high, electrons have the probability of being magnetically trapped in the spectrometer. Due to their long stay,

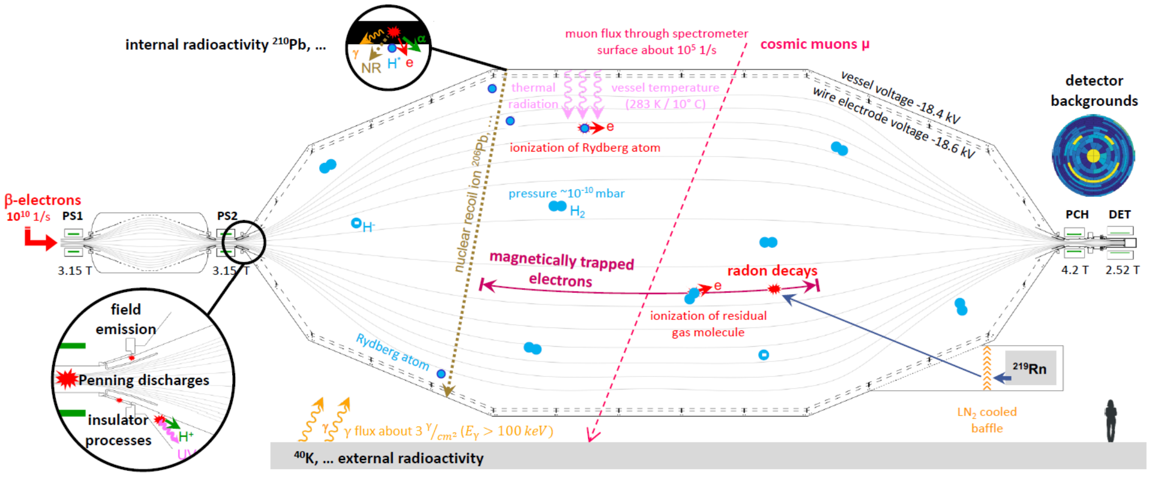

Figure 2.6.: Background sources of the spectrometers [51].

they can ionise residual gas, which in turn supplies secondary electrons. One generating process is the interaction of cosmic muons with the spectrometer hull or electrodes. In Troitsk, the signature of H^--ions was detected, which are magnetically guided in the same way as electrons. These have been efficiently removed in Mainz via NEG-getter pumps. A penning trap between the pre and main spectrometer was also considered, as well as environmental radioactivity, which can cause high energy gammas or δ-electrons from the wall and electrodes.[41]

These background sources will now be explained in detail with their associated measurements. This is followed by description of the most recent extension of the background model, the interaction of Rydberg atoms (sec. 2.3).

2.2.1. Cosmic muons

A major component of the background is expected due to the interaction of cosmic muons with the main spectrometer vessel and the inner electrode. This releases secondary electrons through scattering processes into the spectrometer. The stainless steel surface of the main spectrometer is about 650 m^2, which is exposed to the cosmic radiation at sea level. By upscaling the measured rate from the Mainz experiment one expects a rate of secondary electrons up to $10^5\ \mathrm{s}^{-1}$, originating from the main spectrometer wall [52]. To measure the background from cosmic rays, nine muon detector panels were installed at the main spectrometer with an overall sensitive area of 16.7 m^2 [53]. These modules comprise of an organic plastic scintillator and eight photomultipliers each. Thus, charged particles passing through the scintillator are detected by photon emission collected by the PMTs.[54]

Johanna Linek made correlation measurements to relate the cosmic muon flux to the background electron rate at the Focal Plane Detector (FPD). The correlation at the high

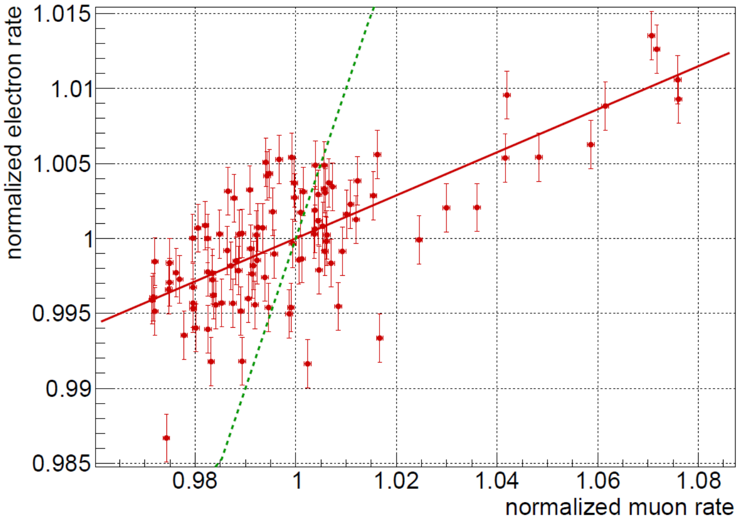

Figure 2.7.: Correlation between muon rate and electron rate at the FPD in the Region of Interest ROI (19.7 – 24.7 keV). The green dashed line corresponds to 100% muon induced events [54].

energy regime (above 130 keV) was 0.711 ± 0.002 and the fraction of muon induced events in this regime was calculated to be 88 ± 5%, wherein these events are induced in the detector wafer itself. However, it has been found that the correlation in the ROI is nearly equal with $r = 0.72 \pm 0.06$, but only a fraction of 14.4 ± 0.7% can be assigned to muons (see fig. 2.7).[54]

Indeed, this fraction of correlation was only accessible for specific magnetic field settings, where electrons from the vessel wall are guided to the detector. At the nominal magnetic field setting no correlation can be seen and therefore muons do not contribute to the KATRIN main spectrometer background. Due to this result, further processes must be considered. Radioactivity is, in addition to muons, a source of secondary electrons, described in subsection 2.2.4. From secondary electrons of muons there is the probability that they are magnetically trapped, these can also ionise residual gas and cause background electrons. The properties of these electrons will be explained in the following section.

2.2.2. Trapped electrons

As mentioned before, electrons inside the spectrometer can be magnetically trapped. These secondary electrons are produced by cosmic rays or radioactive elements inside the spectrometer. Due to their long stay they can ionise residual gas and produce more background electrons. This trapping was first observed in the pre-spectrometer [50].

Figure 2.8 shows a trajectory of an electron trapped in a magnetic field. The magnetic field is only slightly changing so the motion of charged particles is adiabatic, therefore the magnetic moment μ is conserved. As the magnetic field changed, the transverse momentum is converted to longitudinal and vice versa. During this conversion, the polar angle $\theta(\vec{r})$ also changes according to the function:

$$\theta(\vec{r}) = \arcsin\left(\sqrt{\frac{|\vec{B}(\vec{r})|}{|\vec{B}(\vec{r}_0)|}} \cdot \sin(\theta_0)\right) , \tag{2.2}$$

starting at position $\vec{r}_0$ in a magnetic field $\vec{B}(\vec{r}_0)$ with θ_0.

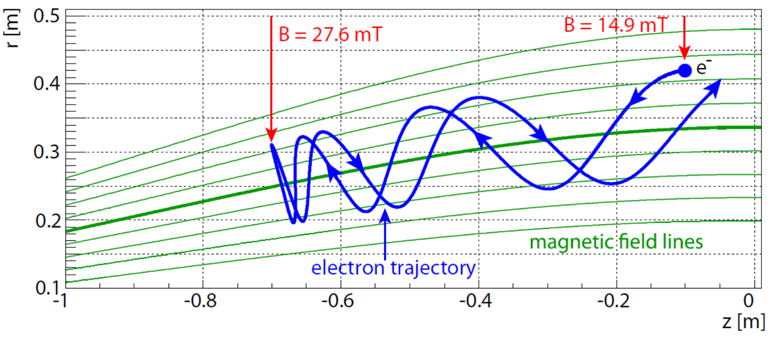

Figure 2.8.: Electron trajectory affected by the magnetic mirror effect in the magnetic field of the pre-spectrometer, starting conditions: $z = 0.1\,\mathrm{m}$, $r = 0.42\,\mathrm{m}$, $\theta = 130°$, and $E_0 = 200\,\mathrm{keV}$ [50].

For example, an electron moves to regions of higher magnetic field, wherein the polar angle θ increases. The polar angle can reach 90° if the magnetic field is sufficiently large (eq. 2.2), with the total energy in the transverse component. Subsequently, the transversal motion tilts and the electron is reflected, which is called the magnetic mirror effect. Taking a closer look, this movement is explained by the Lorentz force. The magnetic field has a radial component which acts in the transverse movement. The Lorentz force points to the area of lower magnetic field, so that the transverse component is weakened [50]. The storage probability is energy dependent. The minimum energy threshold is determined by the resolution of the spectrometer, which is about 0.93 eV. While the maximum energy is about 100 keV, since here the cyclotron radius is greater than the spectrometer radius, causing the electron to hit the wall. Most likely, electrons with energies between 10 eV and 1000 eV are stored.[55]

2.2.3. Penning traps and Penning discharge

It is possible to store electrons in a Penning trap by a specific configuration of electric and magnetic fields. Figure 2.9 shows the configuration of two Penning traps. Assuming an electron with zero kinetic energy in the center of the cathodes from the left picture, it can not move along the z-direction because of the negative potentials at the cathodes. The movement in x/y-directions is also suppressed because the magnetic field would cause a Lorentz force and deflects the electron back to its starting position [50]. The right part of this figure is an example of a Penning-Malmberg trap. There, the magnetic field lines point from the vacuum with negative potential through a more positive potential to the vacuum on negative potential. This configuration forms a Penning trap between the two cathodes as well due to the positive well in the middle and symbolises the Penning trap between the pre- and main spectrometer at KATRIN.

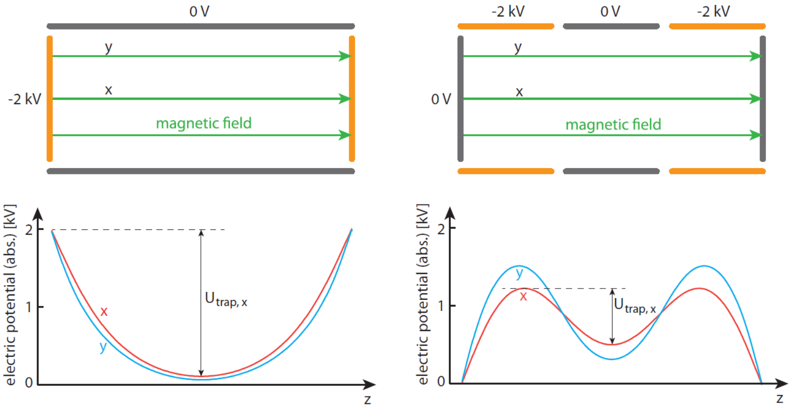

Figure 2.9.: Schemes of Penning traps: cathode to cathode Penning trap (left), vacuum to vacuum (right). The upper part shows the geometry with the direction of the magnetic field lines (green), the cathodes (orange), and the anodes (grey) with electrode potentials. The lower part demonstrates the electric potential along the magnetic field lines x and y. The corresponding depths of the Penning trap $U_{\text{trap},x}$ along x are also shown [56].

A Penning discharge can ignite when the storage probability of electrons is high. First a primary electron is produced by cosmic rays or natural radioactivity, which gets trapped. The trap must be sufficiently large, at least of the order of the ionisation threshold of the residual gas molecules ($\propto$ 10 eV), so that they can be ionised, whereby more electrons are formed and captured. The ionisation of residual gas causes the formation of positive ions, which get accelerated to the cathode, releasing more electrons that can be trapped with a certain probability. If the electrons are stored for significantly long times each secondary electron can further ionise residual gas, increasing the number of stored electrons significantly. Although the pressure is very low, an electron with an energy of 500 eV has a mean free path on the order of 1000 km and undergoes about 3 collisions with residual gas every second [56]. Therefore this process gathers a large number of electrons inside the trap and a self-incurred discharge can occur, releasing these electrons with high energy.[50, 56]

2.2.4. Natural radioactivity

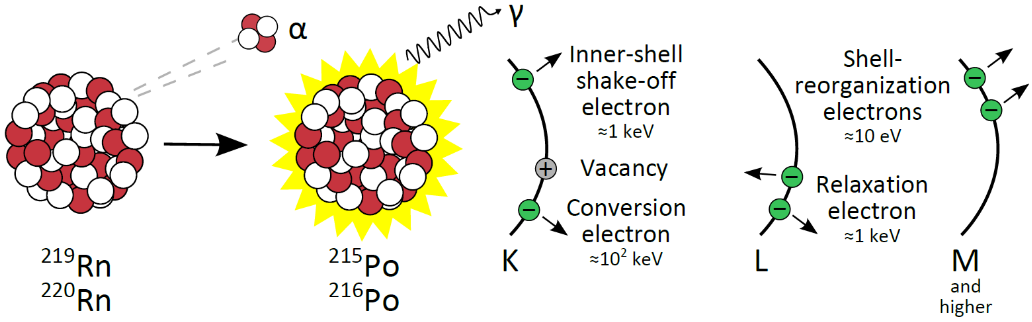

Figure 2.10.: Illustration of radon α decays followed by electron emission of different mechanisms caused by excitation of the daughter nucleus polonium [48].

Natural radioactivity is always a challenging background source in low-rate experiments such as GERDA [38] and BOREXINO [57–59]. With reference to Figure 2.6, there are two ways in which radioactivity can affect measurements. On the one hand, there is external radioactivity by γ-emitting radioactive elements such as ^{40}K, providing γs with energies above 100 keV. On the other hand, there can be intrinsic radioactivity mainly due to decays of radon isotopes ^{219}Rn, ^{220}Rn and ^{222}Rn.

The γ-flux from natural radioactivity inside the spectrometer building was measured to be on the order of $1\,\gamma\,\mathrm{cm}^{-2}\,\mathrm{s}^{-1}$ for energies above 100 keV. To further investigate the possibility of influence, a ^{60}Co source with an activity of 53 MBq was placed next to the spectrometer vessel, where no increased background rate was observed. Therefore, natural radioactivity from outside the spectrometer does not impinge the experiment.[60]

Radon-induced background caused by intrinsic radioactivity is a major background component in the KATRIN experiment [55, 61, 62]. The naturally occurring radon isotopes ^{219}Rn, ^{220}Rn, and ^{222}Rn, emerging from the primordial decay chains of ^{235}U, ^{232}Th, and ^{238}U, belong to the largest contributors of the worldwide background radiation dose [48].

Figure 2.10 shows the different mechanisms of how electrons are emitted by radioactive decays of radon, including their energies. Thereby the radon atom (mainly ^{219}Rn) decays via an α decay into an excited state of polonium (Po), which leads to secondary electron emission. These electrons can originate from inner-shell shake-offs (E $\approx$ 1 keV), conversion (E $\approx$ 100 keV), relaxation (E $\approx$ 1 keV), or shell-reorganisation (E $\approx$ 10 eV). In the case of ^{219}Rn, up to 20 electrons can result from one decay [48]. These electrons either get trapped and cause more secondary electrons or find their way to the detector as background events. The radon emanation in the KATRIN main spectrometer is well known, firstly it can leak from the main spectrometer stainless steel surface, the inner electrodes, or other equipment inside the system. Secondly it can arises from the non-evaporable getter (NEG) material which has to maintain the ultra high vacuum condition of $p \leq 10^{-11}$ mbar in the spectrometer [63]. In order to reduce this source of background electrons, three liquid nitrogen cooled baffles were installed between the NEG pumps and the sensitive flux volume. Radon atoms emanating from the NEG strips propagate with thermal velocity towards the main spectrometer, but stick to the much cooler copper baffle. They adhere longer than their decay time, so ^{219}Rn from the NEG pumps no longer dominates the background. The LN$_2$-cooled baffle reaches a suppression efficiency of $(95.1 \pm 0.3)\%$, allowing the background rate of remaining radon form the NEG pumps to be estimated to $R_{\text{tot}} = (36^{+18}_{-15})$ mcps, which significantly exceeds the KATRIN design level of < 10 mcps.[48]

The amount of ^{220}Rn, in contrast to ^{219}Rn, was measured to be two orders of magnitude smaller so this element can be neglected [50]. The neutral noble gas atoms are not affected by the electric or magnetic field inside the spectrometer, therefore they can easily reach the active flux tube, where produced electrons result in background events. The background rate from radon strongly depends on the lifetime of the isotope as well as the averaged

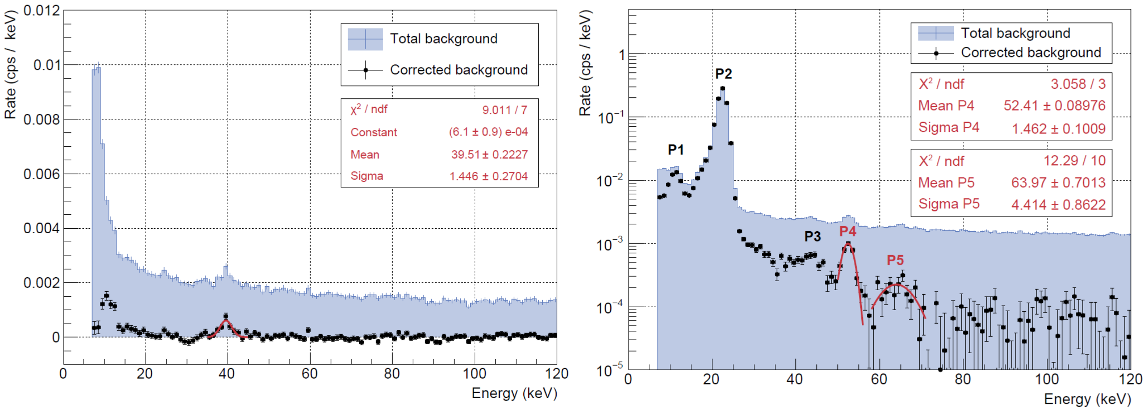

(a)

(b)

Figure 2.11.: (**a**): Background electron energy spectrum at zero vessel potential. Total background rate from 7 – 120 keV (blue) and after corrections for the intrinsic detector background (black dots). Peak-like structure can be seen at 40 keV with Gaussian-fit from 35 – 45 keV [48]. (**b**): Background electron energy spectrum at high vessel potential $U_0 = -18.6$ kV with lower post-acceleration of $U_{PAE} = +4$ kV and combination of different inner-electrode potentials of −5 V and −100 V. Total background rate from 7 – 120 keV (blue) and after corrections for the intrinsic detector background (black dots) [48].

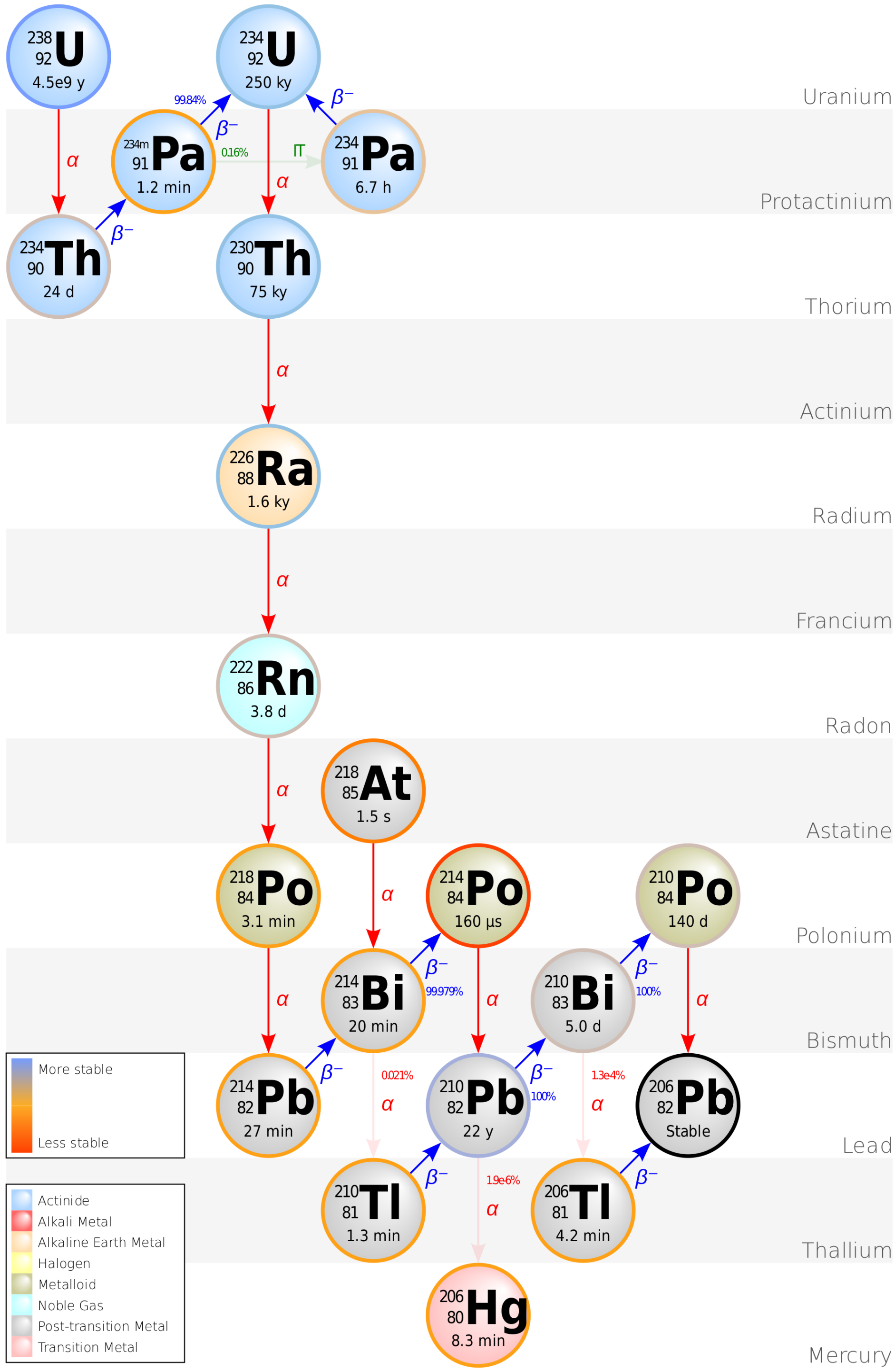

Figure 2.12.: The 4n+2 chain of ^{238}U. Commonly called radium series, beginning with uranium-238 and terminating with lead-206. The coloured frames around the isotopes refer to their stability from dark blue to red, black indicates stable [64].

pump-out time by the TMPs. The short-living isotopes ^{219}Rn ($t_{1/2} = 3.96\,\mathrm{s}$) and ^{220}Rn ($t_{1/2} = 55.6\,\mathrm{s}$) will cause background events due to their short lifetime on the order of seconds. The mean pump-out time at the main spectrometer is $t_{\mathrm{MS}} \approx 360\,\mathrm{s}$, thus the longer-living ^{222}Rn ($t_{1/2} = 3.82\,\mathrm{d}$) is efficiently pumped out. Therefore, ^{222}Rn is initially not treated as a background source.[48]

During the KATRIN commissioning phase SDS-IIa, several background measurements were performed, investigating a larger energy range compared to the SDS-I phase. While only the ROI was considered in SDS-I, energies in the range from 0.2 keV to 260 keV were examined in SDS-IIa. These measurements, taken with the main spectrometer at zero potential as well as standard HV setting, revealed a novel background source from the spectrometer vessel wall.[48]

Figure 2.11a shows the background electron energy spectrum SDS-IIa at zero potential. A peak-like structure occurred around 40 keV with a Gaussian-fit line position of (39.5 ± 0.2) keV and a peak width of (3.4 ± 0.6) keV. This structure could belong on the one hand to γ-photons of about 40 keV and on the other hand to mono-energetic electrons with an energy of 30 keV. The post acceleration voltage $U_{PAE} = 10\,\mathrm{kV}$ means electrons from the spectrometer volume get boosted onto the detector with additional energy of 10 keV. To determine one cause or another, the measurement was compared to a measurement with the post-acceleration voltage of zero. Here, an increased rate was measured at 30 keV, confirming the acceptance of electrons. Additional measurements on high spectrometer potential showed clearly the presence of a second peak-like structure with a higher energy, fig. 2.11b. Peak P1 corresponds H^- ions at $\approx 11\,\mathrm{keV}$ due to energy loss in the detector dead layer and P2 to low energy electron background events with a small surplus energy of a few eV. P3 corresponds to the double incident events of P2. The Peaks P4 and P5 correspond to the L- and M-shell conversion electrons from ^{210}Pb fit with Gaussians to values of 52.41 ± 0.09 keV (L-shell) and 63.97 ± 0.70 keV (M-shell).[48]

The best candidate to explain the observed peaks in the main spectrometer background is the radioactive isotope ^{210}Pb. Starting from ^{238}U, ^{210}Pb is formed over several alpha and β^- decays while ^{222}Rn was also formed (see fig. 2.12).

$^{210}_{82}$Pb decays via β^- into $^{210}_{83}$Bi (bismuth), releasing an electrons with mean energies of either 4.2 keV (84%) or 16.2 keV (16%). Additionally Auger or conversion electrons can occur with specific energy, see table 2.1 and the electron emission spectrum fig. 2.13.

Table 2.1.: Electron-emission processes from ^{210}Pb with their corresponding energies with ocurrences > 10% [65].

Process	Energy (keV)	Intensity (%)
β^-	4.2 ± 0.1	84 ± 3
β^-	16.2 ± 0.1	16 ± 3
Auger (L-shell)	8.15	35 ± 1
Conversion (L-shell)	30.152 ± 0.001	58 ± 1
Conversion (M-shell)	42.540 ± 0.001	13.6 ± 0.2

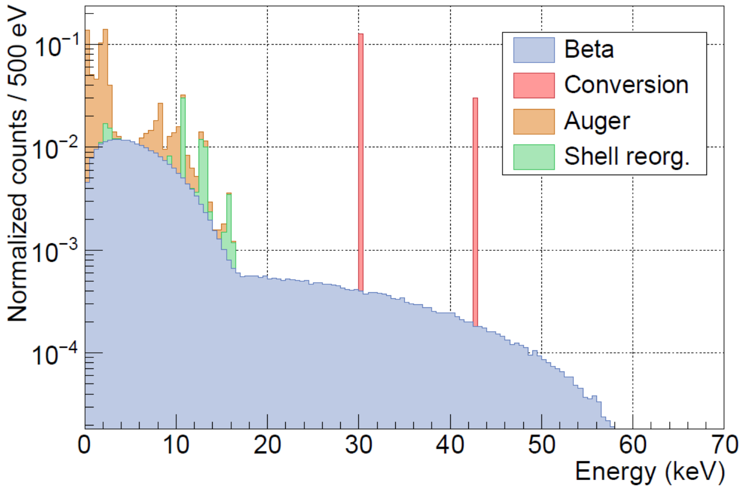

Figure 2.13.: ^{210}Pb electron energy spectrum, including β^- (blue), internal conversion (red), Auger (orange), and shell-reorganisation (green) [48].

Continuing the SDS-II phase in standard mode, more background investigations were planned and performed. To further validate the presence of ^{210}Pb more significant electron energies had to be verified. The reason why this signature was not seen during the SDS-I phase is that, the L-shell conversion electron energy is in the same region as the double arrival of two electrons within the detectors time resolution for the nominal setting of main spectrometer voltage $U_0 = -18.6\text{kV}$, post-acceleration voltage $U_{PAE} = +10\,\text{kV}$, and the detector bias voltage $U_{bias} = +0.12\,\text{kV}$. The energy difference between double arrived and L-shell conversion electrons from ^{210}Pb is about 1.5 keV so the peak could not be resolved within the energy resolution of the detector. Lower post-acceleration measurements (fig 2.11b) revealed the L-shell conversion electron adjacent to the two-electron peak and the M-shell conversion electron peak, respectively [48]. Newer measurements with different settings clearly validate the presence of ^{210}Pb and corresponding electrons [66]. In addition to the signature of the conversion electrons, there is also another indication of the presence of ^{210}Pb. Cluster events with a specific time-structure whose origins will be explained as part of the background characteristics in sec. 2.2.5.

Contamination with ^{210}Pb as part of the uranium-238 decay chain and the intermediate of radon-222 must have occurred after the construction of the main spectrometer. Since it has been electro-polished (see sec. 3.3), whereby such contaminants are efficiently removed, ^{222}Rn from the ambient air has adsorbed on the surface and disintegrated. This puts ^{222}Rn back in the spotlight as a background source. Fabian Harms [48] appreciated the contamination, more precisely, the activity of ^{210}Pb over the time that the spectrometer was filled with air during the installation of the inner electrode. He also compared simulated with measured data of 30 keV conversion electrons starting from the spectrometer surface and the inner electrode, whose dimensions are about 1240 m^2. He calculated the ^{210}Pb-activity from the data to $\sim$ 1 kBq as a rough estimation, which is ten times smaller compared to the overall activity from the ambient air during the installation. This number thus serves as a guide to the rate of these background processes.

Due to the fact that the background is not fully understood yet, there is another framework in which measurements are attempted to be reconciled with simulations in order to obtain a consistent picture of the formation of the background. This framework forms the constantly evolved Rydberg background model (sec. 2.3), in which ^{210}Pb plays a major role.

2.2.5. Characteristics of the remaining background

The remaining background that is, background of unknown origin has properties that need to be known to build up a reasonable model. Since the background is about 50 times larger than the design value of 10 mcps [60], much more interest was directed towards the background. This has led to increased investigations that revealed important properties of the background.

Figure 2.14 shows the spatial distribution of the background. On the detector event representation, one can easily see the radial dependence, an increasing rate to outer rings. An azimuthal dependence is also visible, pointing out an elevated rate at the upper left with an decreased rate in the bottom right. This behaviour can be explained by a slight misalignment of the beamline, inducing a shift of the magnetic flux tube. Therefore more secondary electrons from the spectrometer wall were measured due the magnetic flux tube is closer to the wall. The background rate, normalised to the volume each ring observes with their corresponding flux tube radii, shows two advantages. On the one hand, measurements with different magnetic field settings can be compared directly, while on the other hand, each ring observes a volume of different size which is now taken into account.

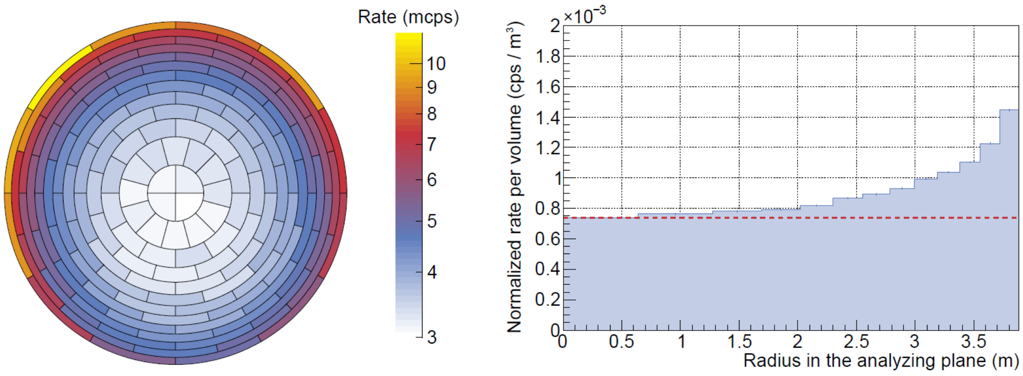

Figure 2.14.: Detector event distribution of the spectrometer background in the standard ROI with cold baffles. Data set N2 (app. tab. A.1) from SDS-IIa to analyse the spatial background distribution. On the left side one can see the background rate per detector pixel. It shows a radial and azimuthal dependence. On the right side, the background rate is shown in a detector ring-wise representation. The rate on a particular ring is normalised to observed flux tube volume and scaled to the corresponding radii of the flux tube in the analysing plane. The dashed red line demonstrates two different background contributions: 75% of the total rate is constant throughout the whole volume, while 25% make up a radially increasing proportion [48].

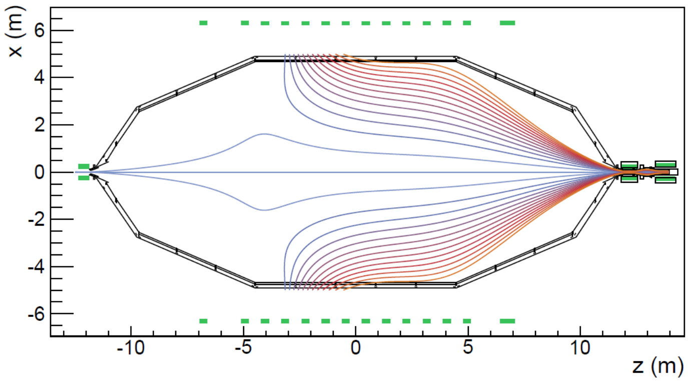

Figure 2.15.: Asymmetric magnetic field configuration to guide secondary electrons from the spectrometer surface to the detector. The color indicates the ring boundaries on the detector wafer from innermost (blue) to outermost (red) [48].

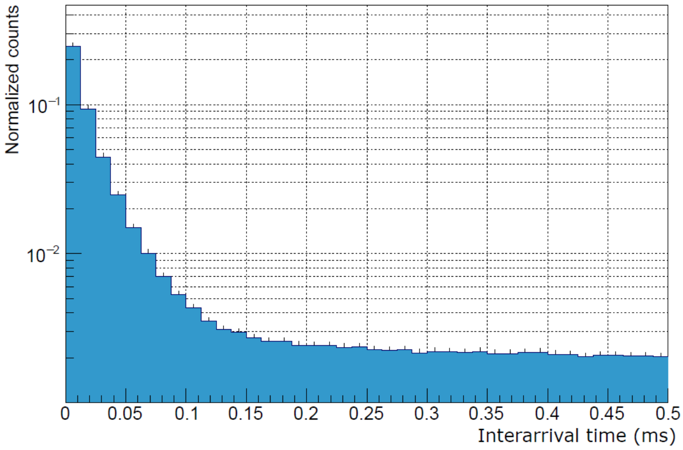

Figure 2.16.: The interarrival time distribution of consecutive electron events arriving at the detector. Correlated events can be found for times smaller than 0.2 ms as their trend is non-exponential. In contrast, the distribution shows a Poissonic behaviour for larger times, indicating no correlation [67].

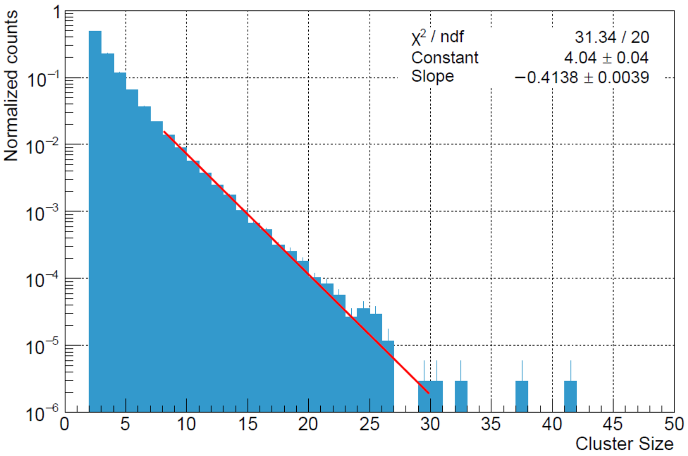

Figure 2.17.: Correlated events within 0.2 ms grouped in clusters. The cluster size scales as an exponential, so a stochastic selection process is assumed [67].

The dominant proportion of the background, with 75%, appears to be homogeneously distributed throughout the whole volume, while 25% consists of a radially increasing part that can be explained by secondary electrons from the wall, diffusing into the flux tube.[48]

The rising rate to higher radii is explained by accidental cluster events whereby detected electrons are correlated with their interarrival time. This is explained in the following.

To further investigate secondary electrons from the spectrometer surface an asymmetric configuration of the magnetic field (fig. 2.15) was set at the SDS-IIb phase. With this configuration it is possible to guide electrons from the inner surface to the detector and measure their energy and rate. A surface area of about 250 m^2 can be mapped onto the detector [48]. This procedure is necessary to collect more statistics of secondary electrons from the wall, at the normal setting only a few electrons could diffuse into the flux tube, the others are magnetically guided back to the wall.

Figure 2.16 shows the results of interarrival time measurements. Within a short time of 0.2 ms several events can be correlated as their distribution is not exponential. Above 0.2 ms the distribution corresponds to Possion-distributed single events and is therefore uncorrelated. The increased rate for small times can be interpreted as the detection of more electrons within a short time. Such an event is called a cluster event. To separate these cluster events from single events, an algorithm was invented for radon-induced background events which are proposed to be the major source of cluster events [48]. The algorithm counts events within a certain time Δt, if there are no more events the cluster is complete. This results in a distribution of counts in comparison to their cluster size, fig. 2.17. However, the cold baffles suppress radon-induced background to a minimum of about 36 ± 18 mcps, which does not match the measured background rate and cluster presence.[67]

Cluster sizes with up to 40 events were not expected, while the magnetic mirror effect of the MAC-E filter strongly suppresses large cluster sizes [67]. A combination of random two or more events at the same time can not be excluded in special cases. The events are not spread arbitrarily on the detector, but instead the pixel distribution of these events has in general two types. Firstly, the cluster events are packed together at adjacent pixels. Secondly, two separated areas of adjacent pixels with smaller clusters are traced, as shown in fig. 2.18.[67]

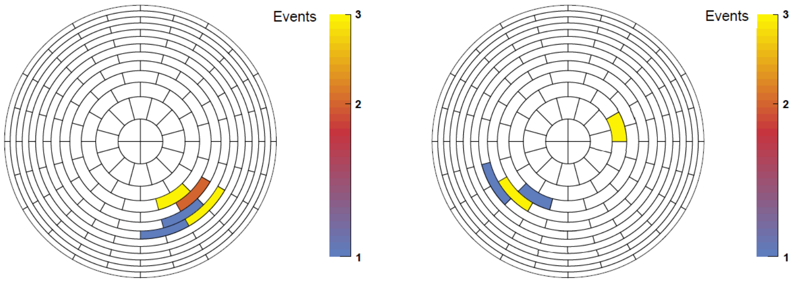

Figure 2.18.: Typical cluster event distribution on the focal plane detector demonstrating the two types of event displays. On the left hand side the packed together cluster event. On the right hand side, a cluster event with two separated areas of hit pixels. Modified by using the template of [67].

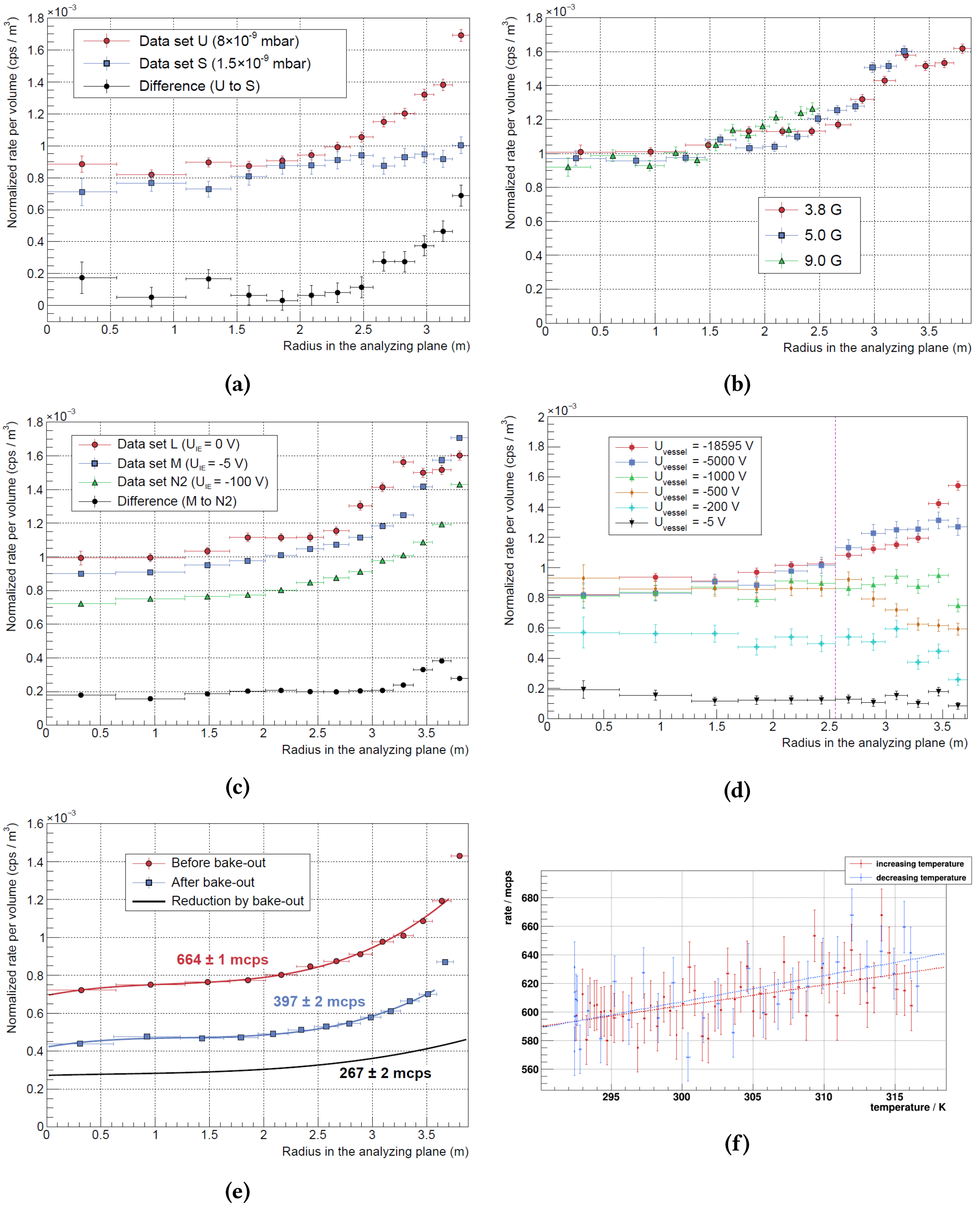

(a)

(b)

(c)

(d)

(e)

(f)

Figure 2.19.: Radial background distributions (**a**): for elevated pressure (U) and medium pressure (S) at the 5 Gauss setting. For data sets U and S, see tab. A.2 [48]. (**b**): for various symmetric magnetic field settings. For data sets L, P, and Q, see app. tab.A.3 [48]. (**c**): as a function of the inner electrode potential. For data set L, M, and N2, see app. tab. A.1 [48]. (**d**): at different spectrometer vessel potentials [48]. (**e**): Influence of a vacuum bake-out procedure on the spectrometer background. For data set N2 from SDS-IIa (red dots) and from SDS-IIb runs ♯24627 - ♯24671 (blue rectangles) [48]. (**f**): Background rate for increasing and decreasing temperature [51].

As mentioned before cluster events can also be explained by the presence of ^{210}Pb. Under the assumption the radioactive lead isotope decays in the spectrometer vessel wall and generates electrons, the remaining ^{206}Pb ion may leave the wall and propagate through the spectrometer volume, causing electrons directly or indirectly upon impact with the steel.

To further discuss the background characteristics, measurements depending on the pressure (fig. 2.19a), the magnetic field (fig. 2.19b), the inner electrode potential (fig. 2.19c), the spectrometer resolution (fig. 2.19d), the bake-out procedure (fig. 2.19e) and the temperature (fig. 2.19f) are taken into account.

The radial background rate for different pressure conditions (fig. 2.19a) shows an increased rate at the outer flux tube regions, whereas the inner region only slightly increases. This may be due to an increased inflow of electrons from the wall into the flux tube. Low energy secondary electrons are confined to small cyclotron radii and would therefore not enter the flux tube volume. However, the scattering probability of the electrons increases with the pressure, whereupon they can be scattered into the flux tube. Nevertheless, the increased rate at the edge of the flux tube, up to one meter into the spectrometer, can not be explained by these secondary electrons.[48]

The radial profiles of the background for different magnetic field settings (fig. 2.19b, app. tab. A.3) appears similar, apart from smaller fluctuations caused by azimuthal dependencies. Due to higher magnetic fields the radial flux tube dimension decreases and low-energy electrons are more efficiently shielded. This similarity was an unexpected observation, which implies that the non-radon induced background scales with the volume of the flux tube. The conventional background model based on secondary electrons from the vessel wall stands in contradiction to this observation due to the consequence that the electrons originate homogeneously distributed over the volume of the spectrometer.[48]

Figure 2.19c illustrates the influence of the inner electrode voltage on the radial background rate. As predicted the rate decreases with increasing inner electrode voltage, but not as much as expected. Excluding the distortion in data set L for $U_{\mathrm{IE}} = 0\,\mathrm{V}$ impinged by inhomogeneous electric fields, the three distributions show the expected radial behaviour as in fig. 2.14. In addition the difference of the data sets M and N2 are shown, which remains constant up to 3 m and increases to the outer flux tube region, which is explained by the more effective electrostatic shielding. However, the distribution of the inner rings does not match the expectation. Electrons with medium energies ($E < 100\,\mathrm{eV}$) from the vessel surface can only reach the inner flux tube volume via a 2-stage process [52]. An electron needs to be stored in the outer flux tube regions and has to experience a slow drift towards the spectrometer axis due to non-axially magnetic and electric fields. This stored drifting electron ionises residual gas molecules and generates background electrons. However, the time scale of the drift into the inner volume is much larger than the corresponding storage time of these electrons. Thus, the storage condition is broken before electrons could reach the inner volume and the rate is expected to decrease significantly radially to smaller radii. The inconsistency of this minor constant background suppression opens questions about a novel effect.[48]

Another finding belongs to the main spectrometer high voltage, or the resolution, respectively (fig. 2.19d). The background rate barely decreases with decreasing high voltage, or worse resolution untill the absolute voltage drops below $-500\,\mathrm{V}$ where the reduction is significant. Some measurements were performed with asymmetric magnetic field settings, so the outer rings ($r \gtrsim 2.5\,\mathrm{m}$) are not taken into account. The relative background reduction also remains constant over the volume, resulting in no explanation for this observation. This is ongoing research by N. Trost and A. Pollithy.[48, 66, 68, 69]

Between the SDS-IIa and SDS-IIb phases, a vacuum bake-out procedure (fig. 2.19e) was successfully performed. By heating the spectrometer vessel, adsorbed molecules on the surface, such as H_2O, can be removed and improve the surface conditions. This procedure led to a background improvement of about 20%, but the same radial shape and brings up the assumption that the remaining background is related to the surface conditions.[48]

The temperature also indicates a dependence on the background rate (fig. 2.19f). The rate was measured for increasing and decreasing temperature resulting in a normalised slope of $0.79 \pm 0.12\,\mathrm{mcps/K}$ with a correlation factor of 0.6. This will be discussed as an indicator of the Rydberg background model in sec. 2.3.[51]

Modifying the steep cone electrode U_{SC} or the post-acceleration voltage U_{PAE} showed no effect on the background rate [48]. Active countermeasures have complementary shown that the remaining background does not result from stored electrons of radioactive decays [51].

In addition, special dipole measurements were implemented to study the starting energies of stored electrons [69]. By applying a Penning trap (fig. 2.9) inside the main spectrometer and increasing the depth of the trap stepwise, electrons with different starting energies can be separated. Subsequently, an electric dipole pulse is applied so that the trapped electrons are removed from the system. By the comparison of the rate reduction at a specific trap depth one can obtain the amount of electrons with starting energies in the region of the trap depth. In the same manner electrons get trapped magnetically. According to the same principle, electrons are trapped magnetically and their energies investigated and compared with those of the Penning trap. The measurement revealed electron starting energies up to 4.5 eV, whose origin is currently not understood (see fig. 2.20) [68, 69]. However, the Rydberg background model could be the solution of understanding the remaining background of the KATRIN spectrometer.

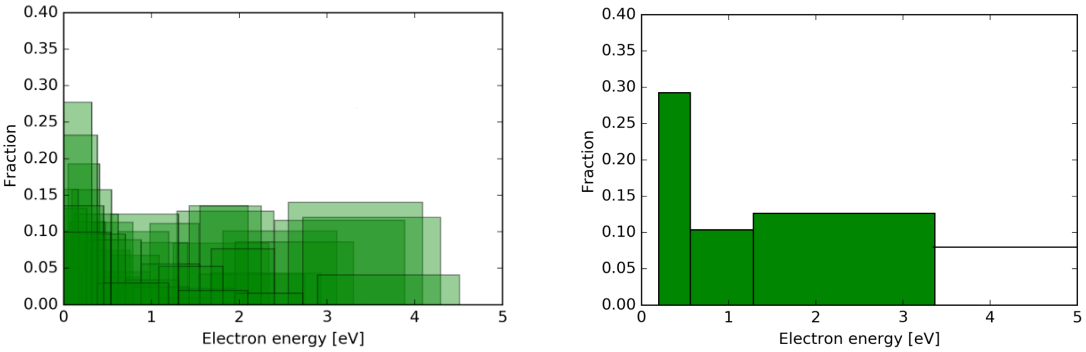

(a) (b)

Figure 2.20.: Electron starting energies determined via (a) electric trapping and (b) magnetic trapping [69].

2.3. The Rydberg background model

The Rydberg background model describes an extension of the background sources in the KATRIN main spectrometer. As already mentioned, the background has various characteristics that are incompatible with previous considerations and studies. Consequently, a model had to be developed, which could explain some or all of these characteristics. The motivation of the model is mainly based on the measurements of the dependence of the background on the inner electrode voltage (fig. 2.19c), the pressure (fig. 2.19a) and the magnetic field (fig. 2.19b). These measurements revealed a nearly pressure independent background source, which has a lower dependence on the inner electrode voltage than expected and is also constantly distributed over the entire volume.

Rydberg atoms are highly excited atoms in states of high principal quantum number n [70, 71]. They were named after the Swedish physicist Johannes Rydberg, who developed the well-known Rydberg formula - the correlation of the wavelength with the principal quantum number [72]. The Bohr model [73] is useful to explain some properties of these atoms such as their size. The orbital radius

$$r_n = \frac{4\pi\epsilon_0 n^2 \hbar^2}{Z m_e e^2} \tag{2.3}$$

depends on the principal quantum number n^2 with $\hbar$ - reduced planck constant, ϵ_0 - vacuum permittivity, e - elementary charge, m_e - electron mass, and Z - atomic number. This leads to the scaling of the geometric cross section $\sigma \propto n^4$. In general, the radius depends on n and the angular momentum quantum number l. The solution of the radial part of the Schrödinger equation $R_{n,l}$ and the total hamiltonian is characterised by three quantum numbers (n, m, l) [74]. The smallest possible orbital radius at $Z = n = 1$ for a hydrogen atom is called the Bohr radius

$$a_0 = \frac{4\pi\epsilon_0 \hbar^2}{m_e e^2} = 5.29 \cdot 10^{-11}\,\mathrm{m} = 0.529\,\mathring{A} \quad .$$

Therefore, a hydrogen atom with a principal quantum number of $n = 10$ results in a 100-times larger orbital radius of $r_{10} = 5.29\,\mathrm{nm}$, and a geometric cross section of $10^4 a_0^2$ [71]. The binding energy of the electron decreases with increasing principal quantum number due to the larger radius, while the Coulomb force from the nucleus weakens. The energy relation for hydrogen and hydrogen-like ions is given by

$$E_n = -\frac{Z^2 Ry}{n^2} = -\frac{Z^2 hcR_\infty}{n^2} = -\frac{Z^2}{n^2} 13.6\,\mathrm{eV} \tag{2.4}$$

with the Rydberg energy $Ry = 13.606...\,\mathrm{eV}$, is obtained from the Rydberg constant $R_\infty = (m_e e^4)/(8\epsilon_0^2 h^3 c)$ [71]. For multi-electron atoms the hydrogenic energy formula changes due to the core penetration (low-l states) or core polarisation (high-l states) to

$$E_{nl} = -\frac{Z_c^2 Ry}{(n-\delta_l)^2} = -\frac{Z_c^2 Ry}{(n^*)^2} \quad . \tag{2.5}$$

Introducing the the effective principal quantum number $n^* = n - \delta_l$, where δ_l is the quantum defect, dependent on the angular momentum quantum number l. The charge of the core is

Z_c [74]. Since the binding energy scales with n^{-2}, highly excited electrons are only weakly bound. These can therefore be easily perturbed or ionised by collisions or external fields. The long lifetime is also an important property of Rydberg atoms. The radiative transition rate can be derived from the Einstein A coefficient for $nl \longrightarrow n'l'$ transitions. The lifetime depends mainly on the highest frequency and the l-state. The transition from low-l states is almost independent from n, resulting in a lifetime-dependence of $\tau_{nl} \propto n^3$. For maximum high l states with $l = n - 1$, only $n \longrightarrow n - 1$ transitions are allowed, giving a $\tau_{n(n-1)} \propto n^5$ scaling [74]. By averaging the corresponding decay rate of all l, m states of same n, one obtains the useful expression $\tau_n \propto n^{4.5}$ [75].

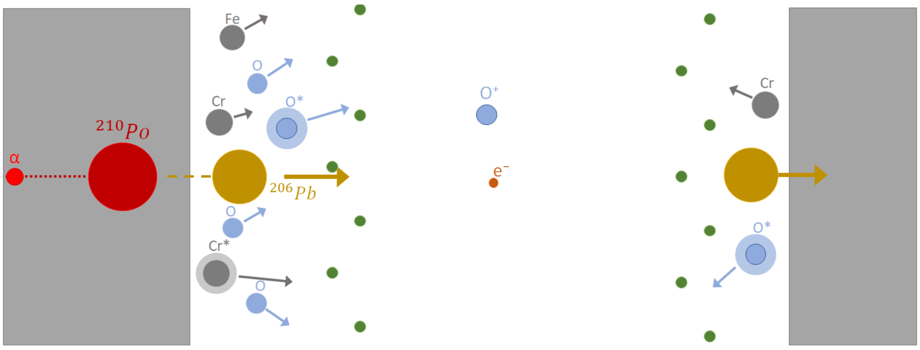

Figure 2.21.: Illustration of sputtered atoms, Rydberg atoms, and background electrons by the radioactive decay of ^{210}Po (red). The stainless steel and atoms from the steel such as Fe and Cr are shown in grey. Oxygen atoms are shown in blue, the remaining lead-ion in yellow, while the inner electrode is demonstrated in green. Excited or metastable atoms are marked with * and are surrounded with an extended area.

The Rydberg atoms in the KATRIN main spectrometer are assumed to originate from the spectrometer vessel wall due to the radioactive α-decay of implanted ^{210}Po, a daughter of ^{222}Rn (see fig. 2.12), illustrated in fig. 2.21. While the remaining ^{206}Pb-ion propagates through the stainless steel vessel it scatters and may atomise atoms of the steel. Atomisation describes the release of an atom from its compound and the lattice. Some of these atomised atoms may scatter on other atoms and some leave the vessel surface and propagate into the main spectrometer volume, which is called sputtering (see sec. 3.1)[76, 77]. The ^{206}Pb-ion may also leave the vessel steel and can sputter atoms again as it hits the opposite side of the spectrometer wall. These sputtered atoms have the ability to be in highly excited or metastable states [78–80] and since they are neutral, they are not affected by the inner electrode so they can pass the wire electrode.

First assumptions of this model included the excitation to Rydberg states of hydrogen molecules, which are adsorbed at the inner spectrometer surface. Followed by the ionisation of thermal radiation of the spectrometer vessel (see sec. 4.1). However, the bake-out procedure efficiently removes adsorbed atoms on the surface because they are not chemically bound. Additionally, if the remaining background would only consist of these hydrogen Rydberg atoms, the spectrometer bake-out would have led to a more drastic reduction. Likewise, the ionisation by the black body radiation (BBR) is not satisfactory. As will be explained in sec. 4.1, the energies of BBR-ionised electrons are on the order of meV, up to two orders of magnitude too low. Figure 2.20 shows that electrons with energies up to 4.5 eV have to be generated and therefore other ionisation mechanisms have to be taken into account.

Furthermore there are restrictions on the properties of the Rydberg atoms. Rydberg atoms origination from the vessel surface have to be in a long-living state, thus the constant background density can be explained - ionisation has to occur constantly distributed over the entire volume. On the other hand their excitation has to be low enough that they are not immediately ionised by the electric field between the vessel wall and the inner electrode (see sec. 4.3). In addition, the ionisation process must not occur by the collision with residual gas atoms, since the background rate does not have the appropriate pressure dependence (see sec. 4.2). Metastable autoionizing states are the best candidate to explain the measured electron energies, but are unlikely to provide the necessary lifetimes (see sec. 4.4).

To prove some investigations corresponding this model, a radioactive ^{228}Th source was attached to the main spectrometer. ^{228}Th is part of the ^{232}Th decay chain (see app. fig. A.1). The half-lifes of the daughter nuclei are smaller than 3.6 days corresponding to ^{224}Ra, which prevents permanent contamination. While the source was attached, daughter nuclei of the source will get implanted into the main spectrometer vessel stainless steel. The intermediate ^{212}Pb provides a suitable half-life of 10.64 ± 0.01 h to measure its activity properly. The background measurements (app. fig. A.3) were performed with symmetric and asymmetric magnetic field settings. Both verified the expected half-life of ^{212}Pb very well [81]. A strong correlation between the electrons starting from the wall and the inner volume was observed (see fig. 2.22). This observation manifests the presence of a common background process of electrons originating from the wall or the inner volume.

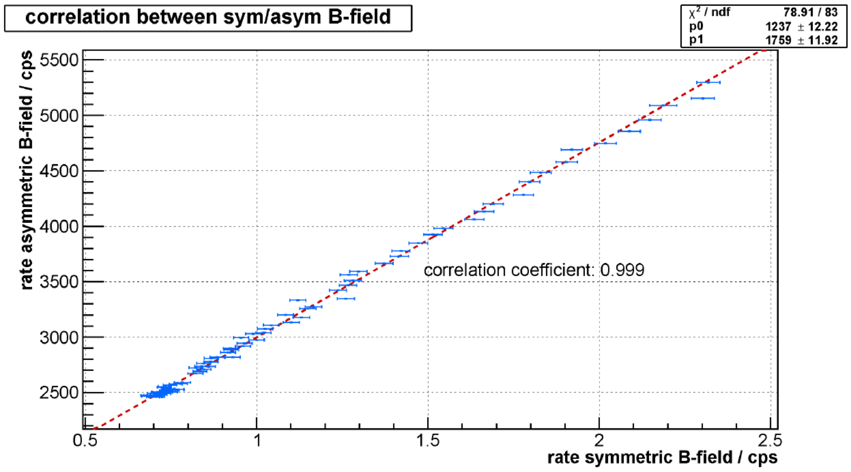

Figure 2.22.: Comparison of the rates for symmetric and asymmetric magnetic field setting of the thorium measurements [51].

3. Simulation of sputtered atoms from the main spectrometer hull

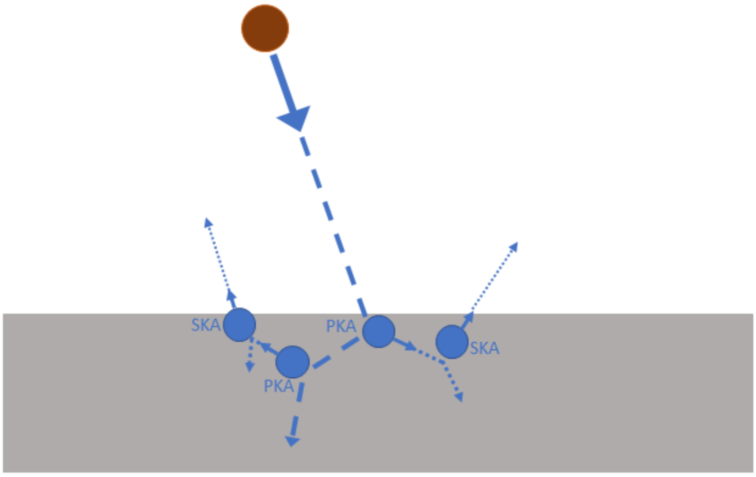

Figure 3.1.: Illustration of sputtering process. Incident ion (brown) creates collision cascade in material (grey), causing two atoms (blue) to escape. PKA - primary knock-on atom by the ion, SKA - secondary knock-on atom by another atom.

Sputtering describes the removal of atoms from the surface of solids or liquids by bombardment of particles with energies from eV to MeV. Besides the interaction of the incident particle - atom, ion, molecule etc. - with solid surfaces, many secondary processes occur, such as neutralisation, excitation or ionisation, backscattering and implantation. Due to erosion by removing surface atoms, the morphology of the surface gets modified. Ion bombardment further causes the emission of electrons and of photons causing radiation damage on the surface layers [77, 82]. At that, sputtering is not limited to incident particles but also occurs with particles emerging within the material.

Based on ideas and simulation of our colleague A. Osipowicz [126] it is commonly assumed that recoiling ions from radioactive decays within the KATRIN main spectrometer vessel wall cause the sputtering of atoms related to the unknown background source. He provided first considerations on this topic, which is the main motivation of this work.

The following section describes the theoretical basis of the sputtering process, as well as the software SRIM used for simulation. The conditions of the main spectrometer were studied and transferred to the simulation to obtain a more precise model of the sputtering process and its characteristics as a further development of A. Osipowicz's work.

3.1. Theory of sputtered particles

Figure 3.1 illustrates the mechanism of sputtering processes. An incident ion of certain energy hits in a target, causing target atoms to escape their lattice binding due to inelastic kinetic energy transfer. These atoms hit other target atoms again and these can be released from the material. This is generally called a collision cascade and the amount of sputtered particles depends on various parameters. It obviously depends on the starting energy, the charge and the mass of the incident ion, but also on the target solid [83]. The atoms of the material are in a lattice arrangement, which leads to a certain lattice binding energy of each atom. This energy must be overcome in order to be able to knock on other atoms. Likewise, the impacted atoms must overcome a surface binding energy to escape from the material.

The first model of this process was invented by Thompson in 1968 [84–86]. He measured the kinetic energy of ejected particles by bombarding gold with argon and xenon ions with energies of 43 keV or 66 keV. He established some properties of the energy spectrum of sputtered particles. He derived under the assumption of an inverse squared collision potential $V(r) \propto r^{-2}$, the energy spectrum. It shows a peak near the surface binding energy U and decreases for higher energies as $\propto E^{-2}$. The full theoretical description of the sputtering process was developed by Sigmund in 1969 [76]. Via solving differential equations and the Boltzmann transport equation, he invented several equations that describe the sputtering yield such as the energy or the depth of origin of sputtered particles. Further he directly connected the energy spectrum with the surface binding energy U, his energy differential sputtering yield is

$$\frac{dY}{dE} \propto \frac{E}{(E+U)^{3-2m}} \quad . \tag{3.1}$$

The parameter m corresponds to a model interaction potential $V(r) \propto r^{-1/m}$ [87].

More interest was devoted to the sputtering process such as the investigation of the atomisation of molecules or clusters, and also their rotational and vibrational movement [88–92]. Behrisch and Eckstein concluded the past efforts to complete a set of equations describing the sputtering process and its properties [77]. The most important one is the approximation of the differential sputtering yield

$$\frac{\partial^3 Y \Delta E \Delta\Omega}{\partial E \partial^2 \Omega} = Y(E_0, \theta_0 = 0)\frac{2}{\pi}(1 - 3m + 2m^2)\frac{U^{1-2m}E}{(E+U)^{3-2m}}|cos\theta|\Delta E \Delta\Omega \quad . \tag{3.2}$$

$Y(E_0, \theta_0)$ is an approximate algebraic formula for the dependence of the sputtering yield on the bombardment conditions. It depends on the nuclear energy deposition function F_D, which is proportional to the nuclear stopping power $S_n(E_0)$ of the incident ion in the solid. As mentioned before, m is a parameter of the approximate solutions of integral transport equations for the atom-atom collisions potential $V(r) \propto r^{-1/m}$ with $0 \leq m < 0.5$. U is the surface binding energy whose value is usually set equal to the heat of sublimation since the surface binding energy is generally not well known. Its value is in the range of $1 - 10$ eV.[76, 77]

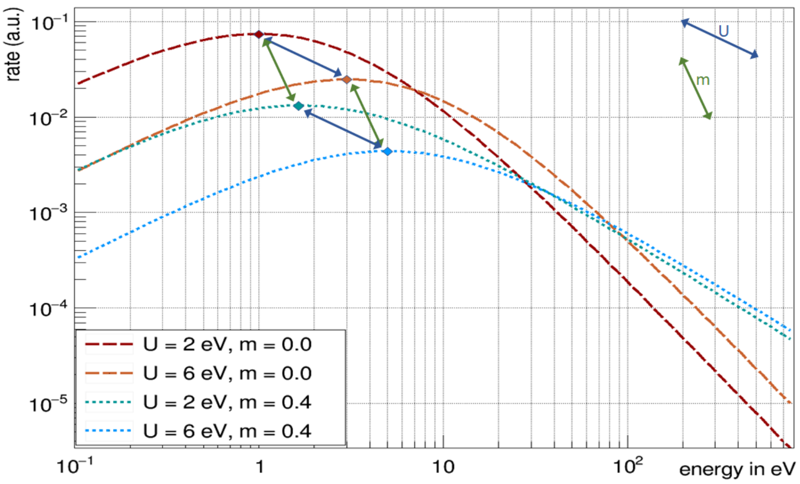

Figure 3.2.: Energy spectrum of the sputtering process. The model function is presented by $Y(E,U,m) = c \cdot (1 - 3m + 2m^2)\frac{U^{1-2m}E}{(E+U)^{3-2m}}$, where c is a constant (here $c = 1$). The plots are made with different surface binding energies U and parameters m. The maxima are marked with colored squares. The influence of changing one parameter is also shown in the top right corner.

Figure 3.2 shows the theoretical energy spectrum depending on the surface binding energy U and the model parameter m. It also illustrates the significant characteristic of the spectrum, the peak position, depending on the parameters. By deriving $Y(E,U,m)$ one obtains the peak position as the zero of the derivative:

$$\frac{dY(E,U,m)}{dE} \equiv 0 \quad \longrightarrow \quad E_{\text{peak}} = -\frac{U}{2(m-1)} \quad . \tag{3.3}$$

For $m = 0$ it is equal to the half of the surface binding energy. Another characteristic is the decreased maximum for increased U and m. This belongs to the model function of the energy spectrum, since the integral of different U and m, is always constant:

$$\Upsilon(E,U,m) = \int_0^\infty Y(E,U,m)dE = \left[\frac{U^{1-2m}((2m-2)E-U)}{2(U+E)^{2-2m}}\right]_0^\infty = 0.5 \quad . \tag{3.4}$$

In addition one can see the power-law scaling for higher energies $\gtrsim 50$ eV, where the case $m = 0$ represents Thompson's predicted scaling of E^{-2} [85] and for the limit $m \longrightarrow 0.5$ the power-law scales with $\propto E^{-1}$.

In order to complete the sputtering process, the presence of excited or metastable sputtered particles is also taken into account. These could be the main background source at the KATRIN main spectrometer.

Since sputtering is investigated, many theories and models came up to explain the measured energy spectra of sputtered atoms. However, after excited atoms were detected, flaws in the models were constantly detected. The models did not provide reliable forecasts and had to be revised. During the 1980s many scientist tried to establish a unified theory of sputtering, which should explain measurements comprehensibly. First investigations referring to the yield of excited sputtered atoms in comparison of the yield of neutral ground state atoms and ions indicated that the population of excited atoms possess higher mean energies than the neutral ground state ones. This lead to the assumption that the excitation of sputtered atoms only occurs in the far tail of the energy spectrum, resulting in a small population. This and the comparison of the sputtering yield of secondary ions (10^{-1}–10^{0}) with excited atoms (10^{-4}–10^{-2}) infers the supposition that the excitation process results from a different effect than the ionisation. Thus, ionisation is not a special case of excitation [93]. Roger Kelly [78, 94] has developed a theoretical framework to explain the sputtering yields of sputtered neutral ground state, excited, ionised, and molecular species. His theory is based on the inelastic energy transfer at collisions. He relates it to the earlier investigations that the excited sputtered particles mainly get generated towards the high energy tail. The formation of these excited atoms by resonance neutralisation of ions is ruled out due to the high energies they allegedly have. During his work he pointed out that excitation is only relevant for the outermost first and second atom layers, as excited atoms in the solid rapidly dissipate. Earlier studies of sputtering atoms from cleaned and oxidised metal surfaces revealed a correlation of the excitation process with the deposit of oxygen - the oxygen effect [78, 95]. It was shown that the yield generally increases, while decreasing the ground state population. The mean energy of the sputtered atoms shifts to higher energies by a factor of $3-5$ and higher excited states were present. Also the population of ions and metastable sputtered atoms with excitation energies $\sim 1\,\mathrm{eV}$ increased by an order of magnitude in analogy to the short-lived excited ones. The oxidised metal surfaces resulted in the release of a large fraction of metal oxide quasi-molecules. However, this behaviour was very different for different materials, sometimes the mean energy increases, but it can also decrease or hardly change [95]. Likewise, the angular distribution of oxidised and cleaned metal surfaced did not fit the model predictions [96]. These findings have made the establishment of an explanatory model very difficult, as it depends on the target compound itself. Nevertheless, although another effect of excitation as by collision was substantiated, the energy spectrum of excited sputtered iron atoms showed the same behaviour as the neutral ground state ones with less mean energy [97, 98]. This led to the removal of the previous assumption that the excited atoms are not generated in a common process with the normal sputtered atoms. The excitation process or the presence of excited sputtered atoms did not fit the models, but other scientists developed the models. As it was now common that the excited sputtered atoms have the same origin as the neutral ground state atoms, more information must be extracted from the collision process [79]. Based on binary inelastic collision, the limiting angle of recoils as well as the cross-section of excitation can be derived [99]. An important theoretical description was developed by Konoplev [100], where a general formula for the minimum transfer energy threshold was established. In a collision cascade, only inelastic collision can excite atoms, which is a small fraction. A recoil has to gain a minimum energy transfer in order to be in a excited state. Therefore, excited atoms recoiling with low energy can only be set in motion by high energy particles [100].

However, all these efforts have still not lived up to some observations. A. Wucher measured a high population of excited metastable sputtered silver atoms [80] with excitation energies up to 3.75 eV, which was not expected, whereupon he concluded with Z. Sroubek a new model of the excitation process [101]. The formation of the excited state due to the electron promotion of binary collisions between the target atoms cannot explain the high excitation probability, they observed for sputtered metastable Ag atoms. So they assume that the sputtered atom ‘copies’ the equilibrium electronic state of the solid, which can be modified by collisional excitation [101]. The concept predicts the creation of *d* holes by energetic collisions, which are screened by the conduction electrons, thus forming the excited atom. This excitation propagates through the solid and is transferred to a sputtered atom, resulting in a neutral excited Ag atom [77]. For other metals a high population of metastable excited sputtered atoms with low kinetic energy was also observed leading to the conclusion that the emission of excited atoms is caused by multichannel resonant electron transfer (RET). This process describes the sputtered atom leaving the surface as a positive ion and becoming neutralised into an atomic state by resonant transfer of an electron from the valence band of the metal, i.e., a nonadiabatic tunneling of the electron [77].

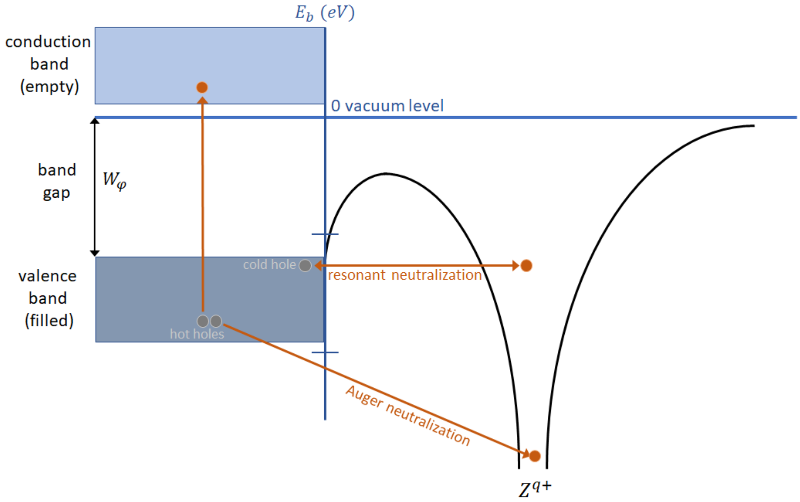

Figure 3.3.: Electron transitions between surface and projectile ion leading to formation of holes (via resonant neutralisation) as well as electron-hole pairs (via Auger neutralisation). Figure adapted from [102].

Electron exchange processes at metal surfaces play an essential role in many surface-analysis techniques [103, 104] and they are investigated in experimental and theoretical studies. Two basic charge transfer mechanisms between atoms or molecules and a solid are known [105]. On the one hand resonant electron transfer and on the other hand Auger processes, see fig. 3.3. At resonant electron transfer the energy level of the atom is in resonance with the continuum states of the solid [105]. The general approach in describing this resonant charge transfer in scattering atoms from a metal surface is based on a solution of the Anderson-Newns Hamiltonian [104]. The metal electrons are described by free waves inside a potential box with a depth equal to the sum of the work function W_ϕ and the Fermi energy. The atomic level shifts due to the interaction with image charges, induced in the metal. As a consequence of the attraction to its image charges, the effective ionisation potential decreases and an electron from the solid can tunnel into the atom and vice versa as one-electron process.[104, 106]

Besides that, Auger processes are two-electron ones and are fundamental at the ion(atom)-surface interactions as well [102, 105, 107, 108]. The Auger Neutralisation (AN) describes a process, whereby one electron from the surface is transferred to a bound state of the atom, while another becomes a surface excitation due to electron-electron interaction. In addition the inverse process of Auger ionisation (AI) can occur, where an electron is transferred to an energy above the Fermi energy with the generation of surface excitation, needing kinetic energy of the atom because of energy conservation. Also Auger Deexcitation (AD) has to be considered. Here an initially excited state decays into the ground state under electron emission, directly or indirectly. The direct process is without electron exchange from the atom or molecule to the solid, the excited electron decays into the ground state, transferring energy to a solid electron causing an surface excitation or emission. Indirectly, an electron from the solid decays into the ground state of the atom, so that the excited one gains the energy and gets emitted.

3.2. Software SRIM

SRIM is a software package for the **S**topping and **R**ange of **I**ons in **M**atter [109–111]. Since its introduction in 1985, it continuously evolved and the latest version was published in 2013. With this software one can simulate the propagation of ions in matter and calculate the stopping power in one-atomic targets and compounds. For these calculations the program TRIM (Transport of Ions in Matter) is included, which deals with different methods. Up to eight layers of different size and composition can be set to simulate the propagation. In addition, the final 3D distribution of the ions as well as energy loss by target damage, sputtering, ionisation, and phonon production is provided. For this work the production of sputtered atoms and their distribution, provided by the extension TRIM.SP [112] is of interest. Choosing the TRIM calculation type 'Recoil cascades and monolayer steps (full cascades)', one obtains a detailed calculation of all target atom cascades as well as detailed information of atoms leaving the target, such as their energy, exit angle, position, and chemical element.

The basic principle is to follow the primary ion, while it moved either into or out of the target. Every particle, recoil atom, or ion is tracked until it either leaves the target or its energy has fallen below a certain threshold. The collision cascades are now considered by following the primary knock-on atom (PKA). The PKA may knock on another atom - SKA (secondary knock-on atom), leave the target, or fall below the energy threshold. In case of a secondary knock-on, now the SKA will be tracked untill one of the termination conditions are fulfilled. If all secondaries are treated, the primary ion is followed up and the procedure restarts.[112]

The collisions are classically described by elastic binary collisions by an interaction potential, depending on the energy - binary collision approximation (BCA). Hereby the energy loss to electrons can be handled separately as an inelastic energy loss [77]. The scattering angle in the center-of-mass system is determined by an integral of the impact parameter p and the interaction potential $V(r)$ with energy and momentum conservation:

$$\vartheta = \pi - 2p \int_R^\infty \left(\frac{r^2}{\sqrt{1 - \frac{V(r)}{E_r} - \frac{p^2}{r^2}}} \right) dr \quad , \tag{3.5}$$

where r is the distance between the two colliding atoms and R the apsis (closest approach) of the collision [77, 113]. The surface is treated as a randomised target, thus avoiding the lengthy procedure for determining the position of the next collision partner. An atom has to overcome the surface binding energy, which has a significant influence upon the total sputtering yield. In general the heat of sublimation is used as an input. It acts in the form of a planar attractive potential upon the atoms which attempt to leave the surface and cause a refraction or even a reflection back into the solid [112], which causes the maximum of the energy distribution to non-zero (see. Fig. 3.2). In general the surface binding energy is not known, especially as it depedends on the surface topology. Therefore, the application of the heat of sublimation is a good mean value, because these values are determined experimentally, without specific topology. In compound targets, only a interpolation according the compostition can be assumed. The lattice binding energy with an approximated value of $E_{\mathrm{LB}} \sim 3\,\mathrm{eV}$ and a displacement energy of $5 - 30\,\mathrm{eV}$ is also taken into account, specified by the chemical element. The electronic energy loss is calculated via a combination of Lindhard-Scharff and Bethe-Bloch stopping powers, the latter is valid up to relativistic energies.[112]

The major advantages of BCA programs are the speed of calculations in addition to the detailed information about sputtering yield, backscattering, transmission, and radiation damage. The effect of different angles of incidence or energies can thus be quickly calculated and compared, since these programs are about four orders of magnitude faster than molecular dynamics ones. However, they also come with disadvantages, e.g. that a low energy moving atom collides only with one single target atom or the concept of asymptotic trajectories, which is not satisfactory at low energies. The comparison with experimental data actually shows a very good agreement, so that these disadvantages do not influence significantly.[77]

3.3. Composition and surface of the main spectrometer stainless steel

To get reliable information about the sputtering process in the main spectrometer, it is necessary to know the composition of the stainless steel. The material specification of the main spectrometer vessel reads EN 10028-7 - 1.4429 (AISI 316 LN, X2CrNiMoN17-13-3), shown in table 3.1. It consits of an austenitic chromium-nickel-molybdenum stainless steel with additions of nitrogen. This material was selected due to its good results for UHV-technology, permeability, and radioactivity [114, 115].

Table 3.1.: Chemical composition of the KATRIN main spectrometer stainless steel 1.4429, values are given in % (neglecting the traces of P, S and Si) [115, 116].

C	Mn	N	Cr	Mo	Ni	Fe
≤ 0.03	≤ 2	0.17 ± 0.05	17.5 ± 1.0	2.75 ± 0.25	12.5 ± 1.5	balance

Table 3.2.: Chemical composition of the stainless steel and its passive layer for the simulation with SRIM, given in %. Compounds only present in traces or that do not characterise the steels properties are neglected.

	Fe	Cr	Ni	Mo	Mn	N	O	C
Passive layer (35 Å)	15	20	5	0	0	0	50	10
Vessel	64.5	17.3	13.4	2.6	2	0.15	0	0

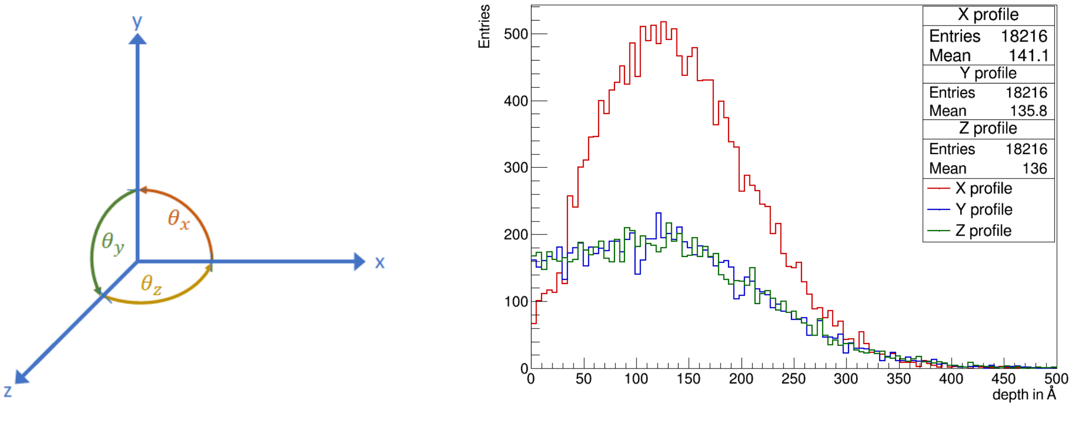

(a) **(b)**

Figure 3.4.: (**a**): Coordinate system of simulations. The x-axis depicts the depth, the y- and z-axis the lateral extension including the directional cosine angles θ_i. The inner surface is therefore placed in the yz-plane at $x = 0$. (**b**): Histogram of the implantation profiles. The X-profile corresponds to the depth (x-axis) of implantation is shown in red. The lateral profiles along y in blue and z in green, respectively.

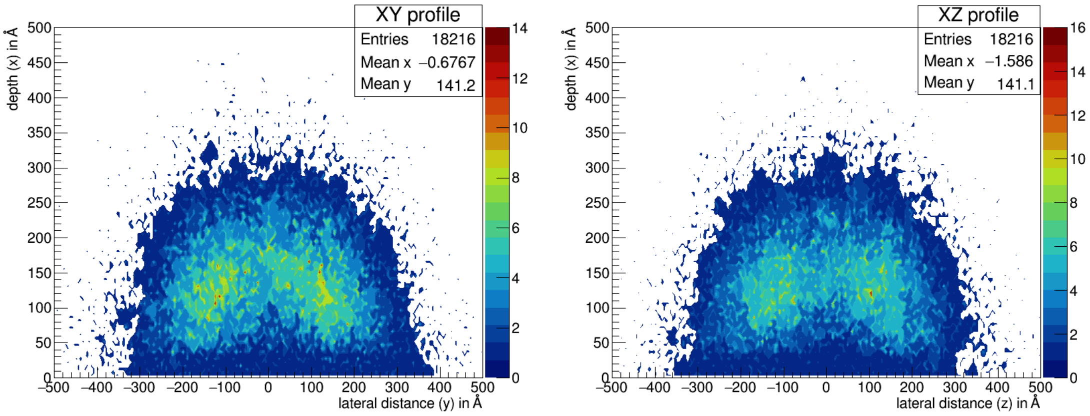

Figure 3.5.: 2D Implantation profiles for the xy- and xz-plane. The colour indicates the amount of implanted particles.

The steel was electropolished after completion. Electropolishing (EP) is a polishing process of electrochemical anodic dissolution. The workpiece serves as an anode, immersed in an electrolyte. Together with a cathode in the solution and a power supply, the metal surface oxidises and dissolves in the electrolyte. Due to this mechanism, a viscous film will be formed on the anode, preventing the increase of the electrochemical reaction efficiency. Lastly a passive layer of smooth roughness is formed, which enhances the corrosion resistance [117]. The effects of EP on the stainless steel 1.4429 have been extensively investigated, giving to the surface composition and passive layer depth with various electrolyte concentrations or currents at different temperature and times [118–122].

The main spectrometer stainless steel was electropolished with DERUSTIT CN 18 [123] for about 20 minutes at $40° - 50°$C. Afterwards it was rinsed and pickled with DERUSTIT CN 15 [124]. CN 18 contains $> 40\%$ phosphoric and $> 35\%$ sulfuric acid, where CN 15 contains $< 25\%$ sulfuric acid without phosphoric.[125]

Concluding the investigations from the literature and the procedure for the main spectrometer stainless steel vessel, one can estimate some characteristics referring the surface structure and the passive layer composition. The passive layer is characterised by a large amount of oxygen, bounded to chromium and iron oxides (Cr_2O_3, Fe_2O_3, FeO). The ratio of chromium to iron changes with the passivation time [122], and the surface roughness is about 15 Å. This information led to the chemical composition of the stainless steel vessel and its passive layer for incorporation into the simulations with SRIM (see tab. 3.2).

3.4. Energy and angular distributions of sputtered atoms

In order to roughly mimic the important sputtering process induced by radioactive decays of ^{210}Po into ^{206}Pb, three simulations were performed. Starting with the implantation of ^{210}Pb via radioactive decay of ^{214}Po into the main spectrometer steel (see fig. 2.12). The implanted particles start under various angles within the stainless steel with a certain energy and cause sputtering. Some of these implanted atoms may leave the vessel steel and may cause sputtering as they hit the opposite site of the spectrometer [126].

During the first α decay (^{214}Po), the energy $Q = 7.834\,\mathrm{MeV}$ is released, corresponding to the kinetic energy of the daughter nucleus to

$$T_{\mathrm{daughter}} \simeq \frac{m_\alpha}{m_{\mathrm{mother}}} \cdot Q \qquad \rightarrow \qquad T_{^{210}\mathrm{Pb}} = \frac{4u}{214u} \cdot 7.834\,\mathrm{MeV} = 146.4\,\mathrm{keV} \ . \tag{3.6}$$

The starting parameters of the ^{210}Pb ions are their position, energy and direction. The energy was set constant to $E_{\mathrm{implant}} = 146\,\mathrm{keV}$ as well as the position to $(x, y, z) = (0, 0, 0)$. The direction is defined by three angles, the directional cosines, see fig. 3.4a. They are defined by the normalised scalar product of the velocity vector $\vec{v}$ with the coordinate axes vector $\vec{e}_i$ $(i = x, y, z)$ and are directly related to the direction of the velocity via:

$$\alpha_i = \cos(\theta_i) = \frac{\vec{v} \cdot \vec{e}_i}{|\vec{v}|} \ , \qquad \vec{v} = |\vec{v}| \begin{pmatrix} \cos(\theta_x) \\ \cos(\theta_y) \\ \cos(\theta_z) \end{pmatrix} \ . \tag{3.7}$$

Table 3.3.: Parameters of the implantation simulation of ^{210}Pb. The starting positions entries are values in Å and the ranges $[a,b]$ for the cosines denote $a \leq \cos(\theta_i) \leq b$ uniformly distributed.

Energy (keV)	Position	$\cos(\theta_x)$	$\cos(\theta_y)$	$\cos(\theta_z)$	Started	Implanted	Backscattered
146	(0,0,0)	[0,1]	[-1,1]	[-1,1]	20000	18216	1784

Table 3.4.: Parameters of the explant of ^{206}Pb, $i = x, y, z$. The first row indicates the first sputtering process of the explantation simulation. The second row relates to the second sputtering process due to transmitted Pb-ions.

Energy (keV)	Position	$\cos(\theta_i)$	Started	Transmitted	Sputtered	Yield (atoms/ion)
103	various	[-1,1]	18216	3523	394885	21.68
various	various	various	3523	–	36633	10.39

The input parameters as well as results of the implantation simulation can be seen in tab. 3.3. 8.92% of the particles were backscattered and therefore not implanted, so 18216 particles are implanted.

Their two-dimensional spread is shown in fig. 3.5 and the 1D distribution in fig.3.4b. The mean depth is 141.1 Å and the mean lateral spread 135.9 Å. Sputtering is not considered during implantation since this occurred when the spectrometer was at ambient air and thus does not contribute to the background.

The implantation profiles define the starting positions of the ^{206}Pb-ions. Table 3.4 shows parameters and results of the second simulation, whereby all directions are taken into account, including the range [-1,1] for $\cos(\theta_x)$, which represents a full 4π-sphere. Two of these cosines are uniformly distributed, defining the third one since the length of the direction vector ($\cos(\theta_x)$, $\cos(\theta_y)$, $\cos(\theta_z)$) has to be equal to one, so each direction has the same probability. The energy is constant at 103 keV, calculated via eq. 3.6 and the corresponding released energy of $Q = 5.407$ MeV. The positions are gathered from the implantation simulation. 6895 of the 18216 implanted particles caused the sputtering of atoms, while 2264 Pb-ions are transmitted into the spectrometer volume. These transmitted particles cause again sputtering as they hit the opposite side, which presents the third simulation. By adding up the sputtering yields, one obtains an overall yield of

$$Y = \frac{431518\,\text{atoms}}{6895\,\text{ions}} = 62.58\,\frac{\text{atoms}}{\text{ion}} \quad ,$$

which is also called the multiplicity of the sputtering process. App. fig. A.4 shows the distributions of the amount of sputtered atoms of the different elements. The amount is not scaled so the entries correspond to the sputtering yield, caused by 18216 initially Pb-ions.

$$Y(U, E, m) = c \cdot (1 - 3m + 2m^2) \frac{U^{1-2m} \cdot E}{(U + E)^{3-2m}} \tag{3.8}$$

is the model function, used to fit the energy distributions of the sputtering yield (fig. 3.6), which are normalised to the number of ^{206}Pb-ions. Each chemical element is fit, resulting in the parameters U and m in app. tab. A.4, the calculated peak position is also shown. Assuming the same interaction potential for all elements, the fits are repeated with the mean of the parameter m with $\overline{m} = 0.24512$, which improved the calculated peak positions (see. eq. 3.3) of oxygen, carbon, and nickel. The fit surface binding energy U as well as its theoretical input, the peak position, and the amount of sputtered atoms can be seen in tab. 3.5. The amount of manganese, molybdenum, and nitrogen is very low, so they are neglected, however, these elements are not present in the passive layer. They propagated through the passive layer and are transmitted, so it is plausible that this also applies to other elements. It can therefore be assumed that the sputtered atoms do not originate only from the surface layer.

Table 3.5.: Number of sputtered atoms, fitting results: parameter U and c at fixed $m = 0.24512$, the theoretical surface binding energy $E_{\mathrm{sub,theo}}$ and the calculated peak position E_{peak}.

Element	Sputtered	U (eV)	c	$E_{\mathrm{sub,theo}}$ (eV)	E_{peak} (eV)
O	235074	0.8635 ± 0.0032	6.759 ± 0.015	2.00	0.572
Cr	70068	2.1527 ± 0.0156	2.001 ± 0.008	4.12	1.426
Fe	54985	2.2893 ± 0.0197	1.469 ± 0.007	4.34	1.516
Ni	17402	2.4084 ± 0.0394	0.477 ± 0.004	4.46	1.595
C	16970	3.5784 ± 0.0595	0.498 ± 0.004	7.41	2.370

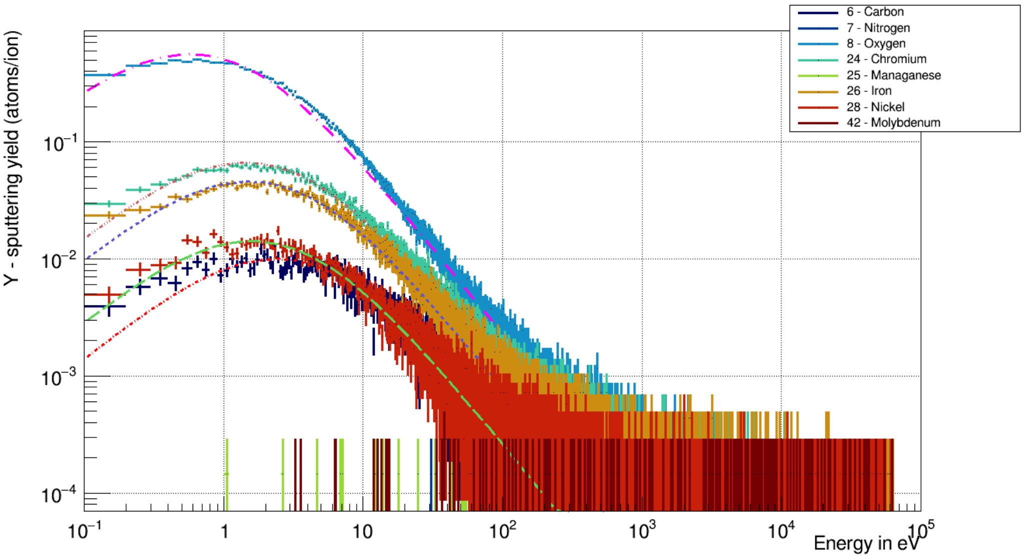

Figure 3.6.: Energy distribution of the first sputtering process, scaled to the total number of contributing Pb-ions (6895) with 0.1 eV binning. Fit with the model function eq. 3.8.

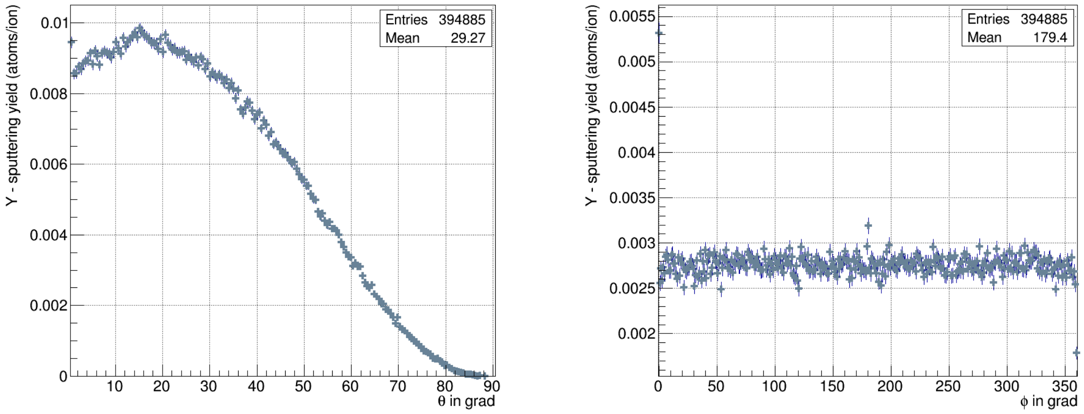

Figure 3.7.: Angular distributions. Polar angular distribution (left) and Azimuthal angular distribution (right), scaled to the total number of contributing Pb-ions.

In contrast to the implantation profile, the coordinate axes (fig. 3.4a) changed to illustrate the angular distributions. The x-axis changed its direction, so a vector with a polar angle $\theta = 0°$ is therefore perpendicular to the surface, pointing into the spectrometer volume. The y- and z-axis remained, $\phi = 0$ is defined to be parallel to the y-axis. The polar and azimuthal angle distributions are shown in fig. 3.7. The azimuthal angle is uniformly distributed from $0°$ to $360°$, the slightly higher rate peaks belong to the direction with $\theta = 0°$, where ϕ is not well defined. The polar angle distribution shows a maximum at $\approx 16°$ and a gaussian-like tail to $90°$. The element-wise representation of the polar angular distribution is shown in app. fig. A.5.

Additional plots can be found in app. A.2, such as the energy and angular distribution of the transmitted Pb-ions app.fig. A.7 as well as the energy and angular distribution of the second sputtering of the explantation process app.fig. A.9. Additionally the 1D and 2D distributions of the positions of ^{206}Pb-ions inside the spectrometer vessel wall app.fig. A.11.

As well as the energy, the corresponding velocity distribution is also important. The velocity can easily be calculated via:

$$v = \sqrt{\frac{2 \cdot E}{m_{\text{atom}}}} \cdot 9822.695 \frac{\text{m}}{\text{s}} \quad . \tag{3.9}$$

In this connection, the velocity factor 9822.695 arises from the units transformation

$$[v] = \sqrt{\frac{\text{eV}}{\text{u}}} = 9822.695 \frac{\text{m}}{\text{s}} \quad ,$$

since the energy is given in electronvolts and the masses of the atoms in atomic mass units u. By applying this formula to the model function, one obtains the velocity model function $\tilde{Y}(v, c, m, m_{\text{atom}})$ with changed constants:

$$\begin{aligned}
\tilde{c} &= \frac{c \cdot (1 - 3m + 2m^2) \cdot m_{\text{atom}}}{2 \cdot (9822.695)^2} \\
\tilde{k} &= \frac{m_{\text{atom}}}{2 \cdot (9822.695)^2} \\
\tilde{Y}(v) &= \tilde{c} \frac{U^{1-2m} \cdot v^2}{(U + kv)^{3-2m}} \quad . \qquad (3.10)
\end{aligned}$$

The velocity distributions can therefore be derived with the previously adjusted parameters from the energy distribution (tab. 3.5) and are shown in fig. 3.8. The corresponding peak values are calculated in tab. 3.6 and the time-of-flight curves are illustrated in fig. 3.9 for a further estimation of the necessary lifetimes of the possible metastable atoms.

Table 3.6.: Calculation of the peak velocities via eq. 3.9 with the energy peak values and the atomic masses.

Element	E_{peak} (eV)	atomic mass (u)	v_{peak} ($\frac{\text{m}}{\text{s}}$)
O	0.572	16	2626.54
Cr	1.426	52	2300.40
Fe	1.516	56	2285.61
Ni	1.595	58	2302.63
C	2.370	12	5715.52

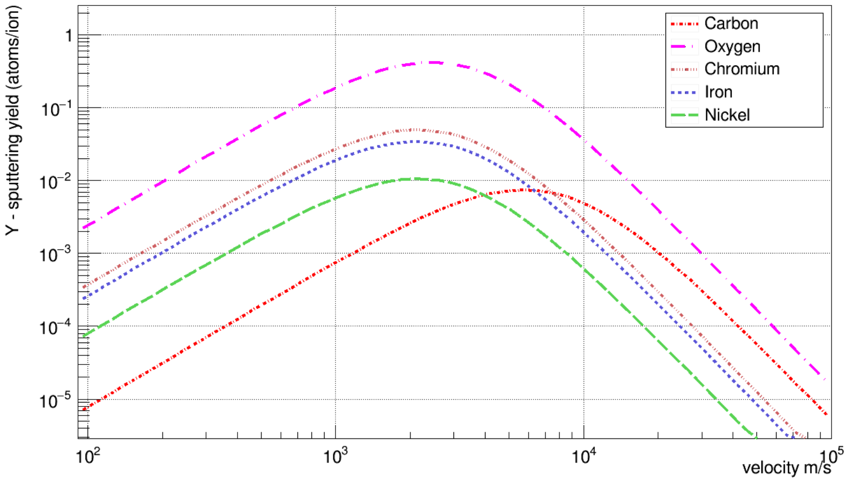

Figure 3.8.: Velocity distributions $\tilde{Y}(v)$ of the most common elements: oxygen, chromium, iron, nickel, and carbon. The curves are calculated with the velocity model function eq. 3.10 and have the same style as the energy fits.

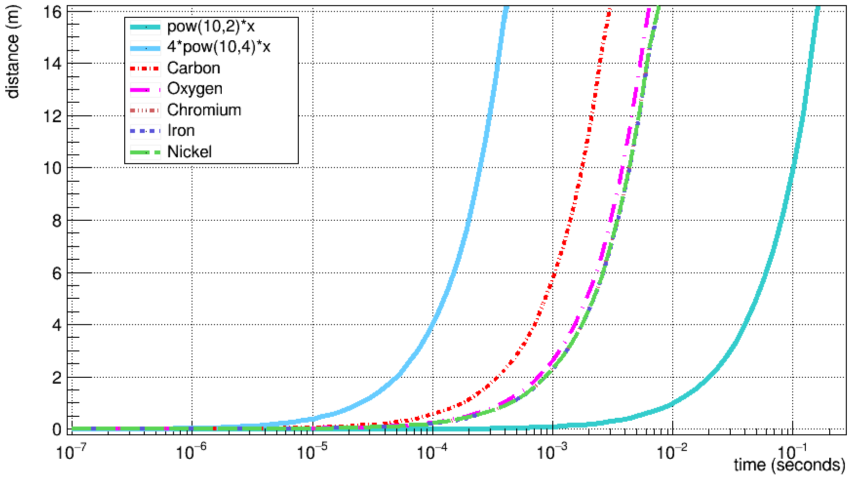

Figure 3.9.: Time-of-Flight curves of the most probable velocities (v_{peak}) of each atom. Two borders at velocities of $v_{\text{low}} = 100\,\text{m/s}$ and $v_{\text{high}} = 40000\,\text{m/s}$ are also shown.

The implantation of ^{210}Pb and the explantation of ^{206}Pb by radioactive decays into the compound of the main spectrometer stainless steel is feasible. The implantation profile of ^{210}Pb with a kinetic energy of 146 keV showed an average implantation depth of $x \approx 140\,\text{Å}$. The subsequent sputtering simulation of the ^{206}Pb-ions, initiated at the implantation positions, revealed a sputtering yield of about 63 atoms per contributing ion, taking into account a secondary process of the transmitted ions. The energy distributions showed significant maxima of values in the order of ≈ 1 eV, corresponding to velocities of the atoms in the order of 2500 m/s. The energy distributions can be well described with a model function, provided by Eckstein [77]. The acquired velocities give insights to properties metastable atoms must have in order to be the main background source. The time-of-flight illustrates a necessary lifetime of these atoms of several milliseconds. Since the background density is constant over the entire volume, the metastable atoms should live long enough, so they can overcome a flight distance of up to 10 m, the spectrometer radius. Further discussion is given in sec. 4.2.

The software SRIM is suitable for examining some characteristics of the sputtering yield. In particular, the implantation profiles are very illustrative at high precision. The energies and angles of the sputtered atoms are calculated approximately, however they correspond to the expectation from the theory and are calculated quickly. Some problems were detected, such as an unexplained energy shift around the sublimation heat. The energy distributions only started from this value, so they have to be shifted back by this heat value. Likewise, the heat of sublimation is merely an orientation value and can only approximate as the surface binding energy, if its available. This is not the case for gas atoms such as oxygen and nitrogen. Often, the calculations have not been completed to the full number of primary particles, which subsequently had to be repeated in a second pass. Problems have also arisen with the representation of numbers, e.g. with decimal points and exponential notation. In addition, it is not satisfactory that the atomic composition is only randomly distributed and molecules as well as ions or excited atoms are not considered at all. Nevertheless, the simulation provided important characteristics of the sputtering yield, which contribute to the further development the Rydberg background model.

4. Ionisation mechanisms of Rydberg atoms

4.1. Ionisation by black body radiation

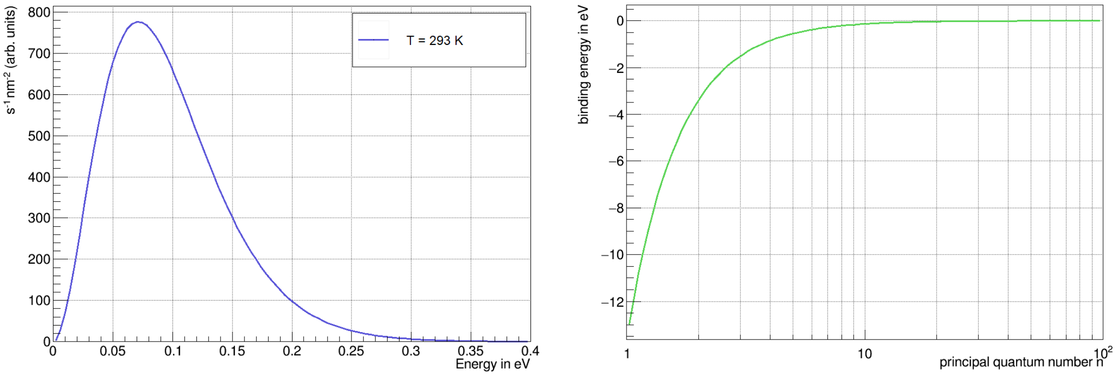

(a) **(b)**

Figure 4.1.: (**a**): Black body radiation distribution at $T = 293$ kelvin, described by Planck's law as a function of energy. (**b**): Electron binding energy of hydrogen atom as a function of the principal quantum number n of the Bohr model.

The interaction of Rydberg atoms with thermal radiation, i.e. black body radiation (BBR) is of special interest. The energy spacing between neighbouring states of high principal quantum numbers (n_+, n_-) can be calculated with the Rydberg formula:

$$\Delta E = E(n_+) - E(n_-) = -Ry\left(\frac{1}{n_+^2} - \frac{1}{n_-^2}\right) \quad , \tag{4.1}$$

with $n_+ > n_-$ and $Ry = 13.606\ldots$ eV. The maximum of the black body radiation distribution is ≈ 0.07 eV (see fig. 4.1a). The energy spacing $\Delta E \leq 0.1$ eV corresponds to the tuple $(n_+, n_-) = (7, 6)$, therefore Rydberg atoms are strongly affected by black body radiation, even at room temperature [71]. In addition the coupling to thermal radiation is large due to large dipole matrix elements of transitions between Rydberg states. Hence, an excited state switches to other energetically nearby states by BBR-induced dipole transitions. The effective lifetime of one state is described by the sum of inverse decay rates. These rates are the spontaneous decay rate Γ_{nl} by radiative transitions and the BBR-induced decay rate Γ_{BBR}. Since the black body decay rate scales with n^{-2}, while the spontaneous one scales with n^{-3}, it is evident that the black body radiation rate exceeds the spontaneous emission rate at high enough n, even for low l, altough Γ_{nl} decreases rapidly with increasing l [71]. The rate of BBR-induced transitions can be ten times larger than the rate of spontaneous transitions to neighbouring Rydberg states [127] in the case of a $n = 18, l = 17$ hydrogen-like state.

$$A^* + \hbar\omega_{\mathrm{BBR}} \longrightarrow A^+ + \mathrm{e}^- \quad . \tag{4.2}$$

In addition to radiative nl transitions, black body radiation can also photo-ionise highly excited Rydberg atoms and generate very low energy electrons. The energy distribution can be seen in fig. 4.2 and holds the condition

$$E_{\mathrm{BBR,e^-}} = \hbar\omega_{\mathrm{BBR}} - \frac{Ry}{n^2} \quad , \tag{4.3}$$

whereby the photon energy $\hbar\omega_{\mathrm{BBR}}$ must exceed the ionisation threshold of the excited atom. Electrons from Rydberg photo-ionisation at room temperature thus have low energy since the energy of the photons rarely exceed 0.25 eV. The kinetic energy is below 0.15 eV and therefore lower than the energy resolution of the KATRIN main spectrometer, so they cannot be magnetically stored. The bound-free matrix elements of this process are complicated and difficult to compute since the basis of the bond states contains no free states and no orthogonality is given [128]. For calculation up to high n, one set of equations exists, providing the computation. With these the ionisation cross-section, dependent on the bound-free matrix elements $\mathcal{R}_{nl}$ reads

$$\sigma_{nl}^{\mathrm{ion}}(\omega_{\mathrm{BBR}}) = \frac{4\pi^2\alpha\omega_{\mathrm{BBR}}}{3(2l+1)}[l\mathcal{R}^2_{nl\to E,l-1} + (l+1)\mathcal{R}^2_{nl\to E,l+1}] \quad . \tag{4.4}$$

The ionisation cross-section in conjunction with the black body radiation spectrum (fig. 4.1a) lead to the electrons energy spectrum [128].

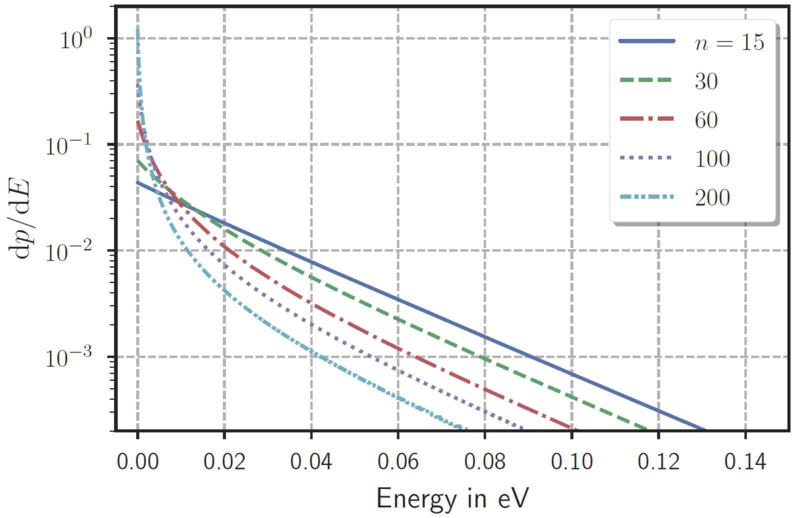

Figure 4.2.: Electron energy spectrum emitted from BBR photoionisation for different n and constant $l = 1$ at 293 kelvin [128].

4.2. Penning ionisation

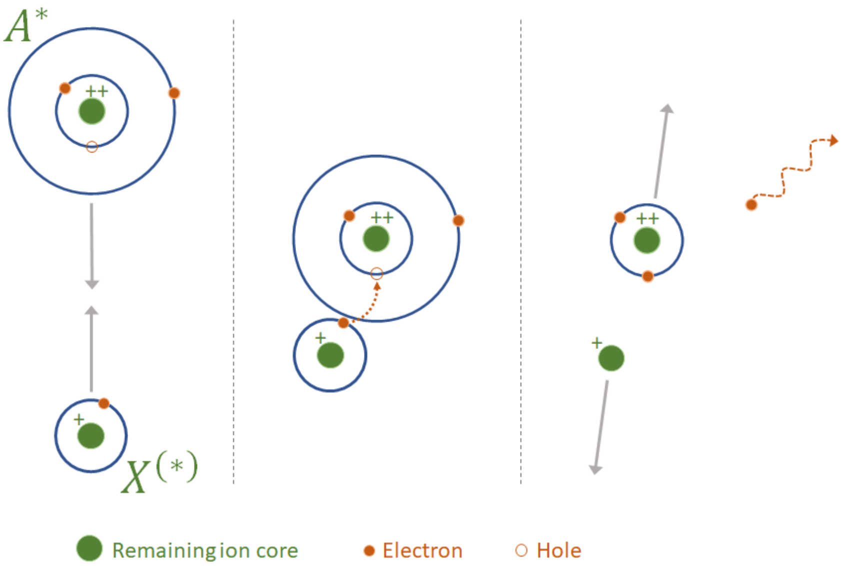

Figure 4.3.: Process of Penning ionisation. Ionisation of an (excited) atom $X^{(*)}$ by collision with an excited atom A^{*} under electron emission. Adapted from [129].

Penning ionisation describes low energy collisional ionisation under electron emission, discovered and first described by Penning [130]. As shown in figure 4.3, two atoms collide, at least one which is excited. In this case atom A^{*} is the excited one and $X^{(*)}$ the collisional partner, which may be excited. Due to the excitation of A^{*}, an electron-hole is present into which an electron of $X^{(*)}$ can be transferred. As an example from [129], metastable helium $\mathrm{He}(2^3\mathrm{S})$ and ground state hydrogen $\mathrm{H}(1^2\mathrm{S})$ approach each other. Attraction due to van der Waals force leads to overlapping of their electron clouds by forming a excited quasi-molecule. A strong probability that the electron from ground state hydrogen jumps into the lower orbit of helium is present, if the spin state is appropriate, followed by emission of the excited electron. By considering energy conservation and neglecting kinetic energy, the excited electron gains the energy difference

$$\Delta E = E_{\mathrm{e}^-} = E_{\mathrm{exc}}(A^{*}) - E_{\mathrm{ion}}(X^{+}) \tag{4.5}$$

of the initial and final state, whereby subscript ‘exc’ means excitation and ‘ion’ ionisation.

In general more final states are possible, either the formation of a ground state atom with an ion, or the formation of a molecular ion, accompanied by an electron. The reactant $X^{(*)}$ can also be a molecule which gets ionised, dissociated and ionised, or dissociated under formation of a negative/positive ion pair [129, 131–136].

$$A^* + X \longrightarrow A + X^+ + \mathrm{e}^- \qquad \text{Penning ionisation (atomic)} \tag{4.6}$$

$$A^* + X \longrightarrow AX^+ + \mathrm{e}^- \qquad \text{Associative ionisation} \tag{4.7}$$

$$A^* + X_2 \longrightarrow A + X_2^+ + \mathrm{e}^- \qquad \text{Penning ionisation (molecular)} \tag{4.8}$$

$$A^* + X_2 \longrightarrow A + X^+ + X + \mathrm{e}^- \qquad \text{Dissociative ionisation} \tag{4.9}$$

$$A^* + X_2 \longrightarrow A + X^+ + X^- \qquad \text{Negative/positive ion formation} \tag{4.10}$$

These reactions are collectively called chemi-ionisation reactions in order to restrict Penning ionisation only to reaction 4.6 and 4.8. The electron energy is dependent on both the initial kinetic energies and the potentials of the final states, which can be described by Lennard-Jones potentials. This may lead to kinetic energies of emitted electrons up to few electronvolts [129, 132].

For the case of interacting excited or Rydberg atoms, the quantum mechanical state of the atoms has to be considered. The interaction potentials are mainly lead by dipole-dipole interactions due to their large dipole momenta, when the electron is ‘far’ away from the ionic core [137–139]. These interactions are of greater interest because of their application in quantum information and quantum simulation science as well as quantum mechanical description of ultra-cold systems [139–146]. Figure 4.4 illustrates the resonant coupling of an atomic pair of excited atoms. Through dipole interaction, the pair undergoes an Auger-type process including ionisation and electron emission without the necessity of overlapping electron clouds. The energy level diagram on the left side shows the de-exciting atom (subscript ‘d’), the one on the right, the ionising atom (subscript ‘i’). The transition energy from (n_d, l_d) to (n'_d, l'_d) can be calculated via the Rydberg formula eq. 4.1 and has to be larger than the ionisation energy ε_0 of the ionising atom, determined with eq. 2.5, to ionise the atom. Considering ε_0 as a theoretical transition of the de-exciting atom, one obtains the final electrons energy vie eq. 4.1

$$\varepsilon'_i = -Ry\left(\frac{1}{n_{th}} - \frac{1}{n'_d}\right) \quad . \tag{4.11}$$

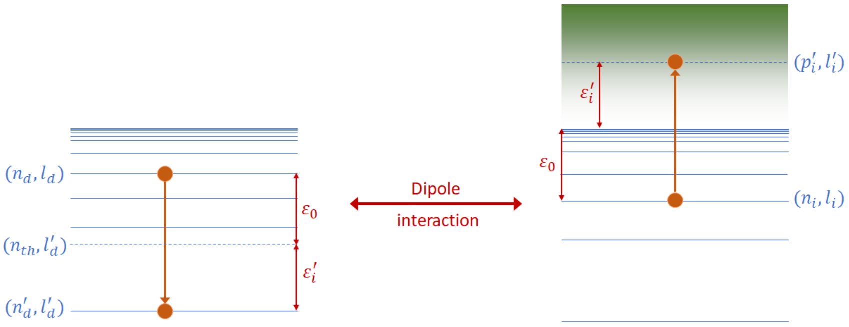

Figure 4.4.: Illustration of energy levels at the dipole-dipole interaction mechanism of two excited atoms. Resonant coupling of an atomic pair to the continuum via an Auger-type process. Adapted from [144].

To investigate the impact of Penning ionisation as a solution of the remaining background, simulations with Kassiopeia were performed. As a starting point, using an activity of $\approx 1\,\mathrm{kBq}$, one thousand decays of ^{210}Pb in the main spectrometer vessel wall during one second, followed by the formation of Rydberg atoms. were simulated. These particles maintain a uniformly distributed energy between 8 eV and 30 eV and are emitted under various polar angles defined by a Gaussian with a mean of 16° and sigma of 28°. The polar angle is uniformly distributed between -180° and $+180^\circ$. At each decay, 24 particles start at diced positions from the inner surface. In conclusion during one second 24000 particles start from the inner surface with various energies under various angles to verify possible interactions within the spectrometer volume. However, this simulation provided no indication of background arising from colliding Rydberg atoms, since the closest approach was only 45 cm. In addition this simulation yields to the path length of each atom, which is shown in fig. 4.5a. It nicely demonstrates why the mean lifetime of excited atoms should be in the order of milliseconds, as most fly the length of the spectrometer diameter.

In contrast, Penning ionisation is always present near the surface. Figure 4.5b shows the lateral distribution of starting positions of sputtered atoms from the surface of one single decay event, evaluated with SRIM. This example, 60 atoms got sputtered, spread over an area of $\approx 70\,\mathrm{nm}^2$. The size of excited atoms scales with n^4, so that this area would correspond to the size of an excited hydrogen atom with $n = 9.72$. If only 10% of these sputtered atoms are excited, one can assume that each electron cloud intersects with another. This overlap would efficiently cause the ionisation of some atoms near the surface. The necessity of excited atoms inside the spectrometer volume therefore leads to the conjectures that either only a very small fraction of excited atoms are generated which do not interact with other sputtered atoms or Penning ionised atoms capture electrons in a high state and re-ionise within the volume.

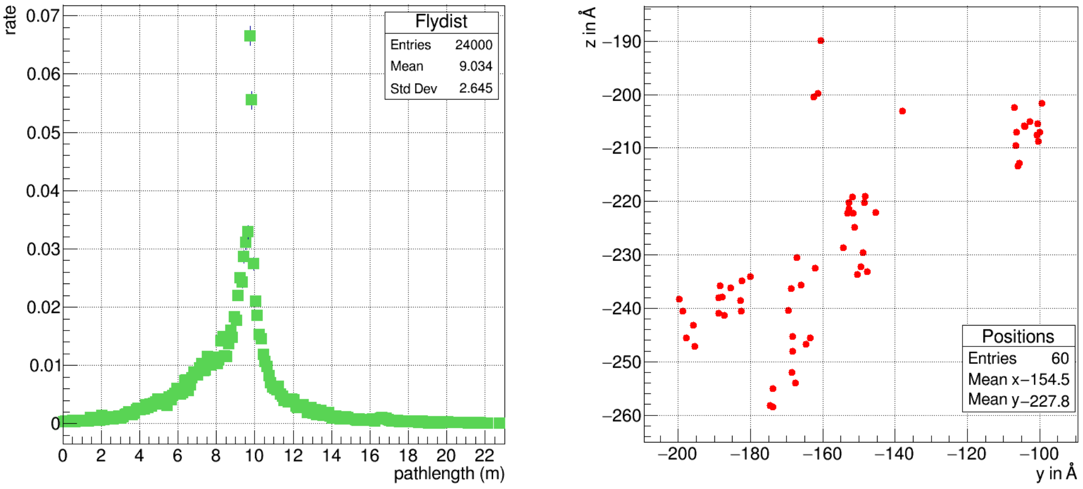

(a) **(b)**

Figure 4.5.: (**a**): Path length distribution of particles started from the inner surface under various angles as described in the text. (**b**): From SRIM simulation, the starting positions of sputtered atoms from one decay event.

4.3. Field ionisation

4.3.1. Behaviour of Rydberg atoms in fields

Rydberg atoms are strongly affected by external fields because the electron binding energies are low and the dipole moment high, thereby external fields may reach similar strengths as the nuclear Coulomb field. In order to compare fields with the atomic energy levels, atomic units are introduced. As a starting point, the influence of external electric or magnetic field becomes comparable with the Coulomb field when they reach the atomic units

$$F_0 = \frac{e}{4\pi\epsilon_0 a_0^2} = 5.142 \cdot 10^{11}\,\frac{\mathrm{V}}{\mathrm{m}} \ , \tag{4.12}$$

$$B_0 = \frac{\hbar}{e a_0^2} = 2.351 \cdot 10^{5}\,\mathrm{T} \ , \tag{4.13}$$

for an electron in the hydrogen ground state. These field strengths are far beyond experimental reach, but accesible for high excited states, since the necessary strengths scale with the principal quantum number n [71, 74]. This will be shown in the cases of electric and magnetic fields, separately. During this chapter, atomic units are used, whose transformation is shown in app. tab. A.5.

Atoms in electric fields

An external electric field $\vec{F}$ introduces the perturbing potential

$$\begin{aligned} V_S &= -\vec{d} \cdot \vec{F} \ , \\ \text{where } \vec{d} &= \sum_i q_i \vec{r}_i \end{aligned} \tag{4.14}$$

is the dipole moment of the atom and i runs over all electrons in the atom. This perturbation is called the Stark effect, which couples l and $l \pm 1$ states of the same m by electric dipole matrix elements. Since l is no longer a good quantum number, it is common to work in parabolic coordinates

$$\begin{aligned} \chi &= r + z \\ \eta &= r - z \\ \varphi &= \tan^{-1}\left(\frac{y}{x}\right) \ , \end{aligned} \tag{4.15}$$

where the Schrödinger equation becomes separable and solvable. This transformation leads to a new set of quantum numbers in relation to n and m

$$\begin{aligned} n &= n_1 + n_2 + |m| + 1 \\ k &= n_2 - n_1 \ . \end{aligned} \tag{4.16}$$

For fixed n and m, there are $n-|m|$ possible values of k ranging from $-n-|m|+1$ to $n-|m|-1$, so the tuple (n, k, m) specifies the Stark eigenstates [146]. The electric field perturbs the

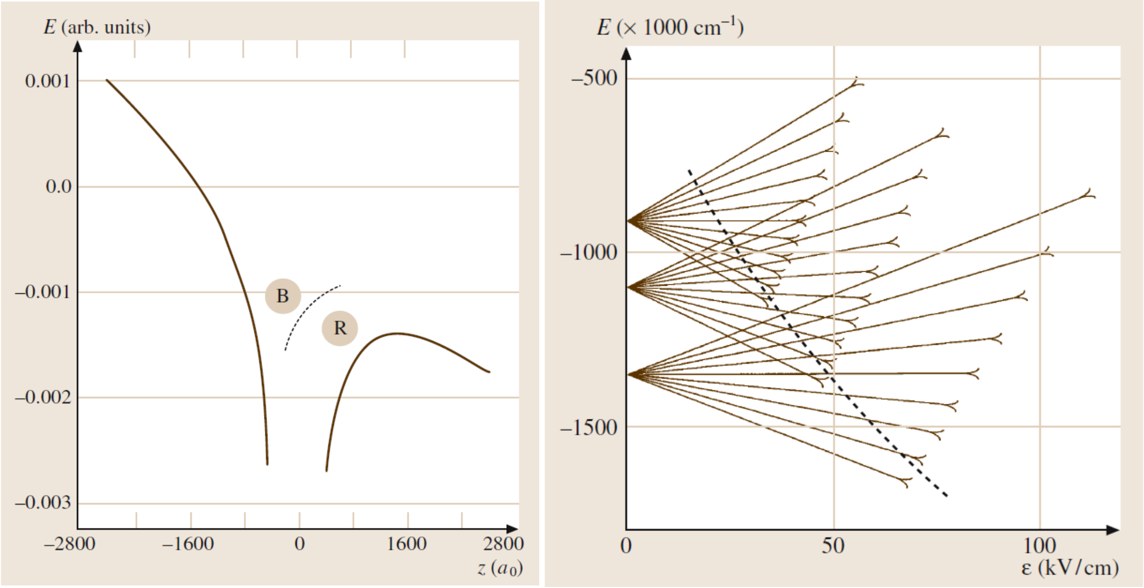

(a) (b)

Figure 4.6.: (**a**): Combined Coulomb-Stark potential along the z-axis when a field of $5 \cdot 10^{-7}$ a.u. (2700 V/cm) is applied. The red state (R) is near the saddlepoint, and the blue state (B) is held on the upfield side of the atom by an effective potential (dashed) [74]. (**b**): Energies of hydrogen $m = 0$, $n = 9, 10, 11$ levels as a function of electric field strength ε. The dashed line indicates the classical ionisation limit $F = E^2/4$ and their onset of the broadening is at an ionisation rate of $10^6\ s^{-1}$ [74].

hydrogen atom and shifts its energy levels, which can be analytically expressed by

$$\begin{aligned} E &= E^{(0)} + E^{(1)} + E^{(2)} + \dots \\ &= -\frac{1}{2n^2} + \frac{3}{2}knF - \frac{1}{16}[17n^2 - 9m^2 + 19 - 3k^2]n^4F^2 + \dots \end{aligned} \tag{4.17}$$

The correction $E^{(1)}$ is called the linear Stark effect and $E^{(2)}$ the quadratic Stark effect, which is the lowest order contribution for ground state atoms since $n = 1$ leads to $m = k = 0$.

Considering an electric field F applied parallel to the z-axis, the total potential for a hydrogen atom in atomic units reads

$$V = -\frac{1}{r} + Fz \ . \tag{4.18}$$

It has a saddle point at $z = -1/\sqrt{F}$, where the potential is $V = -2\sqrt{F}$. This effect is shown in fig. 4.6a with the presence of so called red and blue Stark states. These states are characterised by the maximum values of k under the assumption of $m = 0$. The linear energy shifts are thus maximal whereby either $n_1 - n_2 = n - 1$ shifts the energy up (blue state) or $n_2 - n_1 = n - 1$ shifts it down (red state). Figure 4.6b shows the level crossing of a hydrogen atom with $m = 0$ and principal quantum numbers $n = 9, 10, 11$. The linear Stark effect causes the energy splitting described by k and the crossing of different n levels, if the applied field is sufficiently high. In general the Stark effect of other atoms is not identical to that observed in H, states of nonzero quantum defects join the Stark manifold at some nonzero field and the levels of blue and red states avoid crossing, which can be seen in app. fig. A.12 in the case of Na.

Classically, ionisation occurs if the energy E lies above the saddle point in the potential eq 4.18, which requires the field

$$F = \frac{E^2}{4} = \frac{1}{16n^4} \quad . \tag{4.19}$$

The red and blue states ionise at very different field strenghts since their energy can be very different. The energy of extreme red states is significantly lower, therefore, these states ionise at lower electric fields. Quantum mechanically tunneling through the potential barrier also has to be taken into account, which slightly lowers the ionisation limit as well. Due to finite size of ionic cores of other elements than hydrogen, level crossing between red and blue states of different n is avoided. However, classical ionisation also occurs above the ionisation limit eq. 4.19, in which the same coupling between hydrogenically stable blue states and degenerate red states continua leads to the autoionization of the blue states [147]. As a consequence, all states above the classical ionisation limit ionise at experimentally significant rates, while for higher m states, where the core coupling is smaller, the behaviour is more similar to hydrogen [74].

In addition to static electric fields, varying fields which cause ionisation also has to be considered. This phenomenon is often investigated and theoretically described, e.g. the ionisation of excited atoms by short pulsed laser fields - Stark kick ionisation [71, 147–157].

Atoms in magnetic fields

The influence of magnetic fields is called Zeeman effect [158] and describes the interaction of atoms with an external magnetic field $\vec{B}$, its potential reads

$$V_Z = -\vec{\mu} \cdot \vec{B} = \frac{\mu_B}{\hbar}(g_l \vec{L} + g_s \vec{S}) \cdot \vec{B} + \frac{e^2}{8mc^2}(\vec{B} \times \vec{r})^2 \quad . \tag{4.20}$$

Here, $\vec{\mu}$ is the magnetic moment, μ_B the Bohr magneton, and g_i the orbital g factors $g_l = 1, g_s \approx 2$. In general, three cases of Zeeman effect are present depending on the magnetic field strength. The relative strength of the magnetic field affects spin-orbit coupling. If the magnetic field is weak the anomalous Zeeman effect acts as perturbation in which the angular moment $\vec{L}$ and the spin $\vec{S}$ are coupled to the total angular momentum $\vec{J} = \vec{L} + \vec{S}$. At sufficient high field strengths the angular momentum and the spin are decoupled which is called the Paschen-Back effect. $\vec{L}$ and $\vec{S}$ independently precess around the magnetic field axis [74, 146]. For moderately strong fields up to $B \sim 10^4$ T, the quadratic term in eq. 4.20 can be neglected.

Since the magnetic fields at KATRIN are not in the high field strength regime, only the anomalous Zeeman effect at weak fields is considered. At LS-coupling the energy splitting for given values of l, s, j by the perturbation of a magnetic field along the z-axis is given by

$$\Delta E_{m_j} = g\mu_B B m_j \tag{4.21}$$

$$\text{with } g = g_l \frac{j(j+1) - s(s+1) + l(l+1)}{2j(j+1)} \tag{4.22}$$

$$+ g_e \frac{j(j+1) + s(s+1) - l(l+1)}{2j(j+1)} \tag{4.23}$$

the Landé splitting factor, while $g_e = 2$ and $g_l = 1$ are sufficient as a first approximation [74].

For Rydberg atoms there is slighty different reasoning. The ratio of the diamagnetic term to the linear magnetic field term is $\sim n^4 B$, since the expectation value of $(\vec{B}/|B| \times \vec{r}) \propto n^4$, according the size of the atom [71]. If $n^4 B << 1$, the quadratic diamagnetic term can easily be neglected, the magnetic effects are of the same size as they are in low lying excited states of the same l with a small difference. For $n^4 B \leq 1$ the quadratic term cannot be ignored anymore, but $\vec{L}$ and $\vec{S}$ are decoupled, whereby $\vec{S}$ can often be neglected. The resulting interaction only depends on $\vec{L}$ and B, and has rotational symmetry about the axis parallel to $\vec{B}$ [71]. In this case the linear energy splitting changes due to the non-negligible quadratic term and is approximated by

$$\Delta E_{m_j} = \frac{m_j B}{2} + \frac{B^2}{8}(1 + m_j^2) n^4 \ . \tag{4.24}$$

Each level splits in $(2J + 1)$ equidistant Zeeman-levels, corresponding to the separation of each m_j with $\Delta m_j = \pm 1$. The $m = \pm 1$ states are split by the linear shift and have twice the diamagnetic shift of the $m = 0$ state [71]. At a field strength of 1 T, the corresponding principal quantum number is $n \approx 22$, where the contribution of the quadratic term is equal to the linear one.

Static magnetic fields themselves do not lead to the ionisation of atoms, since their effect is small compared to electric fields. The perturbation affects the angular and spin moments and does not lead to level crossing of different principal quantum numbers n, as electric fields. However, magnetic fields can indirectly cause the ionisation of atoms, if atoms move through a static magnetic field. Due to the Lorentz transformation of the motion, referring to a system, where the atom is at rest, an electric field is induced by the seemingly moving magnetic field. The connection between the induced electric field $\mathcal{E}_0$ and the static magnetic field $\mathcal{H}$ reads

$$\frac{\mathcal{E}_0}{\mathcal{H}} = \sqrt{\gamma^2 - 1} \cdot \sin(\varphi) \ , \tag{4.25}$$

whit $\gamma = \sqrt{1 - v^2/c^2}^{\,-1}$ the Lorentz factor, v is the velocity of the atom, and φ is the angle between $\vec{v}$ and $\vec{\mathcal{H}}$ [159–161]. Since this equation contains the Lorentz factor it is clear that only very strong magnetic fields with intermediate velocities or weaker fields with relativistic velocities can cause induced electric field of sufficient strengths.

As a consequence the behaviour of atoms and Rydberg atoms in crossed or parallel electric and magnetic fields was often theoretically described [152, 153, 162–166]. The theories involve averaged dynamics of perturbed Kepler orbits or the tool imaginary time method, providing the description of tunneling and ionisation by using classical equations of motion. All these treat the chaotic motions of atoms, whose description would exceed the scope of this work. One effort which should be mentioned, Fauth et. al [162] observed an outer potential minimum of rubidium Rydberg atoms in crossed electric and magnetic fields. This state corresponds to a bound state with a very high dipole moment, which can be reached e.g. via tunneling from a highly excited state. Their measurements were performed at low fields in the order of $[F] \sim 1\,\mathrm{kV/m}$ and $[B] \sim 0.1\,\mathrm{T}$. The existence of this state was surprising and only possible via special field configurations, leading to an outer minimum of the electrons potential, and a highly excited long-living state.

4.3.2. Electric and magnetic fields in the KATRIN main spectrometer

The magnetic field setting in the KATRIN main spectrometer is mainly adjusted by the pre-spectrometer magnet (PS2) and the pinch magnet (PCH), at the entrance and exit of the main spectrometer. Additionally it can be varied by the LFCS, the low field correction system, to compensate the earth magnetic field and fine-tune the analysing plane. The nominal magnetic field at the solenoids is of the order of few tesla, while it drops to tenth of milliteslas at the analysing plane. With the above mentioned process of Lorentz ionisation, the induced electric field for atoms with $v = 10^4\,\mathrm{m/s}$ at a magnetic field of 5 T is

$$\begin{aligned}\mathcal{E}_0 &= \sqrt{\gamma^2 - 1} \cdot 5\,\mathrm{T} \\ &= 1.\bar{1} \cdot 10^4 \cdot 2.13 \cdot 10^{-5}\,\mathrm{a.u.} \\ &= 9.455 \cdot 10^{-16}\,\mathrm{a.u.} = 0.486 \frac{\mathrm{mV}}{\mathrm{m}} \quad . \end{aligned} \tag{4.26}$$

This vanishing field strength would not cause any meaningful perturbation of the atoms, thus this effect can be neglected.

Indeed, we intentionally generate electric fields inside the main spectrometer. On the one hand by the high voltage on the vessel, and on the other hand by the inner electrode system. The general voltage setting on the main spectrometer vessel and the inner electrode system (IE) is

$$\begin{aligned} V_{\mathrm{vessel}} &= -18400\,\mathrm{V} \quad , \\ V_{\mathrm{IE}} &= -200\,\mathrm{V} + V_{\mathrm{vessel}} \quad . \end{aligned}$$

The inner electrode system consists of two layers of wires in distances of 0.15 m and 0.22 m. Figure 4.7 shows the x-component of the electric field strength simulated with KEMField [167] between the vessel wall ($x = 4.9\,\mathrm{m}$ at $z = 0\,\mathrm{m}$) and the inner electrode system at the radial edge ($x < 4.9\,\mathrm{m}$) on a plane at the center ($z = 0\,\mathrm{m}$). The electric field strength ranges from -6000 V/m to 4000 V/m, with these peak values only prevailing directly on the wires. The significant areas around $\pm 0.075\,\mathrm{m}$ belong to the wire suspension, which are also on V_{IE}. To investigate possible field ionisation scenarios, one should take a closer look into the electric field between the vessel and the inner electrode. For this purpose, the simulated field map was used to get the field strength along specific paths started at

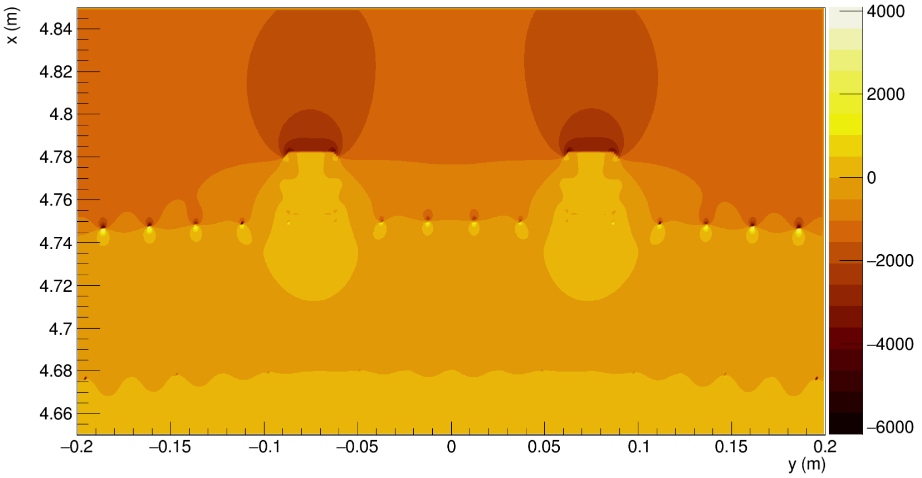

Figure 4.7.: Electric field contour map at the vessel wall in the xy-plane. At global KATRIN main spectrometer coordinates $-0.2\,\mathrm{m} \leq y \leq 0.2\,\mathrm{m}$ and $4.65\,\mathrm{m} \leq x \leq 4.85\,\mathrm{m}$. The color indicates the electric field strength $\vec{E}_x$ in V/m.

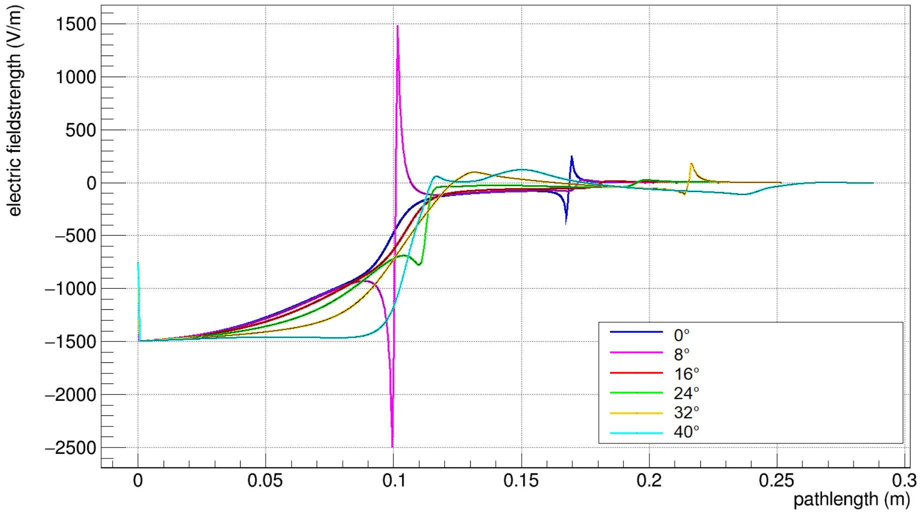

Figure 4.8.: Electric field strength $\vec{E}_x$ distributions along straight paths started from $(x, y, z) = (4.85, 0, 0)$ directed into the volume under various polar angles ($0° \leq \theta \leq 40°$).

$x = 4.85$m under certain polar angles. Such field strength along straight paths are shown in figure 4.8. The blue curve, corresponding to 0° does not show a peak around 0.1 m, since this path is exactly between two wires of the first wire layer, however, a peak appears at 0.17 m, corresponding to the second wire layer at $x = 4.68$ m. The pink curve with a polar angle of $\theta = 8°$ nicely shows the first wire layer peak with an absolute maximum of 2500V/m and also the negative field strength between the two wire layers. Free electrons of low energy generated between the wire layers will therefore also be accelerated back to the vessel surface. These pathway studies showed that free electrons are efficiently kept away from the volume between the surface and the inner electrode, because the mean electric field is pointing towards the surface. The field strength is slightly negative even behind the second wire layer. More such electric field distributions along paths for the different electric field directions along x, y, and z under various polar angles can be found in app. A.3.1.

For concluding this chapter, it should be mentioned that the magnetic field in the KATRIN main spectrometer does not perceptibly perturb Rydberg atoms. In contrast to the magnetic fields, the electric fields contribute to the perturbation of Rydberg atoms. Due to the high peak strengths at the inner electrode wire system, Rydberg atoms might be ionised by these electric fields. Since the atoms are in motion, the wire electrode electric field appears as a pulsed field, which causes the ionisation, according to [149–151, 157]. Hereby resulting electrons will be efficiently withdrawn by the electric field and can not cause background events. However, Rydberg atoms are subject to the Stark effect through the electric field, which affects their quantum mechanical state. Additionally the behaviour of excited atoms in crossed electric and magnetic fields is exceptionally interesting since their theoretical description is extremely not trivial. Nevertheless, the impact of magnetic and electric fields on Rydberg atoms does not deliver the desirable solution of the remaining background, since ionised atoms at the wire electrode can not contribute electrons within the entire volume.

4.4. Autoionization

Since the pressure inside the KATRIN main spectrometer is on a level of 10^{-11} mbar, scattering of excited atoms with gas atoms is highly improbable. Hence, intrinsic ionisation mechanisms, which takes place in the absence of other atoms must be considered. Such ionisation mechanisms are called autoionization. Discrete states, lying above the Rydberg limit, depict the convergence limit of excited state to the continuum. Thereby the wave function will be a mixture of discrete and continuum wave functions, leading to the radiationless process

$$A^* \longrightarrow A^+ + e^- \ . \tag{4.27}$$

A describes either single atoms or molecules. Autoionizing states lead to resonance lines in absorption spectroscopy and were firstly observed by P. Auger as the Auger effect.[168]

4.4.1. Interatomic coulombic decay

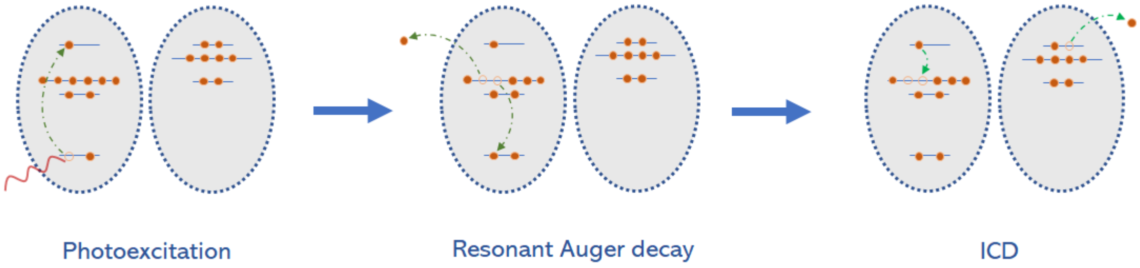

Figure 4.9.: Energy level scheme of two neighbouring atoms for ICD electron generation after resonant Auger decay. Adapted from [169].

Electron correlation is responsible for many effects in atomic and molecular physics. The most basic process involving more than one electron is the single photon double ionisation of He atoms. In contrast, many electronic processes can not be described intuitively such as interatomic electron scattering. These processes form a genre of ‘non-local electronic effects’, which means that participating electrons are not connected via chemical bounds. Penning ionisation or the resonance electron transfer are non-local processes since the participating atoms do not share electrons. The interatomic (or intermolecular) coulombic decay (ICD) phenomenon is similar to those mentioned, however, the electron correlation arises from local effects. It was initially predicted to be present in HF and water molecules and was first observed in Neon dimers (Ne_2).[169, 170]

The ICD in the case of neon occurs by the 2s-ionisation of one atom of the dimer, while a 2p-electron fills this vacancy. The de-excitation energy is transferred to the atomic neighbour, leading to a 2p-ionisation of the second atom. This process can be theoretically treated as an Auger decay, it differs only since the electrons are located at two different atoms. Thus, the total decay rate depends on the electron-electron Coulomb matrix elements by a direct and an exchange contribution. After the experimental verification of the existence of ICD, many different mechanisms were observed. ICD occurs not only after inner-valence ionisation/excitation, but also after resonant excitation as high lying states decay, and subsequent to Auger cascades after inner shell ionisation. The list of ICD-like processes evolved steadily, since ICD electrons were also observed after electron capture or in solutions. In addition theoretical progress favours the search for further mechanisms such as two-center resonant photoionisation. It turned out that the presence of neighbouring atoms increases the photoionisation probability of one atom by orders of magnitude, if a resonant excitation of the other atom and subsequent ICD is energetically possible. Another process called electron transfer mediated decay (ETMD) differs from ICD in the way, that the initally excited atom is neutral after ETMD and the electron donor atom is doubly charged. In this case, the atomic system principally consits of different species with strongly differing energetics. The double ionisation potential of one atom can lie below the inner-valence threshold of the other, leading to the vacancy being filled by an electron of the neighbouring atom.[169]

Figure 4.9 illustrates the three step process of resonant Auger decay ICD. After the initial excitation of a ground state electron, a resonant Auger decay follows. An electron from a higher lying shell, radiatively decays into the vacancy under photon emission. This photon gets absorbed by another electron of the original shell and gets transmitted into the continuum with very low energy. Now the primary excited electron decays into the remaining vacancy, while the emitted photon gets absorbed by an electron of the neighbouring atom, leading to an ICD electron with energies in the eV range. This process results in the formation of two positive ions, which repel eachother due to the Coulomb force.[169]

In order to further describe the ICD mechanism, excitations other than those by photons must be considered. ICD was also carried out after ion and electron impact, in which the dimers got excited or ionised. For example, the breakup reaction of He_2 into He^+/He^+ by alpha bombardment was observed [171]:

$$\begin{aligned} \mathrm{He}-\mathrm{He}+\mathrm{He}^{2+} &\rightarrow \mathrm{He}^{+*}(n=2\ldots4)\text{–}\mathrm{He}+\mathrm{He}^{+} \\ \mathrm{He}^{+*}\text{–}\mathrm{He} &\rightarrow \mathrm{He}^{+}+\mathrm{He}^{+}+\mathrm{e}^{-}_{\mathrm{ICD}} \quad . \end{aligned} \tag{4.28}$$

Such processes yield to ICD electron energies up to 10 eV, which is the reason, why the interatomic/-molecular coulombic decay is to taken into account as a a background source in the KATRIN main spectrometer. The dipole measurements (fig.2.20) revealed background electron energies up to 4 eV of unknown origin. It is obvious that sputtered atoms occur in clusters of several atoms that are not chemically bonded, but in very close proximity to each other. The sputtering of molecules can also be present, which can play the role of the electron mediator. It is not erroneous that clusters of sputtered atoms or molecules can be excited in such a way that ICD takes place.

However, these states typically prioritise dissociation, which yields to a time span of only several femtoseconds, in which ICD must take place [169, 172, 173]. As a consequence, the several mechanisms of ICD and ICD-like processes can not contribute as the unknown remaining background source in the KATRIN main spectrometer, because the necessary excitation within the volume is highly unlikely, although they would deliver the desired electron energies.

4.4.2. Autoionization of metastable and atomic states

Further interest has to be brought to atomic or molecular states which are able to autoionize without the presence of neighbouring atoms. The necessary energy to ionise the species itself is provided by internally stored energy. For molecular species, this internal energy can be delivered via vibrational or rotational states. The operating condition is based on energy conservation, the internal energy must exceed the ionisation limit, so that transitions to the molecular ion and an electron can take place. In general, the molecules are in an excited state in such a way the outer electron has Rydberg character with additional vibrational or rotational excitation. The ionisation process is ensued by vibrational-electronic or rotational-electronic interaction, so resulting excess energy relaxes into electronic energy and removing the Rydberg electron [168, 174, 175]. On the other hand, these vibrational or rotational excitations are not available for atomic species. Therefore, these states must achieve an energy balance in a different way that exceeds the ionisation limit. This is initially unusual at first since atomic states with energies above the ionisation limit generally get ionised.

However, in order to obtain the required lifetimes of the ionising states, an increasing search was made for so-called metastable states. Metastability of quantum mechanical states is characterised by a specific state, whose spontaneous transitions are forbidden by electric dipole transition selection rules. Therefore, their lifetime is enhanced but not infinite since electric quadrupole transitions may occur as second order effects. Helium and oxygen provide such metastable states [73] which exceed the typical lifetimes by few orders of magnitude, resulting in lifetimes of milliseconds untill seconds. Since oxygen is one of the main contributions at the sputtering processes in the KATRIN main spectrometer, the literature search was restricted to this element at first. In addition it is unclear, whether molecules are actually sputtered in sufficient numbers, so only atomic species are considered.

It turned out that oxygen definitely provides metastable with increased lifetimes, such $^1\mathrm{S}_0$ or $^1\mathrm{D}_2$ with lifetimes in the range of seconds [176]. Or a more short living one, $2p^3 3s^5\mathrm{S}$ with 185 µs. Sadly, these longer lifetimes correspond to radiative transitions and not to autoionization at all. In addition they are not able to autoionize since their excitation energy is far below ionisation limit.

Nevertheless the autoionization of excited oxygen is still an interesting effect, and it will be discussed in the following [177, 178]. Rudd and Smith in 1967 [179] experimentally investigated the energy spectra of autoionizing electrons in oxygen. Their data were obtained by bombarding oxygen gas with 100 keV H^+ and He^+ ions. They discovered six different autoionizing series of ejected electrons with energies between 0 and 4 eV, corresponding to excited states above the ionisation limit, decayinig into the $^4\mathrm{S}$ and $^2\mathrm{D}$ continua. Later, more electron spectra were recorded for example by molecular photodissociation under production of an autoionizing fragment [180]:

$$\hbar\omega + \mathrm{O}_2 \rightarrow \mathrm{O} + \mathrm{O}^* \rightarrow \mathrm{O} + \mathrm{O}^+ + \mathrm{e}^- \quad . \tag{4.29}$$

In the same manner, autoionizing Rydberg states were observed, which are forbidden to autoionize on the basis of LS coupling [181, 183]. These resonances lie above the ionisation potential of atomic oxygen, so these states subsequently de-excite by photon emission

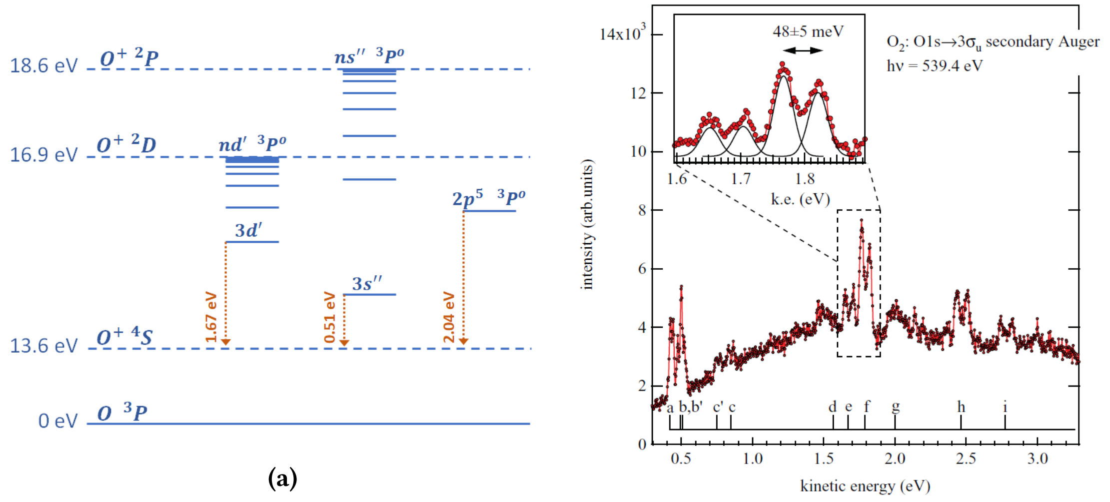

(a)

(b)

Figure 4.10.: (**a**): Term energy diagram of atomic oxygen, illustrating the Rydberg levels $nd'\ ^3\mathrm{P}^0$, $ns''\ ^3\mathrm{P}^0$ and $2s2p^5\ ^3\mathrm{P}^0$. Autoionizing transitions into the ^{4}S continuum are indicated by orange arrows with the predicted energy of the ejected electron. Adapted from [181]. (**b**): Autoionization spectrum measured in the 0- to 3.5 eV kinetic energy range. Differences in the amplitude of paired peaks is only due to shape of the background, which was not subtracted [182].

or autoionization. The electrons gain the energy difference between the state and the ionisation potential of the continuum. The corresponding energy term diagram is shown in fig. 4.10a, nicely illustrating the different states $3s''$, $3d'$ and $2s2p^5$, which contribute with different electron energies. Later measurements proved the autoionization spectrum observed by Wills [180], who measured the kinetic energy of released electrons up to 4.738 eV. In addition to eq. 4.29, ultrafast dissociation with two excited oxygen atoms was observed. One is core-excited and the other valence-excited, leading to a doppler splitting, which can be seen in the autoionization spectrum fig. 4.10b. The roman letters refer to peak labels, whose assignment can be found in app. tab. A.6.

In order to further specify contributions of autoionizing excited states other elements were taken into account. In particular, transition elements such as iron and chromium revealed a high number of different autoionizing states [184–187] and are predominantly present in the main spectrometer stainless steel. The spectrum of neutral iron atoms of autoionizing Rydberg series can be found in app. fig. A.20. There, each peak corresponds to an autoionizing level, reached via three step laser excitation.

In general, atomic autoionization is a well-motivated potential contribution because it provides electron energies up to a few electronvolts. In contrast, the lifetime of autoionizing excited Rydberg states is limited. Due to the resonant generation, the lifetime is of similar duration as other resonant transitions. It takes place during picoseconds such as the de-excitation of core-excited electrons. Therefore, excited atoms in autoionizing states from sputtering at the main spectrometer vessel wall, can not be background contributor inside the entire volume.

4.4.3. Doubly excited states - Planetary atoms

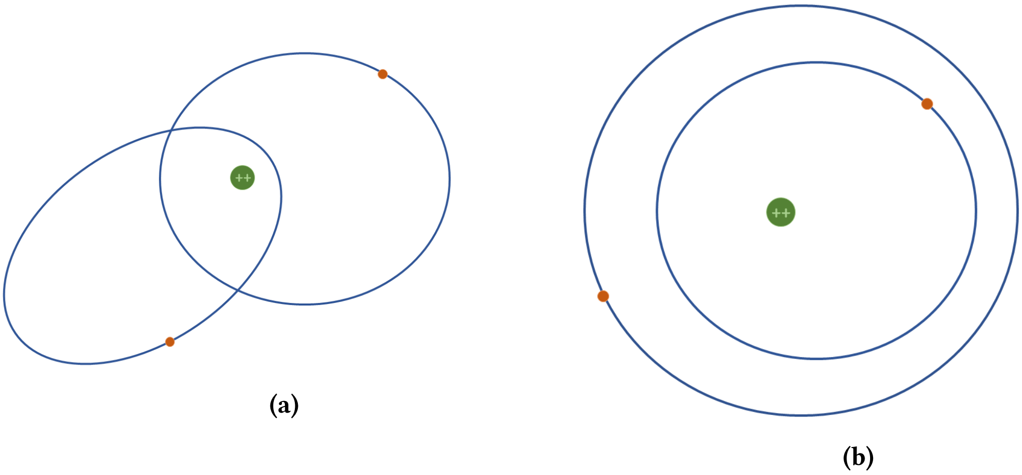

(a)

(b)

Figure 4.11.: (**a**): Scheme of doubly excited state of type 2 - overlap is significant.
(**b**): Doubly excited state of type 1 - overlap with ground state or first few excited is negligible.

Doubly excited states are the most prominent candidate of autoionizing states [188–190]. These states can be classified into two types. Type 1 systems (fig. 4.11b) are characterised by a negligible overlap with the ground state or other excited states, which are not optically accessible. In contrast, type 2 system (fig. 4.11a) are accessible by direct optical excitation from low states and show a significant overlap of the excited electrons.[188]

Let us first consider type 2 of doubly excited systems on the example of helium atoms, where the excited electrons move in similar regions of space ($\langle r_1 \rangle \sim \langle r_2 \rangle$). The Rydberg series with the configuration $2ln'l'$ ($n' \geq 2$) is given with the Rydberg formula eq. 4.1 by

$$W_{2ln'l'} = -\frac{Z^2}{2}\left(\frac{1}{4} + \frac{1}{n'^2}\right) \geq -\frac{Z^2}{4} \quad . \tag{4.30}$$

Hence, the doubly excited states are expected at energies $\geq -1E_H = 27.2$ eV for He ($Z = 2$), the doubly excited state $2ln'l'$ lies in the ionisation continuum of $\mathrm{He}^+ + \mathrm{e}^-$, since the binding energy of He^+ ions is $-2E_H$. The second electron returns to the ground state of the $\mathrm{He}^+(1\mathrm{s})$ ion, while the initial photon energy $\hbar\omega$ of excitation is transformed to the ion formation and partially to the ejected electron. The electrons kinetic energy is given by the difference of the incident photon $\hbar\omega$ and the ionisation energy W_I.[73]

Electron spectroscopy of doubly excited helium atoms [191] produced by double electron capture of He^{2+} ions with Ba atoms were performed. The observed transitions from different $nln'l'$ to different ion states, revealed the electron energy spectrum in figure 4.12. The higher energy electrons (> 35 eV) corresponds to the autoionization process $\mathrm{He}^{**}(2ln'l') \longrightarrow \mathrm{He}^+(1s)$ with $n' \geq 2$. The low energy part from 3 to 8 eV complies with transitions, where $n = 3$ and $n' \geq 3$. The series relating to $n = 4$, $n' \geq 4$ is limited at 2.65 eV, thus lower electron energies correspond to excitations with $n \geq 5$.

Although the low electron energy part would fit to our observation in the KATRIN main spectrometer, one must always consider the lifetimes of such states. The discrete

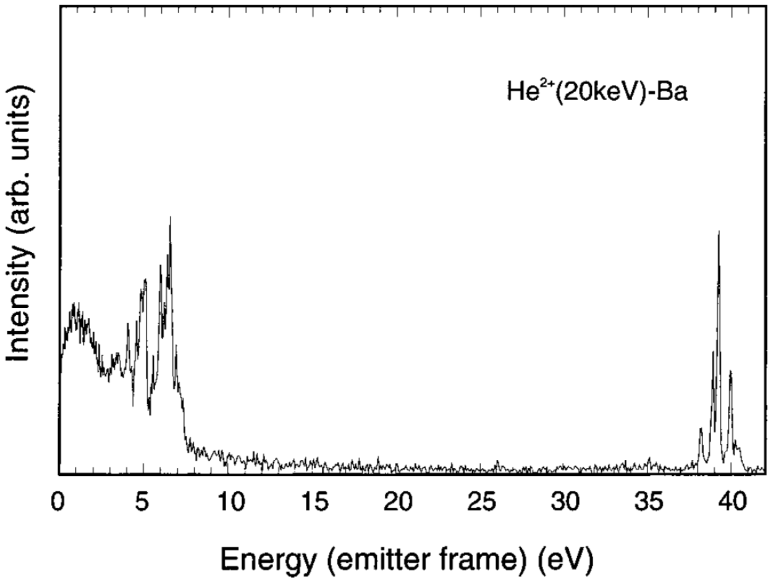

Figure 4.12.: Ejected electron spectrum ranging from 0 to 42 eV that are measured in the forward direction for He^{2+} + Ba collisions at ion collision energy of 20 keV [191].

excited states may also undergo radiative transitions to a lower state, below the ionisation limit by light emission [168]. The lifetime is therefore dependent on the radiative and the radiationless transitions. In general, autoionization predominates over allowed radiative transitions, whose lifetimes are in the order of $10^{-7} - 10^{-9}$ s. Since autoionization was predominately observed, the lifetime of such states is estimate to be in the order $10^{-11} - 10^{-15}$ s, and therefore extremely fast, similarly to the ICD.[168]

Type 1 doubly excited atoms (fig. 4.11b) are more important since they are more abundant [188, 192]. Their excited electrons move in different regions ($\langle r_1 \rangle < \langle r_2 \rangle$), so they comprise of asymmetrically excited electrons with different principal quantum numbers n_1 and n_2, and so there is no significant overlap of their residence probability. The configuration is described by the bound three-body Coulomb system [137, 193]. Such states are called 'planetary atoms' [194], since the electrons motion can be expounded by celestial mechanics, with Kepler orbits, while they depend only on the charge on not on the detailed structure of the ionic core [188]. In general, the energetically overlap of different Rydberg series of low double excitation lead to the interference of resonances and may cause drastic change in the pattern of states. But for asymmetrically highly doubly excited states this interference may lead to surprisingly large lifetimes of the resonance [195].

The basic mechanism of interference is the superposition of different states, described by wave packets, which build up a new solution of the relevant equation. Consider two states which decay into a common continuum. These states may be mixed by a residual interaction and superposing the coupling matrix elements may lead to cancellation of the resulting coupling. This destructive interference leads to enhanced lifetimes of several orders of magnitude for particle decay processes, such as autoionization, and as a special case to a bound state in the continuum if the resulting coupling matrix element vanishes, so the new state does not decay at all.[195]

Percival [188] established a theoretical framework to investigate some characteristics of such planetary atoms. According to celestial mechanics under Coulomb force, he derived a semiclassical theory of bound states with usage of E.B.K. (Einstein, Brillouin, & Keller) quantisation. Bound states are described by two dimensional invariant toroids in a four dimensional phase space. These can be chosen as action integrals I_1 and I_2, which are line integrals around the major and minor axes of the toroid. The connection between bound states and these invariant toroids are given by quantised action integrals

$$I_k = \gamma_k \hbar \text{ or } I_k = (\gamma_k + \frac{1}{2})\hbar \ . \tag{4.31}$$

The energies of the invariant toroids is equal to the bound states and by deriving scaling laws from generalised Kepler laws leads to an energy relation

$$E' = \frac{E}{(2\nu)^2} \ , \tag{4.32}$$

scaled by a positive scaling factor 2ν. In particular, for any positive constant 2ν there exists an invariant toroid with action integrals $(2\nu I_1, 2\nu I_2)$, but only for particular values of 2ν will this toroid correspond to a quantum state. Those values are either $(2\nu\gamma_1)$ an integer or $(2\nu\gamma_2 + \nu)$ a half-odd integer. The original lowest value of energy corresponding to any 2ν is called the fundamental state and all higher states are called overtones, according to $\nu = 1/2, 3/2, 5/2, 7/2, \ldots$. The important characteristic is the lifetime of these states, which is given by

$$\tau = T_{1/2}(2\nu)^3 \exp\left(2\nu \frac{2A_{1/2}}{\hbar}\right) \ , \tag{4.33}$$

where $T_{1/2}$ and $A_{1/2}$ correspond to the orbiting time and the classical action function, respectively. So if the fundamental of the series has a low quantum number and is of type 2, one obtains an expected lifetime on the order of 10^{-13} s. However, the lifetime of the type 1 overtones rapidly increases with the order of the overtone, in that way, that the fourth overtone nearly reaches an approximated electrostatic decay lifetime of 1 s.

These lifetimes would nicely exceed the necessary lifetimes of excited atoms in the KATRIN main spectrometer. As mentioned before, these type 1 planetary atomic states are not produced by direct optical excitation from low states, but are accessible by low energy electron scattering with atomic ions or atoms

$$\begin{aligned} e^- + A^+ &\longrightarrow A^{**} \\ e^- + A &\longrightarrow A^{**} + e^- \\ A^{**} &\longrightarrow A^+ + e^- \ . \end{aligned} \tag{4.34}$$

Statistically they predominate over the type 2 states and are long-lived since they behave like bound states embedded in a continuum due to the destructive interference of their electrostatic coupling [188, 195]. However, radiative transitions may occur, leading to a type 2 state, which decays extremely fast. Therefore, any planetary state could contribute as an electron source in the KATRIN main spectrometer, if a resonant decaying state is reached inside the entire volume. The positive ions or atoms as well as the low energy electrons, necessary for the double excitation process, are in attendance at the sputtering process. Along with the sputtered atoms, electrons are leaving the surface with mean energies of a few eV [82]. The mean energy of double excitation can be estimated to be equal to the energy required to ionise both planetary electrons [188]. Further investigations should be undertaken in this regard, such as an estimation of double excitation at atom/ion electron scattering by sputtered particles from the main spectrometer surface.

5. Test of Rydberg-emisson from short lived ^{223}Ra source

During the STSIIIa measurement phase, background studies at the spectrometer section were performed. Based on a proposal from May 2018 [196], a radioactive source consisting of ^{223}Ra (radium) was introduced into the main spectrometer with the aim of deliberate formation of Rydberg atoms.

Measurement setup and principle

The radium isotope ^{223}Ra has a half-life of $T_{1/2}^{\mathrm{Ra}} = 11.43\,\mathrm{d}$ and is therefore a short-living one. The decay chain is shown in app.fig. A.23, showing that all daughter nuclei have very short half-lives. The longest one is for β^- decay of ^{211}Pb with a half-life of $T_{1/2}^{\mathrm{Pb}} = 36.1\,\mathrm{min}$.

The radioactive element was implanted into 2 probes of regular stainless steel and into 2 probes with an additional gold surface layer. The source was produced by the mass separator ISOLDE at CERN with a mean implantation energy of $30 - 50\,\mathrm{keV}$ of radium atoms. It was proposed by E. Otten that the surface gold layer might decrease the production of Rydberg atoms efficiently.

The sample holder consists of a plug-in module, which was inserted into the main spectrometer through a port at the downstream steep cone in a way that the radioactive source probe is at the inner surface. The construction includes the possibility to apply additional high voltage on the sample holder. This leads to high electric field strength near the sample on the order of $F \approx 5 \cdot 10^5\,\mathrm{V/m}$, which is sufficient to field ionise generated Rydberg atoms with effective principal quantum numbers of $n^* > 16$.

Since one daughter of ^{223}Ra is well-known ^{219}Rn, we expect radon emanation of recombined radon recoils within the samples. However, the implantation energy is less than the recoil energies of the daughters which are on the order of 100 keV, thus their explantation probability is high. Therefore, radon should be explanted efficiently and emanation with induced radon background was considered to be negligible.

Aim of the measurements

The measurements were proposed to further investigate the Rydberg background model. By contaminating the main spectrometer surface with radioactive isotopes of very short half-lives, the Rydberg background might be reproduced with higher rates from the spectrometer surface as well as the source probe itself. The events from Rydberg atoms by sputtering from the sample holder can therefore be separated from the residual events by applying high voltage on the sample holder. In addition the effect of the gold layer on the production of Rydberg atoms shall be observed.

The radioactive contamination has to be observed in detail since sustained contamination must not take place. The radiopurity of the source was checked by ISOLDE and cross contamination by neighbouring atoms is about 10^{-4}. Therefore, the background level should be identical before and after the measurement phase.

Results of the ^{223}Ra measurements

Investigating Rydberg background directly from the source was not feasible to observe since an unexpected high rate of emanating radon was brought into the main spectrometer by the source after the first insertion. Indeed, we expected slight emanation of recombined radon-219 but not in the high observed quantity. The rate was about 2 kcps due to stored conversion electrons from radon decays (see sec. 2.2.4) and therefore two orders of magnitude higher than the expected Rydberg background. The detector event map can be seen in app.fig. A.21 nicely illustrating the expected radial profile of radon induced background with increasing rate for smaller radii. Additional measurements with asymmetric magnetic field setting (see fig. 2.15) were performed because no electrons can be trapped at these settings, and therefore radon induced background by stored conversion electrons can not occur. The rate with open valve was about 10.5 kcps, wherein the nominal background level is 2.5 kcps by electrons from the inner surface. This increase corresponds to an induced rate increase by a factor of 3.2 which was roughly expected due to four alpha decays within the decay chain which may contribute. Since radon induced background overwhelms other contributors, studying the Rydberg background is only possible with closed valve to the source. In the case of emanating radon the following measurements were performed with alternating magnetic field settings so no radon induced electrons are

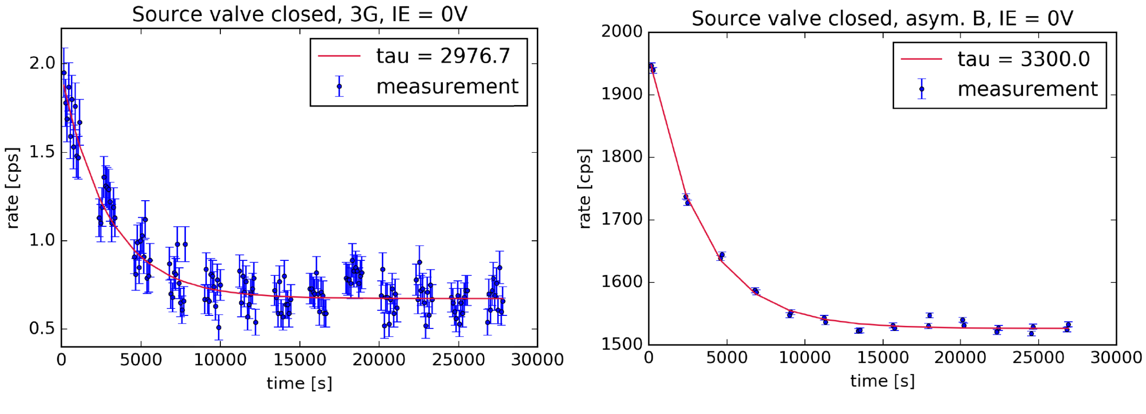

(a) **(b)**

Figure 5.1.: (**a**): Rate after removal of radon induced background electrons with symmetric magnetic field. The exponential fit function provides $\tau = (2976.7 \pm 207.8)$ s, corresponding to a half-life of $T_{1/2} = \ln(2) \cdot \tau = (34.4 \pm 2.4)$ min. (**b**): Rate after removal of radon induced background electrons with asymmetric magnetic field, looking onto the inner surface. The exponential fit function gives $\tau = (3300.0 \pm 51.9)$ s, which corresponds to a half-life of (38.1 ± 0.6) min. The expected literature value is $T_{1/2}^{\mathrm{Pb}} = 36.1$ min.

stored for long time periods. After the valve was closed the rate diminution by subsiding radioactivity was observed and is shown in fig. 5.1 and fit by the exponential function

$$R(t) = a \cdot \mathrm{e}^{(-t/\tau)} + c \quad . \tag{5.1}$$

The dominant part of the diminution is caused by slowest decay of the daughter ^{211}Pb.

Since the source half-life ($T_{1/2}^{\mathrm{Ra}} = 11.43\,\mathrm{d}$) is short and the source produces too much radon induced background, measurements at increased pressure would not make a separation of radon and Rydberg induced background and an energy investigation possible. However, in order to compare the induced background with the nominal one, the characteristic dependence on the inner electrode voltage V_{IE} can be investigated after the valve to the source is closed. Additionally, during the contamination the activation saturation of volume activity by decaying radon to surface activity can be studied.

After the valve was opened, measurements with asymmetric magnetic field were performed to study the activation saturation. The time between opening the valve and starting the measurements was about 8 minutes because of the ramp up the high voltage and the inner electrode. For isotopes where the half-life of the parent isotope is much larger than the one of the daughter, transient equilibrium is expected to occur after approximately four half-lives. Therefore, activation saturation is described by Bateman's equation [197]:

$$A_{\mathrm{Pb}}(t) = A_{\mathrm{Ra}}(0)\frac{\lambda_{\mathrm{Pb}}}{\lambda_{\mathrm{Pb}} - \lambda_{\mathrm{Ra}}}\left(\mathrm{e}^{-\lambda_{\mathrm{Ra}}t} - \mathrm{e}^{-\lambda_{\mathrm{Pb}}t}\right) + A_{\mathrm{Pb}}(0)\mathrm{e}^{-\lambda_{\mathrm{Pb}}t} \quad , \tag{5.2}$$

where $A(0)$ denotes the activity of the isotopes Pb and Ra at $t = 0$ and $\lambda = \ln(2)/T_{1/2}$ the exponential decay constant. $A_{\mathrm{Pb}}(0)$ is assumed to be zero.

The initial measured rate was about 7 kcps, much higher than expected, possibly due to a large amount of radon, released to the volume after opening the valve. Nevertheless, after

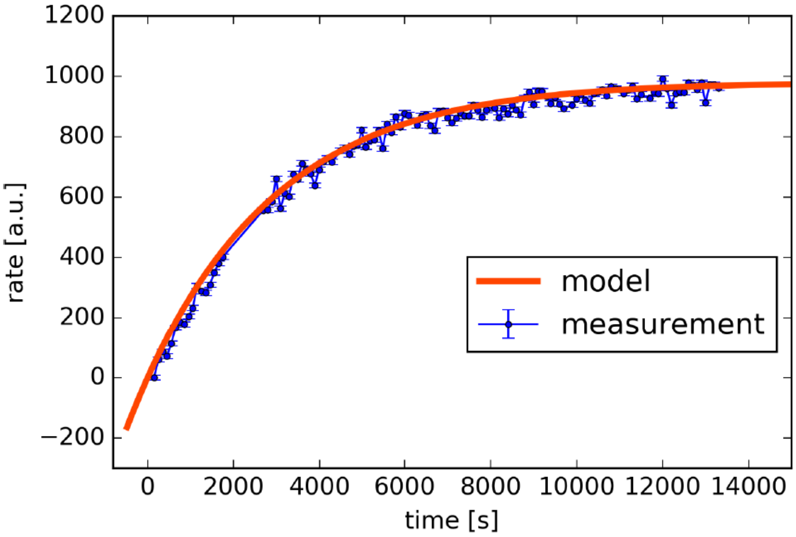

Figure 5.2.: Rate as a function of time after opening the valve to the source at $t = -480\,\mathrm{s}$ (blue). The observed initial rate was subtracted such that the rate is zero at $t = 0$. The red curve is the overlayed Bateman equation, starting at $t = -480s$ when the valve was opened with the corresponding literature values of λ.

Table 5.1.: Collected information about the rates: Calculated N_0 via eq. 5.3 with the measured rate at different inner electrode settings of 0 V, 20 V, and 200 V.

V_{IE} (V)	rate (cps)	# events	N_0 (cps)	f_{red}	(Trost)[128]
200	1.0617 ± 0.0401	1168	1.706	0.679 ± 0.049	0.65
20	0.8965 ± 0.0412	986	2.198	0.874 ± 0.083	0.82
0	0.6690 ± 0.0417	736	2.512	1	1

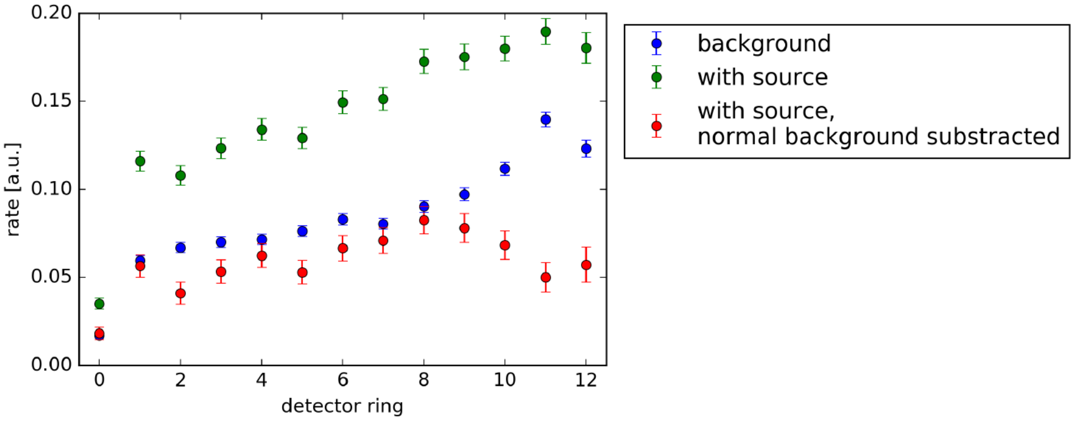

Figure 5.3.: Radial rate distribution of the nominal background (blue) and with the source (green) as well as the induced subtracted by the nominal one (red).

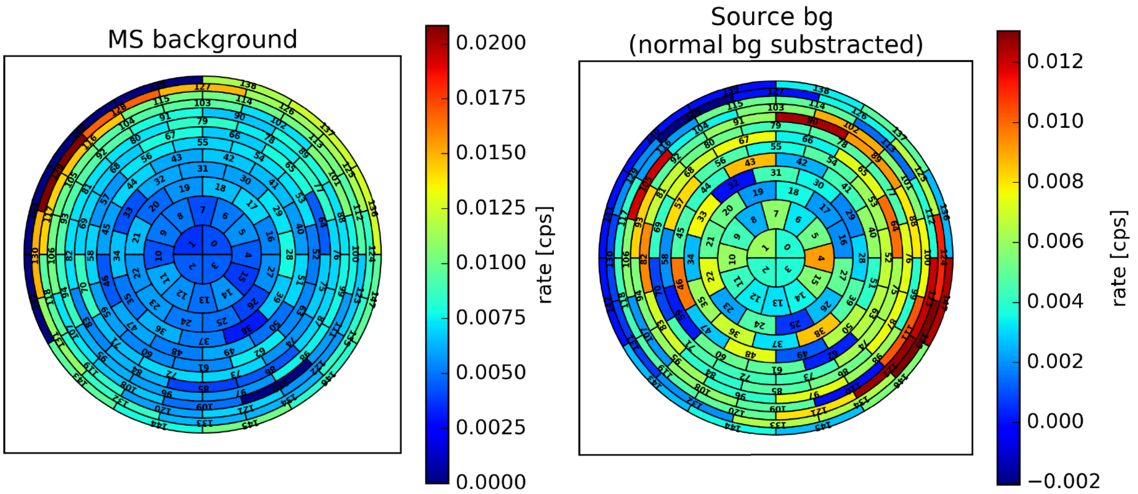

(a) **(b)**

Figure 5.4.: Pixel distribution (**a**): of nominal main spectrometer background. (**b**): of induced background after contamination. Pixels on the upper left as well as pixel 110 are excluded.

subtracting this initial rate, Bateman's equation is appropriate to describe the activation saturation as it can be seen in fig. 5.2. The expected time till saturation at transient equilibrium is about four half-lives, corresponding to $t = 4 \cdot 36.1\,\text{min} = 8664\,\text{s}$, which can also be confirmed.

After saturation was reached the valve was closed and the diminution was observed at different inner electrode voltages to compare to the behaviour of the induced background. This was performed with a symmetric magnetic field setting with additional magnetic pulses to remove stored electrons. The settings are 0 V, 20 V and 200 V in order to get three well separated points. The inner electrode voltage dependence was investigated in detail by N. Trost [128] and its rate dependence can be found in app.fig. A.22. The expected rate of each measurement during the diminution with a half-life of 36.1 min is given by

$$N(t_0, t_1) = N_0 \cdot \int_{t_0}^{t_1} dt\ \mathrm{e}^{-t/\tau} \quad , \tag{5.3}$$

where $t_0 < t_1$. Since $V_{\mathrm{IE}} = 200\,\text{V}$ causes the largest reduction, this setting was measured at first. By comparison of the three N_0 which give the rate at $t = 0$, one obtains the reduction factors

$$f_{\mathrm{red}} = \frac{N_0(V_{\mathrm{IE}})}{N_0(0\,V)}, \tag{5.4}$$

in reference to 0 V on the inner electrode.

Table 5.1 shows the measured rate and calculated N_0 at three different inner electrode voltage settings, leading to a calculated reduction factor f_{red}, and the reference value by N. Trost [128].

The resulting inner electrode voltage dependence of the ^{223}Ra induced background in tab. 5.1 is in agreement with the known reduction factor of the nominal background by Trost [128] within 1σ. This indicates that the radioactive contamination of the main spectrometer with the ^{223}Ra source, produces background in the same manner as it is commonly assumed to be generated by radioactivity of ^{210}Pb.

Another characteristic which can be investigated with these measurements, is the radial dependence of the induced background. The rate is expected to increase towards outer rings since more short-living Rydberg states with low n produce background through spontaneous decay or BBR near to the walls. Therefore, the induced background is assumed to show a similar behaviour in the radial distribution. Figure 5.3 shows this radial distribution as a function of the detector rings. As expected, the background rate with the source increases to higher radii but by subtracting the measured nominal background, a different behaviour can be seen. The rate initially increases as expected but then decreases to the outermost rings. A possible explanation of this discrepancy is an inhomogeneous allocation of ^{211}Pb on the inner spectrometer surface, resulting in an irregularly distributed background rate.

This hypothesis is confirmed by investigating the pixel distribution. Figure 5.4a shows the nominal background with its homogeneously behaviour and slight increase to higher radii but in contrast, fig. 5.4b illustrates the induced background distribution subtracted by the nominal one. The rate is not homogeneously distributed as it shows a strong hotspot on the right detector half. Therefore, the radial dependence can not be compared directly, whereas a simulation of the radial profile by a localised source could help to understand this observation.

In a nutshell, the measurements revealed that radioactivity contributes indirectly as a background source, as it was also shown with the thorium measurements during SDS-II. In addition, the expected dependence on the inner electrode potential could be reproduced. The activation saturation of surface activity by volume radioactivity could also be shown as well as the expected diminution of exponential decay of the daughter isotopes. New proposals for further investigation of the Rydberg background with radioactive sources are under discussion, whereby high demands are placed on the absence of radon. ^{212}Pb as the source is a good candidate because the half-life is about 11 h and therefore more suitable for longer investigations.

6. Conclusion

The KATRIN main spectrometer background has been investigated in detail during previous measurement phases. The background level exceeds the design value of 0.01 cps by a factor of 50 which degrades the sensitivity to the neutrino mass measurement. Due to optimised settings, scanning and analysis strategies, an unprecedented sensitivity of 240 meV/c^2 on the effective electron anti neutrino mass can be achieved. In spite of this, our goal is to fully understand, and possibly reduce further, every contribution of the remaining main spectrometer background.

The independence of the magnetic field strength and the pressure in addition to the homogeneous distribution over the main spectrometer volume, shows that the background characteristics do not match previously observed processes. The small dependence on the inner electrode potential as well as the rate decrease after bake-out, and the radial profile, indicate a correlation between processes from the inner spectrometer surface and the volume. Due to measurements with radioactive sources (^{228}Th and ^{223}Ra) by deliberate contamination of the main spectrometer, this correlation between background events from the inner spectrometer surface and the volume was observed and quantified. Earlier measurements revealed the contamination of long-living ^{210}Pb ($T_{1/2} = 22$ years) with an estimated activity of $\approx$ 1 kBq, which is generally accepted as the main contributor of the spectrometer background. However, the mechanism of how background electrons are generated in the entire volume is still under investigation. The generally assumed mechanism is the formation of a neutral messenger who carries electrons unhindered by the inner electrode wires inside the volume and ionises under electron emission.

These neutral messengers might be Rydberg atoms, highly excited atoms whose characteristics partly match those of the observed background. They are generated by sputtering processes at the main spectrometer surface due to the radioactive decay of ^{210}Pb.

Sputtering simulations have been performed with the SRIM code. The simulation yields insights to the kinematics of sputtered atoms from solids but not on excitation. The atomic composition of targets is chosen by relative amounts of elements. These atomic elements are only randomly distributed, neglecting chemical compounds such as Cr_2O_3. Molecules or ions are not considered and there is no information about sputtering of these. Nonetheless the simulation delivers characteristics of the sputtering process, developing the Rydberg model. Theoretically, sputtered atoms might be in excited states by resonant electron transfer from the solid surface.

N. Trost argued in his PhD thesis [128] that the interaction of Rydberg atoms with the thermal black body radiation could cause the ionisation of these under electron emission to produce the observed background rate. In contradiction to that are dipole measurements which disclosed background electrons with energies up to 4 eV, whereby via BBR interaction generated electrons only have energies lower than 0.2 eV.

Hence, other ionisation mechanisms of Rydberg atoms must be considered that provide electrons with higher initial energies. Penning ionisation or in general, chemi-ionisation reactions are suitable choices of ionisation mechanisms, providing these electron energies. However, these reactions are only accessible via collisions of excited atoms with atoms, molecules, ions, or molecular ions. Since the pressure inside the main spectrometer is on the order of $\sim 10^{-11}$ mbar, collisional ionisation is highly improbable inside the volume. Collisional ionisation still occurs close to the spectrometer surface of sputtered atoms because their lateral spread is small. Additionally, this results in further restriction if excited sputtered atoms should be able to reach the inner volume, they must not ionise there, or their excitation and ionisation takes place within the volume.

Besides collisional ionisation, field ionisation is considered. The electric field between the vessel surface and the inner electrode provides field strengths which perturb the behaviour of Rydberg states due to the Stark effect. The resulting energy splitting may lead to ionisation if the excitation is sufficiently high. However, this will also lead to electrons from the spectrometer wall and not within the entire volume. Therefore, a more unusual suggestion, the phenomenon of autoionization, was suggested. Research in the literature revealed that many autoionizing states exist for different elements. The ejected electron energies obtained by autoionization fit very well to the observation and have therefore been further investigated. But all these states do not provide the necessary lifetime of about 10^{-3} s since the ionisation has to take place inside the volume.

Nevertheless, there is a candidate who seems less likely but still possible. Planetary atoms, highly doubly excited atoms which autoionize if their excited electrons resonantly interact with each other. Depending on the excitation configuration, planetary atoms autoionize within picoseconds. However, the more abundant configuration of highly double excitation may provide destructive interference of the interaction of the electrons. Thereby the lifetime of such states is significantly enhanced, up to seconds. Due to radiative transitions a resonant interacting ensemble can be generated which autoionizes immediately, which can occur at any point in time. Although this planetary atom configuration seems rather unlikely, there is a probability that this phenomenon might be a solution for the observed initial energy spectrum of background electrons in the volume of the main spectrometer.

The measurements with a radioactive ^{223}Ra source were not performed as initially planned. The contributions of a Rydberg-induced background directly from the source could not be separated from radon-induced events. However, deliberate contamination increased the overall background level in order to reproduce some characteristics of the remaining background. Hence, the dependency on the inner electrode potential was reproduced as it was expected from measurements by N. Trost. In addition the activation saturation of the main spectrometer surface by the radioactive source was observed and its diminution after the valve to the ^{223}Ra source was closed. Further measurements with a ^{212}Pb source are in discussion, whereby no radon contamination of the source has high priority. This isotope is more suitable since its half-life is about 11 hours.

Bibliography

[1] W. Pauli. “Offener Brief an de Gruppe der Radioaktiven der Gauvereins-Tagung zu Tübingen: Zürich 4. Dec. 1930”. In: ().

[2] C. L. Cowan et al. “Detection of the Free Neutrino: a Confirmation”. In: *Science (New York, N.Y.)* 124.3212 (1956), pp. 103–104. ISSN: 0036-8075. DOI: `10.1126/science.124.3212.103`.

[3] F. Reines et al. “Detection of the Free Antineutrino”. In: *Physical Review* 117.1 (1960), pp. 159–173. ISSN: 0031-899X. DOI: `10.1103/PhysRev.117.159`.

[4] G. Danby et al. “Observation of High-Energy Neutrino Reactions and the Existence of Two Kinds of Neutrinos”. In: *Physical review letters* 9.1 (1962), pp. 36–44. ISSN: 0031-9007. DOI: `10.1103/PhysRevLett.9.36`.

[5] R. Davis. “A review of the homestake solar neutrino experiment”. In: *Progress in Particle and Nuclear Physics* 32 (1994), pp. 13–32. ISSN: 01466410. DOI: `10.1016/0146-6410(94)90004-3`.

[6] B. T. Cleveland et al. “Update on the measurement of the solar neutrino flux with the Homestake chlorine detector”. In: *Nuclear Physics B - Proceedings Supplements* 38.1-3 (1995), pp. 47–53. ISSN: 09205632. DOI: `10.1016/0920-5632(94)00732-B`.

[7] Q. R. Ahmad et al. “Direct evidence for neutrino flavor transformation from neutral-current interactions in the Sudbury Neutrino Observatory”. In: *Physical review letters* 89.1 (2002), p. 011301. ISSN: 0031-9007. DOI: `10.1103/PhysRevLett.89.011301`.

[8] Y. Fukuda et al. “Evidence for Oscillation of Atmospheric Neutrinos”. In: *Physical review letters* 81.8 (1998), pp. 1562–1567. ISSN: 0031-9007. DOI: `10.1103/PhysRevLett.81.1562`.

[9] Ch Kraus et al. “Final results from phase II of the Mainz neutrino mass searchin tritium beta decay”. In: *The European Physical Journal C* 40.4 (2005), pp. 447–468. ISSN: 1434-6044. DOI: `10.1140/epjc/s2005-02139-7`.

[10] J. Chadwick. *Intensitätsverteilung im magnetischen Spektrum von β - Strahlen von Radium.* 1914.

[11] E. Fermi. “Versuch einer Theorie der β-Strahlen. I”. In: *Zeitschrift fr Physik* 88.3-4 (1934), pp. 161–177. ISSN: 1434-6001. DOI: `10.1007/BF01351864`.

[12] J. Steinberger. “The history of neutrinos, 1930–1985. What have we learned about neutrinos? What have we learned using neutrinos?” In: *Annals of Physics* 327.12 (2012), pp. 3182–3205. ISSN: 00034916. DOI: `10.1016/j.aop.2012.07.012`.

[13] Lise Meitner. “Über die Entstehung der β-Strahl-Spektren radioaktiver Substanzen”. In: *Zeitschrift für Physik* 9.1 (1922), pp. 131–144. ISSN: 0044-3328. DOI: `10.1007/BF01326962`.

[14] F. Reines and C. L. Cowan. “A Proposed Experiment to Detect the Free Neutrino”. In: *Physical Review* 90.3 (1953), pp. 492–493. ISSN: 0031-899X. DOI: `10.1103/PhysRev.90.492.2`.

[15] G. Feinberg. “Decays of the μ Meson in the Intermediate-Meson Theory”. In: *Physical Review* 110.6 (1958), pp. 1482–1483. ISSN: 0031-899X. DOI: `10.1103/PhysRev.110.1482`.

[16] D. DeCamp et al. “Determination of the number of light neutrino species”. In: *Physics Letters B* 231.4 (1989), pp. 519–529. ISSN: 03702693. DOI: `10.1016/0370-2693(89)90704-1`.

[17] M. L. Perl et al. “Evidence for Anomalous Lepton Production in e^+-e^- Annihilation”. In: *Physical review letters* 35.22 (1975), pp. 1489–1492. ISSN: 0031-9007. DOI: `10.1103/PhysRevLett.35.1489`.

[18] K. Kodama et al. “Observation of tau neutrino interactions”. In: *Physics Letters B* 504.3 (2001), pp. 218–224. ISSN: 03702693. DOI: `10.1016/S0370-2693(01)00307-0`.

[19] CERN ATLAS Experiment. *Atlas-Standard-Model-2*. 2018. URL: `https://atlas.cern/discover/physics`.

[20] Robert Oerter. *The theory of almost everything: The standard model, the unsung triumph of modern physics*. New York: Plume, 2014. ISBN: 978-1-101-12674-5.

[21] K. S. Hirata et al. “Real-time, directional measurement of B8 solar neutrinos in the Kamiokande II detector”. In: *Physical Review D* 44.8 (1991), pp. 2241–2260. ISSN: 0556-2821. DOI: `10.1103/PhysRevD.44.2241`.

[22] Q. R. Ahmad et al. “Measurement of the rate of $\nu_e + d \rightarrow p + p + e^-$ interactions produced by (8)B solar neutrinos at the Sudbury Neutrino Observatory”. In: *Physical review letters* 87.7 (2001), p. 071301. ISSN: 0031-9007. DOI: `10.1103/PhysRevLett.87.071301`.

[23] Nicola Cabibbo. “Unitary Symmetry and Leptonic Decays”. In: *Physical review letters* 10.12 (1963), pp. 531–533. ISSN: 0031-9007. DOI: `10.1103/PhysRevLett.10.531`.

[24] Makoto Kobayashi and Toshihide Maskawa. “CP -Violation in the Renormalizable Theory of Weak Interaction”. In: *Progress of Theoretical Physics* 49.2 (1973), pp. 652–657. ISSN: 0033-068X. DOI: `10.1143/PTP.49.652`.

[25] Susanne Mertens. *Background Processes in the Electrostatic Spectrometers of the KATRIN Experiment*. Cham: Springer International Publishing, 2014. ISBN: 978-3-319-01176-9. DOI: `10.1007/978-3-319-01177-6`.

[26] L. Wolfenstein. “Neutrino oscillations in matter”. In: *Physical Review D* 17.9 (1978), pp. 2369–2374. ISSN: 0556-2821. DOI: `10.1103/PhysRevD.17.2369`.

[27] Tsunayuki Matsubara and on behalf of the Double Chooz collaboration. *First result from the Double Chooz reactor-neutrino experiment*. URL: `http://arxiv.org/pdf/1205.6685v1`.

[28] F. P. An et al. “Observation of electron-antineutrino disappearance at Daya Bay”. In: *Physical review letters* 108.17 (2012), p. 171803. ISSN: 0031-9007. DOI: `10.1103/PhysRevLett.108.171803`.

[29] S. Abe et al. “Precision measurement of neutrino oscillation parameters with KamLAND”. In: *Physical review letters* 100.22 (2008), p. 221803. ISSN: 0031-9007. DOI: `10.1103/PhysRevLett.100.221803`.

[30] P. F. de Salas et al. *Neutrino Mass Ordering in 2018: Global Status*. URL: `http://arxiv.org/pdf/1806.11051v1`.

[31] P. F. de Salas et al. “Status of neutrino oscillations 2018: 3 sigma hint for normal mass ordering and improved CP sensitivity”. In: *Physics Letters B* 782 (2018), pp. 633–640. ISSN: 03702693. DOI: `10.1016/j.physletb.2018.06.019`.

[32] Max Tegmark et al. “The Three–Dimensional Power Spectrum of Galaxies from the Sloan Digital Sky Survey”. In: *The Astrophysical Journal* 606.2 (2004), pp. 702–740. ISSN: 0004-637X. DOI: `10.1086/382125`.

[33] Max Tegmark. “Cosmological Neutrino Bounds for Non-Cosmologists”. In: *Physica Scripta* T121 (2005), pp. 153–155. ISSN: 0031-8949. DOI: `10.1088/0031-8949/2005/T121/023`.

[34] Julien Lesgourgues. “Galaxies weigh in on neutrinos”. In: *Physics* 3 (2010). DOI: `10.1103/Physics.3.57`.

[35] S. Hannestad. “Neutrino physics from precision cosmology”. In: *Progress in Particle and Nuclear Physics* 65.2 (2010), pp. 185–208. ISSN: 01466410. DOI: `10.1016/j.ppnp.2010.07.001`. URL: `http://arxiv.org/pdf/1007.0658v2`.

[36] Florian. *Massenparabeln für Kerne mit ungeradem A und odd/odd- bzw. even/even-Kerne zur Erläuterung des doppelten β-Zerfalles*. 2005. URL: `https://de.wikipedia.org/wiki/Doppelter_Betazerfall#/media/File:Doppelbeta-massenparabel.png`.

[37] G. Drexlin. “Direct neutrino mass searches”. In: *Nuclear Physics B - Proceedings Supplements* 138 (2005), pp. 282–288. ISSN: 09205632. DOI: `10.1016/j.nuclphysbps.2004.11.064`.

[38] *GERDA homepage: The GERmanium Detector Array*. URL: `https://www.mpi-hd.mpg.de/gerda/`.

[39] *EXO-200 homepage: Enriched Xenon Observatory*. URL: `http://www-project.slac.stanford.edu/exo/`.

[40] *MAJORANA homepage: Neutrinoless Double-beta Decay Experiment*. URL: `https://www.npl.washington.edu/majorana/`.

[41] J. Angrik et al. *KATRIN Design Report 2004*. FZKA–7090. Forschungszentrum Karlsruhe, 2005.

[42] S. Rupp. *Development of a highly sensitive hollow waveguide based Raman system for the compositional analysis of the KATRIN tritium source gas: PhD thesis*. Karlsruhe Institute of Technology KIT, 2016.

[43] L. Kuckert. *The windowless gaseous tritium source of the KATRIN experiment: Characterisation of gas dynamical and plasma properties: PhD thesis*. Karlsruhe Institute of Technology KIT, 2016.

[44] E. Ellinger et al. “Monitoring the KATRIN source properties within the beamline”. In: *Journal of Physics: Conference Series* 888 (2017), p. 012229. ISSN: 1742-6588. DOI: `10.1088/1742-6596/888/1/012229`.

[45] Florian Heizmann and Hendrik Seitz-Moskaliuk. “The Windowless Gaseous Tritium Source (WGTS) of the KATRIN experiment”. In: *Journal of Physics: Conference Series* 888 (2017), p. 012071. ISSN: 1742-6588. DOI: `10.1088/1742-6596/888/1/012071`.

[46] F. Friedel et al. *Time dependent simulation of the flow reduction of D_2 and T_2 in the KATRIN experiment*. URL: `http://arxiv.org/pdf/1807.10126v2`.

[47] Woosik Gil et al. “The Cryogenic Pumping Section of the KATRIN Experiment”. In: *IEEE Transactions on Applied Superconductivity* 20.3 (2010), pp. 316–319. ISSN: 1051-8223. DOI: `10.1109/TASC.2009.2038581`.

[48] F. Harms. *Characerization and Minimization of Background Processes in the KATRIN Main Spectrometer: PhD thesis*. Karlsruhe Institute of Technology KIT, 2015.

[49] G. Beamson, H. Q. Porter, and D. W. Turner. “The collimating and magnifying properties of a superconducting field photoelectron spectrometer”. In: *Journal of Physics E: Scientific Instruments* 14.2 (1981), p. 256. ISSN: 00223735. DOI: `10.1088/0022-3735/14/2/526`.

[50] F. Fränkle. *Background Investigations of the KATRIN Pre-Spectrometer: PhD thesis*. Karlsruhe Institute of Technology KIT, 2010.

[51] F. Fränkle. *Background overview*. Munich, 17.07.2018.

[52] B. Leiber. “Investigation of background due to secondary electron emission in the KATRIN-experiment”. PhD thesis. Karlsruhe Insitiute of Technology, 2014.

[53] P. Rovedo. “Muon induced secondary electrons at the KATRIN experiment: Detector installation and setup & data analysis”. Diploma thesis. Karlsruhe Insitiute of Technology, 2013.

[54] J. Linek. *Investigation of the muon induced background at the KATRIN main spectrometer: Master’s Thesis*. Karlsruhe Institute of Technology KIT, 2015.

[55] J. Oertlin. *Analysis of Radon-Induced Background during First Measurements at the KATRIN Main Spectrometer: Master’s thesis*. Karlsruhe Institute of Technology KIT, 2014.

[56] F. M. Fränkle et al. “Penning discharge in the KATRIN pre-spectrometer”. In: *Journal of Instrumentation* 9.07 (2014), P07028–P07028. DOI: `10.1088/1748-0221/9/07/P07028`.

[57] *BOREXINO Homepage: BORon solar neutrino EXperiment*. URL: `http://borex.lngs.infn.it/`.

[58] G. Zuzel and M. Wójcik. “Removal of the long-lived 222Rn daughters from copper and stainless steel surfaces”. In: *Nuclear Instruments and Methods in Physics Research Section A: Accelerators, Spectrometers, Detectors and Associated Equipment* 676 (2012), pp. 140–148. ISSN: 01689002. DOI: `10.1016/j.nima.2011.12.043`.

[59] M. Wójcik and G. Zuzel. “226Ra, 210Pb, 210Bi and 210Po deposition and removal from surfaces and liquids”. In: *Journal of radioanalytical and nuclear chemistry* 296.2 (2013), pp. 639–645. ISSN: 0236-5731. DOI: `10.1007/s10967-012-2180-5`.

[60] F. M. Fraenkle and KATRIN collaboration. “Background processes in the KATRIN main spectrometer”. In: *Journal of Physics: Conference Series* 888 (2017), p. 012070. ISSN: 1742-6588. DOI: `10.1088/1742-6596/888/1/012070`.

[61] F. M. Fränkle et al. “Radon induced background processes in the KATRIN pre-spectrometer”. In: *Astroparticle Physics* 35.3 (2011), pp. 128–134. ISSN: 09276505. DOI: `10.1016/j.astropartphys.2011.06.009`.

[62] N. Wandkowsky et al. “Validation of a model for radon-induced background processes in electrostatic spectrometers”. In: *Journal of Physics G: Nuclear and Particle Physics* 40.8 (2013), p. 085102. ISSN: 0954-3899. DOI: `10.1088/0954-3899/40/8/085102`.

[63] S. Görhardt. “Background Reduction Methods and Vacuum Technology at the KATRIN Spectrometers”. PhD thesis. Karlsruhe Insitiute of Technology, 2014.

[64] ThaLibster. *Decay chain of Uranium-238: Adapted and remixed from source code by User: BatesIsBack*. 2017. URL: `https://commons.wikimedia.org/wiki/File:Decay_Chain_of_Uranium-238.svg`.

[65] National Nuclear Data Center. *NuDat (Nuclear Structure and Decay Data)*. Ed. by Brookhaven National Laboratory. 2015. URL: `http://www.nndc.bnl.gov/nudat2/`.

[66] F. Block. *Characteristaion of the Background in the KATRIN Experiment: Master’s Thesis*. Karlsruhe Institute of Technology KIT, 2017.

[67] A. Müller. *Investigation of the secondary electron emission characteristics of the KATRIN main spectrometer: Master’s thesis*. Karlsruhe Institute of Technology KIT, 2016.

[68] A. Pollithy. *Rydberg Analysis - Status*. Karlsruhe, 24.11.2017.

[69] A. Pollithy. *Characterizing the residual background in KATRIN*. 19.02.2018.

[70] T F Gallagher. “Rydberg atoms”. In: *Reports on Progress in Physics* 51.2 (1988), p. 143. URL: `http://stacks.iop.org/0034-4885/51/i=2/a=001`.

[71] Thomas F. Gallagher. *Rydberg Atoms*. Cambridge: Cambridge University Press, 1994. ISBN: 9780511524530. DOI: `10.1017/CBO9780511524530`.

[72] I. Martinson and L. J. Curtis. “Janne Rydberg – his life and work”. In: *Nuclear Instruments and Methods in Physics Research Section B: Beam Interactions with Materials and Atoms* 235.1-4 (2005), pp. 17–22. ISSN: 0168583X. DOI: `10.1016/j.nimb.2005.03.137`.

[73] Ingolf V. Hertel and Claus-Peter Schulz. *Atoms, Molecules and Optical Physics 1.* Berlin, Heidelberg: Springer Berlin Heidelberg, 2015. ISBN: 978-3-642-54321-0. DOI: `10.1007/978-3-642-54322-7`.

[74] Gordon Drake, ed. *Springer Handbook of Atomic, Molecular, and Optical Physics.* New York, NY: Springer Science+Business Media Inc, 2006. ISBN: 0-387-20802-X. DOI: `10.1007/978-0-387-26308-3`. URL: `http://site.ebrary.com/lib/alltitles/docDetail.action?docID=10228967`.

[75] Hans A. Bethe and Edwin E. Salpeter. *Quantum Mechanics of One- and Two-Electron Atoms.* Berlin, Heidelberg: Springer Berlin Heidelberg, 1957. ISBN: 978-3-662-12871-8. DOI: `10.1007/978-3-662-12869-5`.

[76] Peter Sigmund. "Theory of Sputtering. I. Sputtering Yield of Amorphous and Polycrystalline Targets". In: *Physical Review* 184.2 (1969), pp. 383–416. ISSN: 0031-899X. DOI: `10.1103/PhysRev.184.383`.

[77] R. Behrisch and W. Eckstein. *Sputtering by Particle Bombardment: Experiments and Computer Calculations from Treshold to MeV Energies.* Vol. 110. Topics in Applied Physics. Berlin, Heidelberg: Springer Berlin Heidelberg, 2007. ISBN: 978-3-540-44500-5. DOI: `10.1007/978-3-540-44502-9`.

[78] Roger Kelly. "On the origin of sputtered excited atoms". In: *Nuclear Instruments and Methods in Physics Research* 194.1-3 (1982), pp. 583–588. ISSN: 01675087. DOI: `10.1016/0029-554X(82)90585-7`.

[79] G. Falcone, D. Matragrano, and A. Oliva. "Energy distribution of sputtered excited atoms". In: *Lettere al Nuovo Cimento (1971-1985)* 35.16 (1982), pp. 465–468. ISSN: 1827-613X. DOI: `10.1007/BF02817286`.

[80] A. Wucher et al. "Detection of sputtered metastable atoms by autoionization". In: *Physical Review A* 49.3 (1994), pp. 2188–2190. ISSN: 1050-2947. DOI: `10.1103/PhysRevA.49.2188`.

[81] Fränkle. F. *Th-228 source measurements: SDS3 measurements - status and outlook.* Karlsruhe, 7.03.2016.

[82] Karl Heinz Krebs. "Electron Ejection from Solids by Atomic Particles with Kinetic Energy". In: *Fortschritte der Physik* 16.8 (1968), pp. 419–490. ISSN: 00158208. DOI: `10.1002/prop.19680160802`.

[83] R. Kelly. "Bombardment-induced compositional change with alloys, oxides, oxysalts, and halides". In: *Nuclear Instruments and Methods in Physics Research Section B: Beam Interactions with Materials and Atoms* 39.1-4 (1989), pp. 43–56. ISSN: 0168583X. DOI: `10.1016/0168-583X(89)90739-8`.

[84] M. W. Thompson, B. W. Farmery, and P. A. Newson. "I. A mechanical spectrometer for analysing the energy distribution of sputtered atoms of copper or gold". In: *Philosophical Magazine* 18.152 (1968), pp. 361–376. ISSN: 0031-8086. DOI: `10.1080/14786436808227357`.

[85] M. W. Thompson. “II. The energy spectrum of ejected atoms during the high energy sputtering of gold”. In: *Philosophical Magazine* 18.152 (1968), pp. 377–414. ISSN: 0031-8086. DOI: `10.1080/14786436808227358`.

[86] B. W. Farmery and M. W. Thompson. “III. Energy spectra for copper”. In: *Philosophical Magazine* 18.152 (1968), pp. 415–424. ISSN: 0031-8086. DOI: `10.1080/14786436808227359`.

[87] J. Bohdansky. “Important sputtering yield data for tokamaks: A comparison of measurements and estimates”. In: *Journal of Nuclear Materials* 93-94 (1980), pp. 44–60. ISSN: 00223115. DOI: `10.1016/0022-3115(80)90302-5`.

[88] G. E. Chapman et al. “The energy distribution of sputtered atoms from gold”. In: *Radiation Effects* 13.1-2 (1972), pp. 121–129. ISSN: 0033-7579. DOI: `10.1080/00337577208231169`.

[89] P. Sigmund, H. M. Urbassek, and D. Matragrano. “A note on rotational and vibrational motion of sputtered or desorbed diatomic molecules”. In: *Nuclear Instruments and Methods in Physics Research Section B: Beam Interactions with Materials and Atoms* 14.4-6 (1986), pp. 495–499. ISSN: 0168583X. DOI: `10.1016/0168-583X(86)90145-X`.

[90] H. M. Urbassek. “Sputtering of molecules”. In: *Nuclear Instruments and Methods in Physics Research Section B: Beam Interactions with Materials and Atoms* 18.1-6 (1986), pp. 587–595. ISSN: 0168583X. DOI: `10.1016/S0168-583X(86)80093-3`.

[91] A. E. de Vries. “Sputtering of molecules and clusters”. In: *Nuclear Instruments and Methods in Physics Research Section B: Beam Interactions with Materials and Atoms* 27.1 (1987), pp. 173–180. ISSN: 0168583X. DOI: `10.1016/0168-583X(87)90018-8`.

[92] Gerhard Betz and Karl Wien. “Energy and angular distributions of sputtered particles”. In: 140 (1994), pp. 1–110.

[93] Steven Dzioba, Orlando Auciello, and Roger Kelly. “On the kinetic energies of sputtered excited particles, I. Atoms sputtered from Li, LiF, and NaCl”. In: *Radiation Effects* 45.3-4 (1980), pp. 235–245. ISSN: 0033-7579. DOI: `10.1080/00337578008208435`.

[94] Roger Kelly. “Statistical model for the formation of excited atoms in the sputtering process”. In: *Physical Review B* 25.2 (1982), pp. 700–712. ISSN: 0163-1829. DOI: `10.1103/PhysRevB.25.700`.

[95] G. Betz. “Electronic excitation in sputtered atoms and the oxygen effect”. In: *Nuclear Instruments and Methods in Physics Research Section B: Beam Interactions with Materials and Atoms* 27.1 (1987), pp. 104–118. ISSN: 0168583X. DOI: `10.1016/0168-583X(87)90011-5`.

[96] V. G. Drobnich, V. A. Mastyugin, and S. S. Pop. “Investigation of angular and energy distributions of excited sputtered and scattered particles by using a Doppler method”. In: *Nuclear Instruments and Methods in Physics Research Section B: Beam Interactions with Materials and Atoms* 58.3-4 (1991), pp. 443–447. ISSN: 0168583X. DOI: `10.1016/0168-583X(91)95883-F`.

[97] B. Schweer and H. L. Bay. “On the velocity distribution of excited Fe-atoms by sputtering of iron”. In: *Applied Physics A* 29.2 (1982), pp. 53–55. ISSN: 1432-0630. DOI: `10.1007/BF00632425`.

[98] O. Auciello. “Determination of excited sputtered atoms kinetic energy as a contribution to the understanding of the excitation phenomenon in the sputtering process”. In: *Nuclear Instruments and Methods in Physics Research* 194.1-3 (1982), pp. 549–553. ISSN: 01675087. DOI: `10.1016/0029-554X(82)90579-1`.

[99] G. Falcone and F. Piperno. “Kinematics of sputtered excited atoms”. In: *Surface Science* 365.2 (1996), pp. 511–516. ISSN: 00396028. DOI: `10.1016/0039-6028(96)00715-7`.

[100] V. M. Konoplev, M. Vicanek, and A. Gras-Martí. “Note on the spectra of excited particles in sputtering from collision cascades”. In: *Nuclear Instruments and Methods in Physics Research Section B: Beam Interactions with Materials and Atoms* 67.1-4 (1992), pp. 574–579. ISSN: 0168583X. DOI: `10.1016/0168-583X(92)95876-S`.

[101] A. Wucher and Z. Sroubek. “Formation of metastable excited states during sputtering of transition metals”. In: *Physical Review B* 55.2 (1997), pp. 780–786. ISSN: 0163-1829. DOI: `10.1103/PhysRevB.55.780`.

[102] Friedrich Aumayr and Hannspeter Winter. “Potential sputtering”. In: *Philosophical transactions. Series A, Mathematical, physical, and engineering sciences* 362.1814 (2004), pp. 77–102. ISSN: 1364-503X. DOI: `10.1098/rsta.2003.1300`.

[103] R. Taranko and E. Taranko. “Resonant electron transfer in ion/atom–metal surface interactions within generalized Anderson–Newns model”. In: *Vacuum* 54.1-4 (1999), pp. 161–165. ISSN: 0042207X. DOI: `10.1016/S0042-207X(98)00453-9`.

[104] J. Los and J.J.C Geerlings. “Charge exchange in atom-surface collisions”. In: *Physics Reports* 190.3 (1990), pp. 133–190. ISSN: 03701573. DOI: `10.1016/0370-1573(90)90104-A`.

[105] R. Carmina Monreal. “Auger neutralization and ionization processes for charge exchange between slow noble gas atoms and solid surfaces”. In: *Progress in Surface Science* 89.1 (2014), pp. 80–125. ISSN: 00796816. DOI: `10.1016/j.progsurf.2014.01.001`. URL: `http://arxiv.org/pdf/1402.2080v1`.

[106] Ryoichi Kawai and Yoshi-Hiko Ohtsuki. “Resonant neutralization of ions scattered from surfaces with an intermediate velocity”. In: *Nuclear Instruments and Methods in Physics Research Section B: Beam Interactions with Materials and Atoms* 13.1-3 (1986), pp. 605–608. ISSN: 0168583X. DOI: `10.1016/0168-583X(86)90575-6`.

[107] M. A. Cazalilla et al. “Theory of Auger neutralization and deexcitation of slow ions at metal surfaces”. In: *Physical Review B* 58.20 (1998), pp. 13991–14006. ISSN: 0163-1829. DOI: `10.1103/PhysRevB.58.13991`.

[108] Mike W. Kohlhoff. “Interaction of Rydberg atoms with surfaces”. In: *The European Physical Journal Special Topics* 225.15-16 (2016), pp. 3061–3085. ISSN: 1951-6355. DOI: `10.1140/epjst/e2016-60018-x`.

[109] J. F. Ziegler, J. P. Biersack, and M. D. Ziegler. *SRIM - The Stopping and Range of Ions in Matter.* 1985.

[110] J. F. Ziegler, M. D. Ziegler, and J. P. Biersack. *www.SRIM.org: SRIM - The Stopping and Range of Ions in Matter.*

[111] James F. Ziegler, M. D. Ziegler, and J. P. Biersack. "SRIM – The stopping and range of ions in matter". In: *Nuclear Instruments and Methods in Physics Research Section B: Beam Interactions with Materials and Atoms* 268.11-12 (2010), pp. 1818–1823. ISSN: 0168583X. DOI: `10.1016/j.nimb.2010.02.091`.

[112] J. P. Biersack and W. Eckstein. "Sputtering studies with the Monte Carlo Program TRIM.SP". In: *Applied Physics A* 34.2 (1984), pp. 73–94. ISSN: 1432-0630. DOI: `10.1007/BF00614759`.

[113] Herbert Goldstein, Charles P. Poole, and John L. Safko. *Classical mechanics.* 3. ed. San Francisco, NJ: Addison Wesley, 2002. ISBN: 0201657023.

[114] MAN DWE GmbH. *DESIGN REPORT: UHV Main spectrometer for KATRIN at Forschungszentrum Karlsruhe.* 30.06.2005.

[115] MAN DWE GmbH. *"KATRIN" Vacuum Vessel: part list.* 7.06.2005.

[116] *Flacherzeugnisse aus Druckbehälterstählen - Teil 7: Nichtrostende Stähle.* October 2016.

[117] Shuo-Jen Lee and Jian-Jang Lai. "The effects of electropolishing (EP) process parameters on corrosion resistance of 316L stainless steel". In: *Journal of Materials Processing Technology* 140.1-3 (2003), pp. 206–210. ISSN: 09240136. DOI: `10.1016/S0924-0136(03)00785-4`.

[118] S. Trigwell and G. Selvaduray. *Effect of Surface Treatment on the Surface Characteristics of AISI 316L Stainless Steel.* Ed. by NASA Kennedy Space Center. 2005.

[119] Krzysztof Rokosz et al. "XPS depth profiling analysis of passive surface layers formed on austenitic AISI 304L and AISI 316L SS after high-current-density electropolishing". In: *Surface and Coatings Technology* 276 (2015), pp. 516–520. ISSN: 02578972. DOI: `10.1016/j.surfcoat.2015.06.022`.

[120] P. J. Núñez et al. "Characterization of Surface Finish of Electropolished Stainless Steel AISI 316L with Varying Electrolyte Concentrations". In: *Procedia Engineering* 63 (2013), pp. 771–778. ISSN: 18777058. DOI: `10.1016/j.proeng.2013.08.255`.

[121] Tadeusz Hryniewicz, Krzysztof Rokosz, and Massimiliano Filippi. "Biomaterial Studies on AISI 316L Stainless Steel after Magnetoelectropolishing". In: *Materials* 2.1 (2009), pp. 129–145. DOI: `10.3390/ma2010129`.

[122] S. J. Kerber and J. Tverberg. *Stainless Steel Surface Analysis: AES and XPS analysis of the passivation layer on stainless steel can help determine how well it will resist corrosion.* 2000.

[123] Deutsche Derustit GmbH. *Sicherheitsdatenblatt (91/155/EWG): DERUSTIT - Elektrolyt CN 18 A.* 10.02.2003.

[124] Deutsche Derustit GmbH. *Sicherheitsdatenblatt (93/112/EG): DERUSTIT - Dekapierlösung CN 15.* 11.02.2003.

[125] Deutsche Derustit GmbH. *DERUSTIT Elektropolishing Process/Documentation: QS-Plan DWE Katrin.* 2006.

[126] A. Osipowicz. *SRIM Simulations on alpha recoil nuclei in the main spectrometer.* Karlsruhe, 7.03.2016.

[127] I. I. Beterov et al. "Ionization of Rydberg atoms by blackbody radiation". In: *New Journal of Physics* 11.1 (2009), p. 013052. DOI: `10.1088/1367-2630/11/1/013052`.

[128] N. Trost. "Modeling and measurement of Rydberg-State mediated Background at the KATRIN Main Spectrometer". PhD thesis. Karlsruhe Institute of Technology KIT, 2018.

[129] M. J. Shaw. "Penning ionization". In: *Contemporary Physics* 15.5 (1974), pp. 445–464. ISSN: 0010-7514. DOI: `10.1080/00107517408210804`.

[130] F. M. Penning. "Über Ionisation durch metastabile Atome". In: *Die Naturwissenschaften* 15.40 (1927), p. 818. ISSN: 0028-1042. DOI: `10.1007/BF01505431`.

[131] Kanji Katsuura. "Ionization of Atoms by Collision with Excited Atoms". In: *Physical Review* 42.11 (1965), pp. 3771–3775. ISSN: 0031-899X. DOI: `10.1063/1.1695814`.

[132] H. Hotop et al. "Penning electron spectra from ionization of hydrogen atoms by He(2^1S) and He(2^3S) metastables". In: *The Journal of Chemical Physics* 10.5 (1971), pp. 493–497. ISSN: 0009-2614. DOI: `10.1016/0009-2614(71)87021-5`.

[133] H Morgner and A Niehaus. "Experimental and theoretical study of the Penning ionisation of H atoms by He metastables". In: *Journal of Physics B: Atomic and Molecular Physics* 12.11 (1979), p. 1805. URL: `http://stacks.iop.org/0022-3700/12/i=11/a=008`.

[134] A A Mihajlov and R K Janev. "Ionisation in atom-Rydberg atom collisions: ejected electron energy spectra and reaction rate coefficients". In: *Journal of Physics B: Atomic and Molecular Physics* 14.10 (1981), p. 1639. URL: `http://stacks.iop.org/0022-3700/14/i=10/a=013`.

[135] Dumont M. Jones and John S. Dahler. "Theory of associative ionization". In: *Physical Review A* 37.8 (1988), pp. 2916–2933. ISSN: 1050-2947. DOI: `10.1103/PhysRevA.37.2916`.

[136] A. Merz et al. "Experimental and theoretical studies of simple attractive Penning ionization systems". In: *Chemical Physics* 145.2 (1990), pp. 219–238. ISSN: 03010104. DOI: `10.1016/0301-0104(90)89117-9`.

[137] K.-D. Heber et al. "Long-range interactions in planetary three-body Coulomb systems". In: *Physical Review A* 56.2 (1997), pp. 1255–1267. ISSN: 1050-2947. DOI: `10.1103/PhysRevA.56.1255`.

[138] M. R. Flannery, D. Vrinceanu, and V. N. Ostrovsky. "Long-range interaction between polar Rydberg atoms". In: *Journal of Physics B: Atomic, Molecular and Optical Physics* 38.2 (2005), S279–S293. ISSN: 0953-4075. DOI: `10.1088/0953-4075/38/2/020`.

[139] Martin Kiffner et al. "Quantum mechanical calculation of Rydberg–Rydberg autoionization rates". In: *Journal of Physics B: Atomic, Molecular and Optical Physics* 49.20 (2016), p. 204004. ISSN: 0953-4075. DOI: `10.1088/0953-4075/49/20/204004`.

[140] R. E. Olson. "Ionization Cross Sections for Rydberg-Atom-Rydberg-Atom Collisions". In: *Physical review letters* 43.2 (1979), pp. 126–129. ISSN: 0031-9007. DOI: `10.1103/PhysRevLett.43.126`.

[141] F. Robicheaux et al. "Simulation of coherent interactions between Rydberg atoms". In: *Physical Review A* 70.4 (2004), p. 460. ISSN: 1050-2947. DOI: `10.1103/PhysRevA.70.042703`.

[142] F. Robicheaux. "Ionization due to the interaction between two Rydberg atoms". In: *Journal of Physics B: Atomic, Molecular and Optical Physics* 38.2 (2005), S333–S342. ISSN: 0953-4075. DOI: `10.1088/0953-4075/38/2/024`.

[143] S. Gerlach. "Dipol-Dipol Wechselwirkungen ultrakalter Helium Rydbergatome". PhD thesis. Technische Universität Berlin, 2006.

[144] D. K. Efimov et al. "Strong enhancement of Penning ionization for asymmetric atom pairs in cold Rydberg gases: the Tom and Jerry effect". In: *Journal of Physics B: Atomic, Molecular and Optical Physics* 49.12 (2016), p. 125302. ISSN: 0953-4075. DOI: `10.1088/0953-4075/49/12/125302`.

[145] Sebastian Weber et al. "Calculation of Rydberg interaction potentials". In: *Journal of Physics B: Atomic, Molecular and Optical Physics* 50.13 (2017), p. 133001. ISSN: 0953-4075. DOI: `10.1088/1361-6455/aa743a`.

[146] T. L. Nguyen. "Study of dipole-dipole interaction between Rydberg atoms : toward quantum simulation with Rydberg atoms". PhD thesis. Paris: Universite Pierre et Marie Curie, 2016.

[147] Michael G. Littman, Michael M. Kash, and Daniel Kleppner. "Field-Ionization Processes in Excited Atoms". In: *Physical review letters* 41.2 (1978), pp. 103–107. ISSN: 0031-9007. DOI: `10.1103/PhysRevLett.41.103`.

[148] William A. Chupka. "Factors affecting lifetimes and resolution of Rydberg states observed in zero–electron–kinetic–energy spectroscopy". In: *The Journal of Chemical Physics* 98.6 (1993), pp. 4520–4530. ISSN: 0009-2614. DOI: `10.1063/1.465011`.

[149] V. Enss, V. Kostrykin, and R. Schrader. "Ionization of Rydberg atoms by an electric-field kick". In: *Physical Review A* 50.2 (1994), pp. 1578–1580. ISSN: 1050-2947. DOI: `10.1103/PhysRevA.50.1578`.

[150] F. Merkt and R. N. Zare. "On the lifetimes of Rydberg states probed by delayed pulsed field ionization". In: *The Journal of Chemical Physics* 101.5 (1994), pp. 3495–3505. ISSN: 0009-2614. DOI: `10.1063/1.467534`.

[151] Volker Enss and Vadim Kostrykin. "Ionization of Rydberg Atoms by a Stark Kick". In: (1996).

[152] K. Ganesan and R. Gębarowski. "Chaos in the hydrogen atom interacting with external fields". In: *Pramana* 48.2 (1997), pp. 379–410. ISSN: 0304-4289. DOI: `10.1007/BF02845652`.

[153] M. Inarrea and J. P. Salas. “Rydberg hydrogen atom in the presence of uniform magnetic and quadrupolar electric fields”. In: *The European Physical Journal D - Atomic, Molecular and Optical Physics* 27.1 (2003), pp. 3–13. ISSN: 1434-6060. DOI: `10.1140/epjd/e2003-00233-3`.

[154] V. N. Ostrovsky and E. Horsdal-Pedersen. “The Rydberg atom in collinear static and harmonic electric fields”. In: *The European Physical Journal D - Atomic, Molecular and Optical Physics* 23.1 (2003), pp. 15–24. ISSN: 1434-6060. DOI: `10.1140/epjd/e2003-00007-y`.

[155] J. M. Menéndez, I. Martín, and A. M. Velasco. “The Stark effect in atomic Rydberg states through a quantum defect approach”. In: *International Journal of Quantum Chemistry* 102.5 (2005), pp. 956–960. ISSN: 00207608. DOI: `10.1002/qua.20461`.

[156] Lutz Fechner. “High resolution experiments on strong-field ionization of atoms and molecules: test of tunneling theory, the role of doubly excited states, and channel-selective electron spectra”. Heidelberg University Library. 2014. DOI: `10.11588/heidok.00017715`.

[157] B. C. Yang and F. Robicheaux. “Field-ionization threshold and its induced ionization-window phenomenon for Rydberg atoms in a short single-cycle pulse”. In: *Physical Review A* 90.6 (2014), p. 1307. ISSN: 1050-2947. DOI: `10.1103/PhysRevA.90.063413`. URL: `http://arxiv.org/pdf/1410.0970v2`.

[158] A. Blom. “Exact solution of the Zeeman effect in single-electron systems”. In: *Physica Scripta* T120 (2005), pp. 90–98. ISSN: 0031-8949. DOI: `10.1088/0031-8949/2005/T120/014`. URL: `http://arxiv.org/pdf/physics/0406141v1`.

[159] V. S. Popov, B. M. Karnakov, and V. D. Mur. “Lorentz ionization of atoms in a strong magnetic field”. In: *Journal of Experimental and Theoretical Physics* 88.5 (1999), pp. 902–912. ISSN: 1090-6509. DOI: `10.1134/1.558870`.

[160] Bin He, Jian-Guo Wang, and Chun-Lei Liu. “Classical trajectory Monte Carlo investigation for Lorentz ionization of H(^{1}s)”. In: *Chinese Physics B* 22.7 (2013), p. 073101. ISSN: 1674-1056. DOI: `10.1088/1674-1056/22/7/073101`.

[161] Aibassov Erkin Zhakenovich et al. “Effect of Magnetic Field on the Ionization Potential of the Atoms and Ions”. In: *Journal of Chemistry and Chemical Engineering* 9.4 (2015). ISSN: 19347375. DOI: `10.17265/1934-7375/2015.04.009`.

[162] M. Fauth, H. Walther, and E. Werner. “Rydberg atoms in crossed external magnetic and electric fields: Experimental observation of an outer potential minimum”. In: *The European Physical Journal D - Atomic, Molecular and Optical Physics* 7.3 (1987), pp. 293–296. ISSN: 1434-6060. DOI: `10.1007/BF01384997`.

[163] V. S. Popov, B. M. Karnakov, and V. D. Mur. “Ionization of atoms in electric and magnetic fields and the imaginary time method”. In: *Journal of Experimental and Theoretical Physics* 86.5 (1998), pp. 860–874. ISSN: 1090-6509. DOI: `10.1134/1.558557`.

[164] Nils Berglund and Turgay Uzer. “The averaged dynamics of the hydrogen atom in crossed electric and magnetic fields as a perturbed Kepler problem”. In: *Foundations of Physics* 31.2 (2001), pp. 283–326. ISSN: 00159018. DOI: `10.1023/A:1017542620404`.

[165] T. Bartsch. “The hydrogen atom in an electric field and in crossed electric and magnetic fields: Closed-orbit theory and semiclassiscal quantization”. PhD thesis. Universität Stuttgart, 2002.

[166] E. Oks. “Circular Rydberg states of hydrogenlike systems in collinear electric and magnetic fields of arbitrary strengths: an exact analytical classical solution”. In: *The European Physical Journal D - Atomic, Molecular and Optical Physics* 28.2 (2004), pp. 171–179. ISSN: 1434-6060. DOI: `10.1140/epjd/e2003-00308-1`.

[167] Ferenc Gluck. “AXISYMMETRIC ELECTRIC FIELD CALCULATION WITH ZONAL HARMONIC EXPANSION”. In: *Progress In Electromagnetics Research B* 32 (2011), pp. 319–350. DOI: `10.2528/PIERB11042106`.

[168] Jacques E. Collin. “Autoionization in atomic and molecular physics”. In: *Endeavour* 1.3-4 (1977), pp. 122–128. ISSN: 01609327. DOI: `10.1016/0160-9327(77)90170-3`.

[169] T. Jahnke. “Interatomic and intermolecular Coulombic decay: the coming of age story”. In: *Journal of Physics B: Atomic, Molecular and Optical Physics* 48.8 (2015), p. 082001. ISSN: 0953-4075. DOI: `10.1088/0953-4075/48/8/082001`.

[170] S. Barth et al. “Observation of resonant interatomic coulombic decay in Ne clusters”. In: *The Journal of Chemical Physics* 122.24 (2005), p. 241102. ISSN: 0009-2614. DOI: `10.1063/1.1937395`.

[171] J. Titze et al. “Ionization dynamics of helium dimers in fast collisions with He^{++}”. In: *Physical review letters* 106.3 (2011), p. 033201. ISSN: 0031-9007. DOI: `10.1103/PhysRevLett.106.033201`.

[172] S. Scheit, L. S. Cederbaum, and H.-D. Meyer. “Time-dependent interplay between electron emission and fragmentation in the interatomic Coulombic decay”. In: *The Journal of Chemical Physics* 118.5 (2003), pp. 2092–2107. ISSN: 0009-2614. DOI: `10.1063/1.1531996`.

[173] T. Jahnke et al. “Ultrafast energy transfer between water molecules”. In: *Nature Physics* 6.2 (2010), pp. 139–142. ISSN: 1745-2473. DOI: `10.1038/NPHYS1498`.

[174] A. T. Wen et al. “Electron impact studies of autoionizing states in CO_2 using a multi-angle parallel detection electron spectrometer”. In: *Canadian Journal of Chemistry* 72.3 (1994), pp. 870–881. ISSN: 0008-4042. DOI: `10.1139/v94-114`.

[175] S. T. Pratt. “Vibrational autoionization in polyatomic molecules”. In: *Annual review of physical chemistry* 56 (2005), pp. 281–308. ISSN: 0066-426X. DOI: `10.1146/annurev.physchem.56.092503.141204`.

[176] A Corney and O M Williams. “Measurement of the radiative lifetime of the $^1S_0$ metastable level of atomic oxygen”. In: *Journal of Physics B: Atomic and Molecular Physics* 5.3 (1972), p. 686. URL: `http://stacks.iop.org/0022-3700/5/i=3/a=035`.

[177] V. Čermák and J. Šrámek. "Electron spectroscopy of autoionizing states of oxygen atoms". In: *Journal of Electron Spectroscopy and Related Phenomena* 2.1 (1973), pp. 97–100. ISSN: 03682048. DOI: `10.1016/0368-2048(73)80051-9`.

[178] P. M. Dehmer, W. L. Luken, and W. A. Chupka. "Competition between autoionization and radiative emission in the decay of excited states of the oxygen atom". In: *International Journal of Quantum Chemistry* 67.1 (1977), pp. 195–203. ISSN: 00207608. DOI: `10.1063/1.434518`.

[179] M. E. Rudd and Kenneth Smith. "Energy Spectra of Auto-Ionizing Electrons in Oxygen". In: *Physical Review* 169.1 (1968), pp. 79–84. ISSN: 0031-899X. DOI: `10.1103/PhysRev.169.79`.

[180] A A Wills, A A Cafolla, and J Comer. "The production of autoionizing states of atomic oxygen by the photodissociation of O_2". In: *Journal of Physics B: Atomic, Molecular and Optical Physics* 24.18 (1991), p. 3989. ISSN: 0953-4075. URL: `http://stacks.iop.org/0953-4075/24/i=18/a=013`.

[181] James A.R. Samson and V. E. Petrosky. "Partially autoionizing states of atomic oxygen". In: *Journal of Electron Spectroscopy and Related Phenomena* 3.6 (1974), pp. 461–465. ISSN: 03682048. DOI: `10.1016/0368-2048(74)80033-2`.

[182] Renaud Guillemin, Marc Simon, and Eiji Shigemasa. "Doppler effect in fragment autoionization following core-to-valence excitation in O_2". In: *Physical Review A* 82.5 (2010). ISSN: 1050-2947. DOI: `10.1103/PhysRevA.82.051401`.

[183] S. T. Pratt, P. M. Dehmer, and J. L. Dehmer. "Photoionization of an autoionizing level of atomic oxygen". In: *Physical Review A* 43.1 (1991), pp. 282–286. ISSN: 1050-2947. DOI: `10.1103/PhysRevA.43.282`.

[184] Hugh P. Kelly and Akiva Ron. "Photoionization Cross Section of the Neutral Iron Atom". In: *Physical Review A* 5.1 (1972), pp. 168–176. ISSN: 1050-2947. DOI: `10.1103/PhysRevA.5.168`.

[185] E. F. Worden et al. "The ionization potential of neutral iron, Fe I, by multistep laser spectroscopy". In: *Journal of the Optical Society of America B* 1.2 (1984), p. 314. ISSN: 0740-3224. DOI: `10.1364/JOSAB.1.000314`.

[186] M. A. Bautista. "Atomic data from the Iron Project. XVI. Photoionization cross sections and oscillator strengths for Fe V". In: *Astronomy and Astrophysics Supplement Series* 119.1 (1996), pp. 105–110. ISSN: 0365-0138. DOI: `10.1051/aas:1996231`.

[187] T. Day Goodacre et al. "The identification of autoionizing states of atomic chromium for the resonance ionization laser ion source of the ISOLDE radioactive ion beam facility". In: *Spectrochimica Acta Part B: Atomic Spectroscopy* 129 (2017), pp. 58–63. ISSN: 05848547. DOI: `10.1016/j.sab.2017.01.001`.

[188] I. C. Percival. "Planetary atoms". In: *Proc. R. Soc. Lond. A.* 353 (1977), pp. 289–297.

[189] T. F. Gallagher. "Doubly excited states". In: *Journal of the Optical Society of America B* 4.5 (1987), p. 794. ISSN: 0740-3224. DOI: `10.1364/JOSAB.4.000794`.

[190] A. L. Belov and V. P. Krainov. "Classical autoionization of two-electron atoms". In: *Journal of Experimental and Theoretical Physics* 65.2 (1987), p. 257. ISSN: 1090-6509.

[191] K. Iemura et al. “Electron spectroscopy of doubly excited states in He produced by slow collisions of He^2+ ions with Ba atoms”. In: *Physical Review A* 64.6 (2001), p. 516. ISSN: 1050-2947. DOI: `10.1103/PhysRevA.64.062709`.

[192] V. N. Ostrovsky and N. V. Prudov. “Rydberg series of the planetary atom states”. In: *Journal of Physics B: Atomic, Molecular and Optical Physics* 26.11 (1993), pp. L263–L269. ISSN: 0953-4075. DOI: `10.1088/0953-4075/26/11/001`.

[193] K. Richter and D. Wintgen. “Calculations of planetary atom states”. In: *Journal of Physics B: Atomic, Molecular and Optical Physics* 24.23 (1991), pp. L565–L571. ISSN: 0953-4075. DOI: `10.1088/0953-4075/24/23/002`.

[194] Seng et al. “Electron Spectroscopy of Planetary Atoms”. In: *Physical review letters* 74.17 (1995), pp. 3344–3347. ISSN: 0031-9007. DOI: `10.1103/PhysRevLett.74.3344`.

[195] A. Burgers and D. Wintgen. “Inhibited autoionization of planetary atom states”. In: *Journal of Physics B: Atomic, Molecular and Optical Physics* 27.8 (1994), pp. L131–L135. ISSN: 0953-4075. DOI: `10.1088/0953-4075/27/8/001`.

[196] K. Blaum et al. *Test of Rydberg-emission from short lived 223-Ra-source, introduced into the MS through existing sluice: Update on approved Proposal.* 2018.

[197] H. Bateman. “The solution of differential equations occurring in the theory of radioactive transformations”. In: *Proc. Cambridge Philos. Soc* 15.V (1910), pp. 423–427.

[198] ThaLibster. *Decay chain of Thorium-232: Remixed from the version by User: BatesIsBack to include more color-coding and branching fractions.* 2017. URL: `https://commons.wikimedia.org/wiki/File:Decay_Chain_of_Thorium-232.svg`.

[199] E. Bonet. *Decay chain 4n+3: Actinium series.* 2013. URL: `https://commons.wikimedia.org/wiki/File:Decay_Chain_of_Actinium.svg`.

A. Appendix

A.1. Background measurement data sets

Table A.1.: Background measurements L, M, N and N2 at different inner electrode potentials. The magnetic field in the analyzing plane was 3.8 G. The pressure was $p < 1 \cdot 10^{-9}$ mbar in the spectrometer. The vessel potential was adjusted such that $U_0 = U_{\mathrm{vessel}} + U_{\mathrm{IE,common}} = -18.6\,\mathrm{kV}$. Even the steep cones ($U_{\mathrm{SC}}$ were different. Given rates correspond to the number of events within the ROI (25.72 keV – 30.72 keV).[48]

Data set	$U_{\mathrm{IE,common}}$ (V)	U_{SC} (V)	U_{PAE} (kV)	Rate (mcps)
L	0	0	+10	890 ± 5
M	-5	+2	+4	824 ± 1
	-10	+2	+10	789 ± 5
	-15	+2	+10	755 ± 6
	-20	+2	+10	729 ± 7
	-35	+2	+10	701 ± 12
	-50	+2	+10	643 ± 5
N	-100	+1	+10	620 ± 8
N2	-100	+97	+4	664 ± 1
	-200	+1	+10	587 ± 7
	-300	+1	+10	555 ± 7
	-400	+1	+10	545 ± 7
	-575	+2	+10	490 ± 12
	-800	+2	+10	517 ± 12

Table A.2.: Background measurements U and S at different UHV pressure levels in the spectrometer. Recorded with $U_{\mathrm{IE,common}} = -100\,\mathrm{V}$, $U_{\mathrm{SC}} = +1\,\mathrm{V}$, $U_{\mathrm{PAE}} = +10\,\mathrm{kV}$. Background rates correspond ti the number of events within the ROI. [48]

Data set	Pressure ($\cdot 10^{-10}$mbar)	B-field	Rate (mcps)
S	$14.9^{+0.6}_{-0.4}$	5 G	484 ± 8
U	$82.4^{+0.1}_{-0.1}$	5 G	614 ± 5

Table A.3.: Background measurements L,P and Q at different magnetic field settings during SDS-IIa. Carried out with cold baffles and spectrometer in its standard HV-mode.

Data set	Magn. field setting	$U_{\mathrm{IE,common}}$ (V)	Rate (mcps)
L	3.8 G	0	890 ± 5
P	5 G	0	645 ± 4
Q	9 G	0	349 ± 3

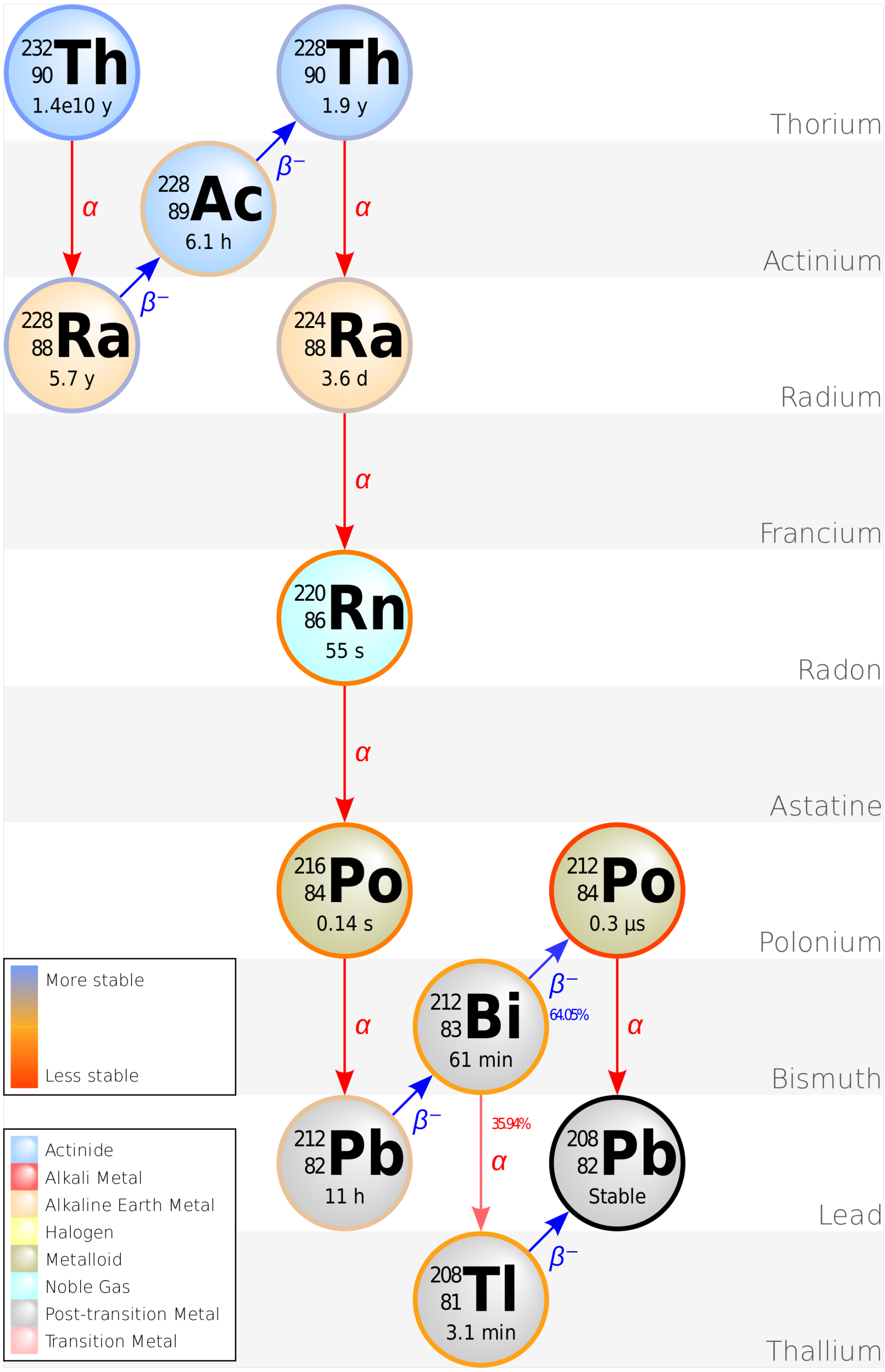

Figure A.1.: The 4n-chain of ^{232}Th. Commonly called the thorium series, beginning with thorium-232 and terminates with lead-208. Colored frame around the isotopes referres to their stability from dark blue to red, black indicates stable.[198]

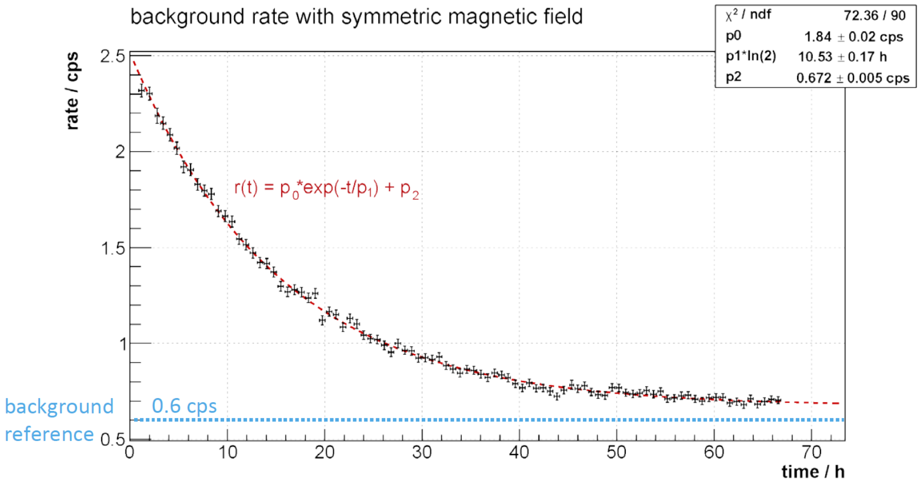

Figure A.2.: Background rate with symmetric magnetic field of the thorium measurements. Appended with a reference background of 0.6 cps.[81]

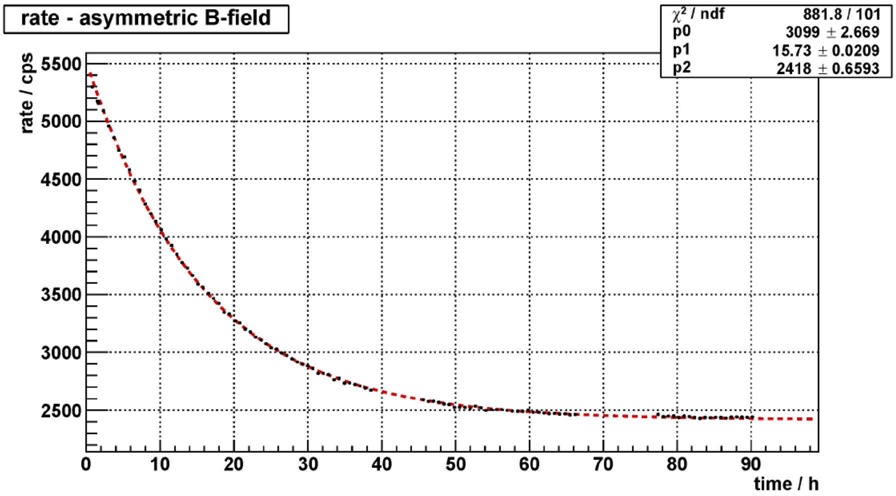

Figure A.3.: Background rate with asymmetric magnetic field of the thorium measurements. Due to the asymmetric magnetic field, more electrons from the wall are detected, resulting in a much higher rate in compared to the symmetric case.[51]

A.2. SRIM simulations

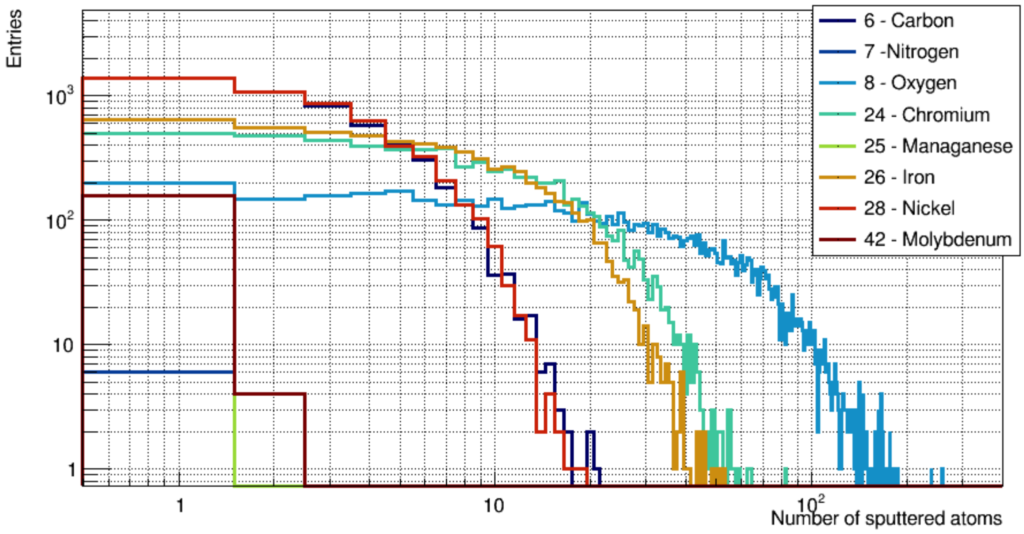

Figure A.4.: Number of sputtered atoms per chemical element. Not scaled to the initially number of Pb-ions.

Table A.4.: Fit results of the energy distribution sputtering yield with free U and m. For each element the fit parameters U and m are given and the theoretical surface binding energy, used in SRIM. The fits lead to calculated peak positions with eq. 3.3 and the mean m to $\overline{m} = 0.24512$

Element	$E_{\text{sub,theo}}$ (eV)	U (eV)	m	E_{peak} (eV)
O	2	1.346 ± 0.010	0.1436 ± 0.0017	0.786
Cr	4.12	2.538 ± 0.0039	0.2038 ± 0.0036	1.594
Fe	4.34	2.453 ± 0.046	0.2277 ± 0.0043	1.588
C	7.41	2.517 ± 0.104	0.3356 ± 0.0087	1.894
Ni	4.46	1.838 ± 0.070	0.3149 ± 0.0082	1.341

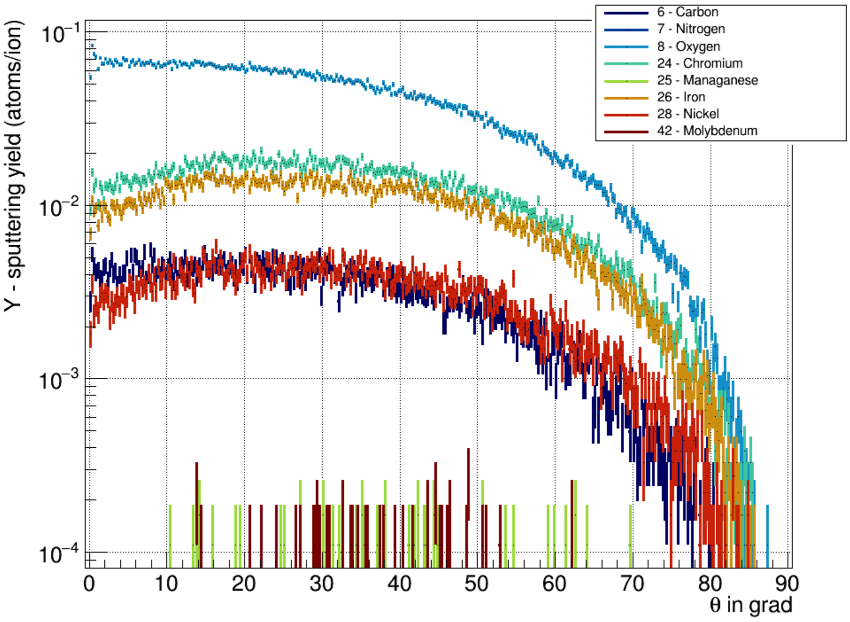

Figure A.5.: Polar angular distribution for each element.

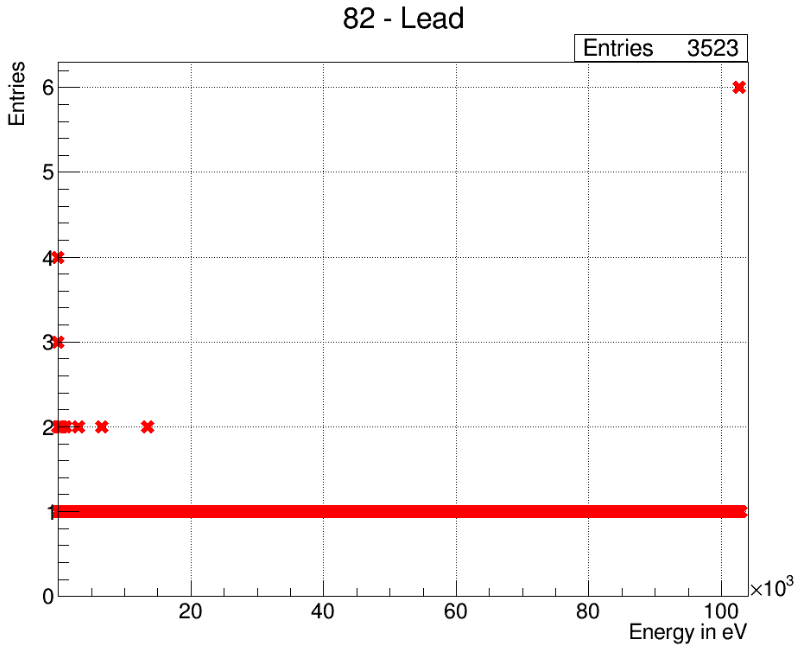

Figure A.6.: Unscaled Energy distribution of the transmitted ^{206}Pb-ions. Nearly uniformly distributed from 1 eV to 103 keV, with slighty higher rates at low energies.

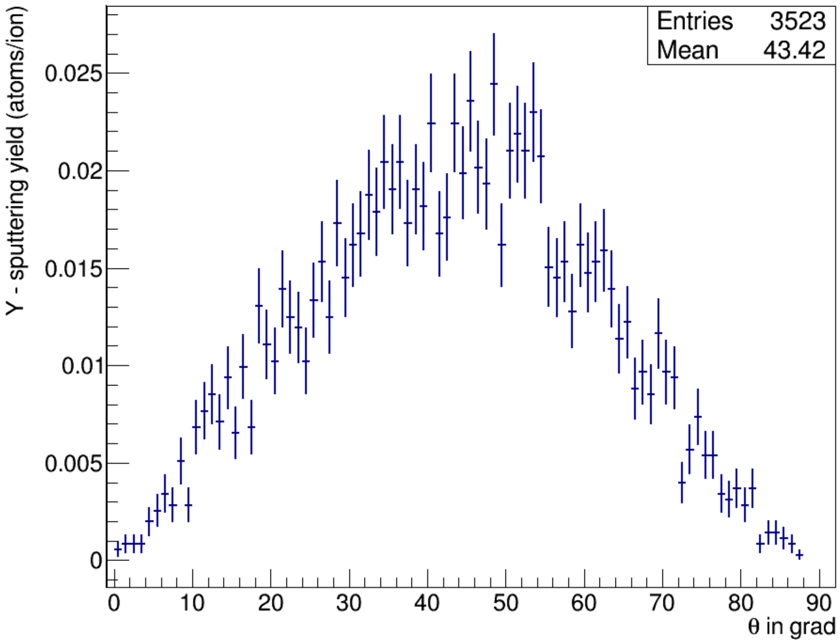

Figure A.7.: Polar angle distributions of the transmitted ^{206}Pb-ions. Clearly visible maximum at ≈ 45°.

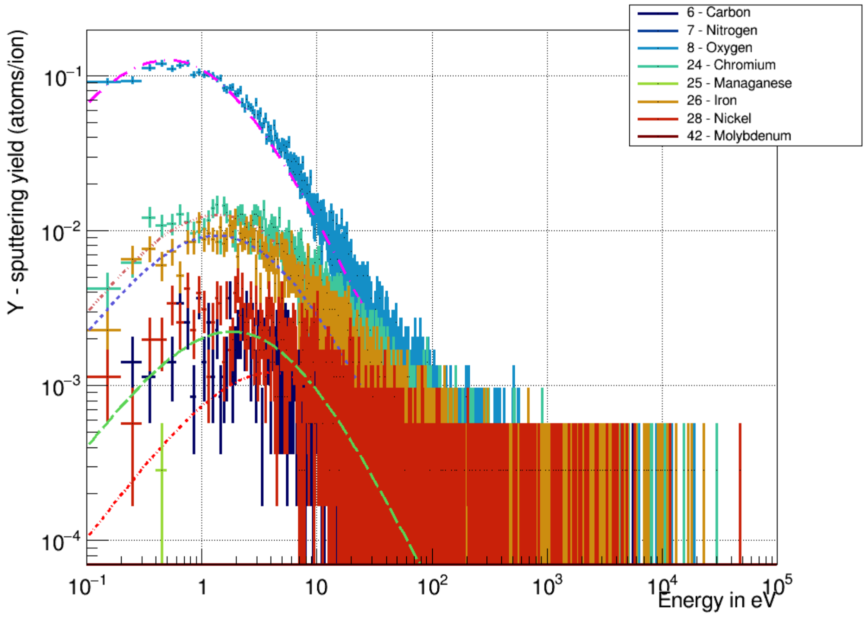

Figure A.8.: Scaled energy distribution of sputtered atoms caused by the transmitted ^{206}Pb-ions. Also fitted with the model function eq. 3.8, but the low rates, especially for nickel and carbon, deliver no good fits.

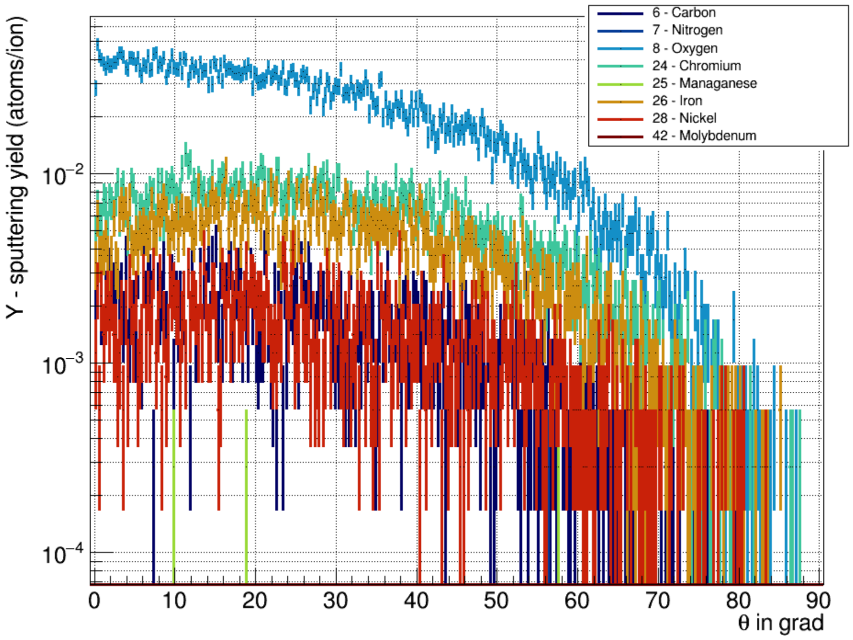

Figure A.9.: Scaled polar angular distribution of sputtered atoms caused by the transmitted Pb-ions.

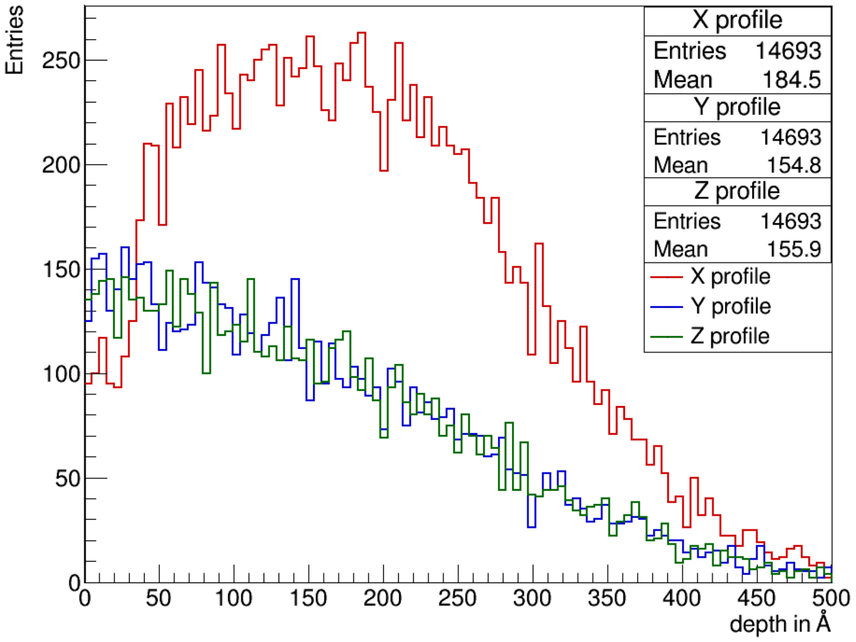

Figure A.10.: 1D histogram of the end positions of the stopped ^{206}Pb-ions. The X-profile corresponds to the depth (x-axis) of implantation is shown in red. The lateral profiles along y in blue and z in green, respectively.

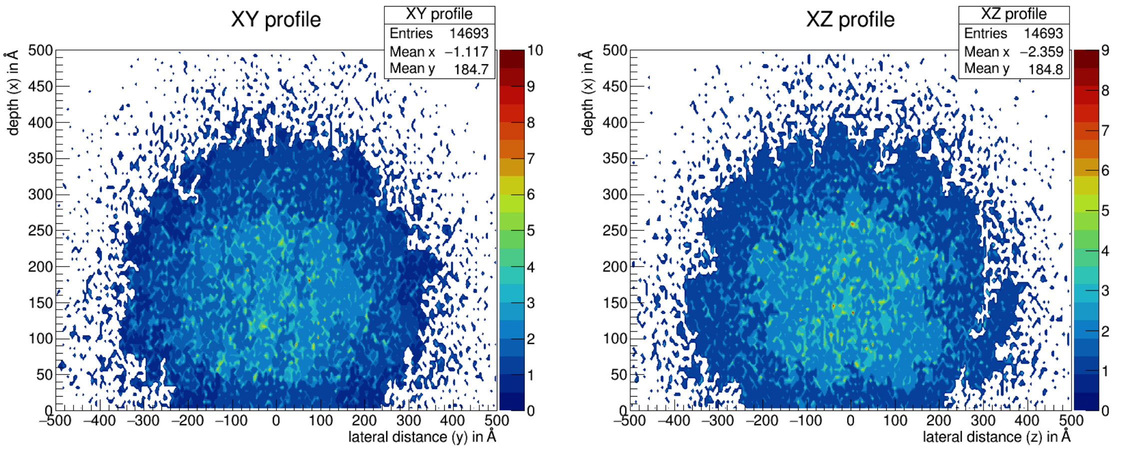

Figure A.11.: 2D profiles for the xy- and xz-plane of the stopped ^{206}Pb-ions. The color indicates the amount of particles.

A.3. Electric and magnetic fields

Table A.5.: Unit transformation from SI to atomic units

Dimension	Expression	Value (SI)
length	$\frac{4\pi\epsilon_0\hbar^2}{m_e e^2}$	$a_0 = 5.292 \cdot 10^{-11}$ m
energy	$\frac{m_e e^4}{(4\pi\epsilon_0\hbar)^2}$	$E_h = 27.211$ eV
time	$\frac{\hbar}{E_h}$	$2.419 \cdot 10^{-17}$ s
momentum	$\frac{\hbar}{a_0}$	$1.993 \cdot 10^{-24}$ kg · m · s^{-1}
force	$\frac{E_h}{a_0}$	$8.239 \cdot 10^{-8}$ N
electric field	$\frac{E_h}{e a_0}$	$5.142 \cdot 10^{11}$ V · m^{-1}
electric potential	$\frac{E_h}{e}$	27.211 V
magnetic field	$\frac{\hbar}{e a_0^2}$	$2.35 \cdot 10^{5}$ T

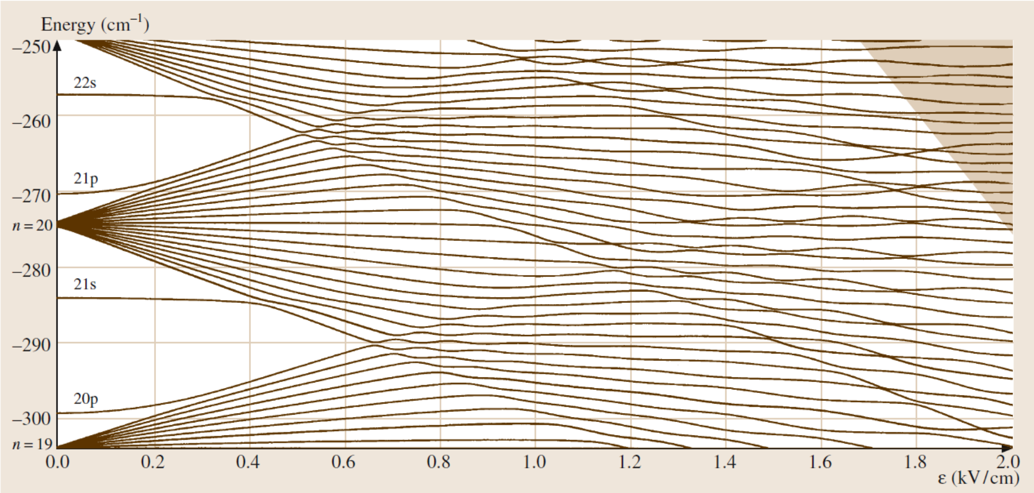

Figure A.12.: Energies of Na $m = 0$ levels of $n \approx 20$ as a function of electric field. The shaded region is above the classical ionization limit.[74]

A.3.1. Simulated electric field maps and along paths of various angle

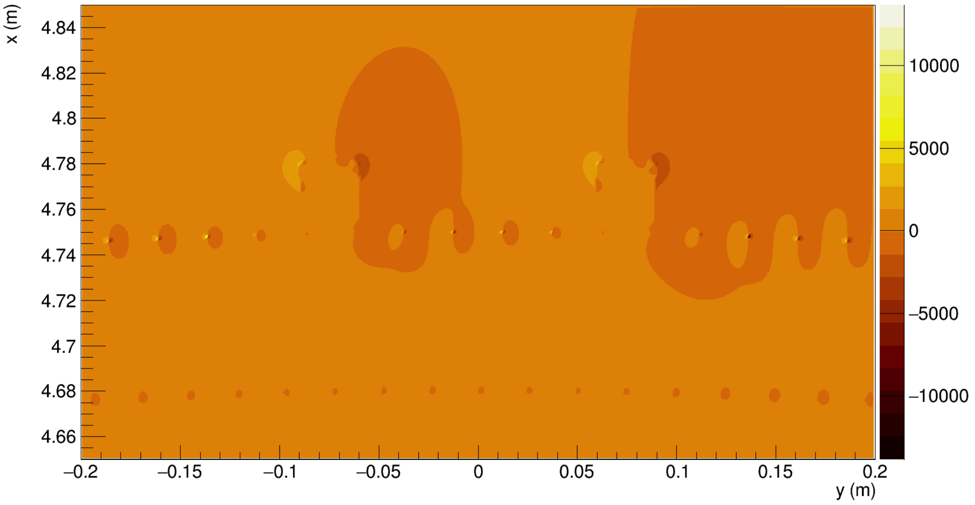

Figure A.13.: Electric field contour map at the vessel wall in the xy-plane. At global KATRIN main spectrometer coordinates $-0.2\,\mathrm{m} \leq y \leq 0.2\,\mathrm{m}$ and $4.65\,\mathrm{m} \leq x \leq 4.85\,\mathrm{m}$. The color indicates the electric field strength $\vec{E} \cdot \hat{e}_y$ in V/m.

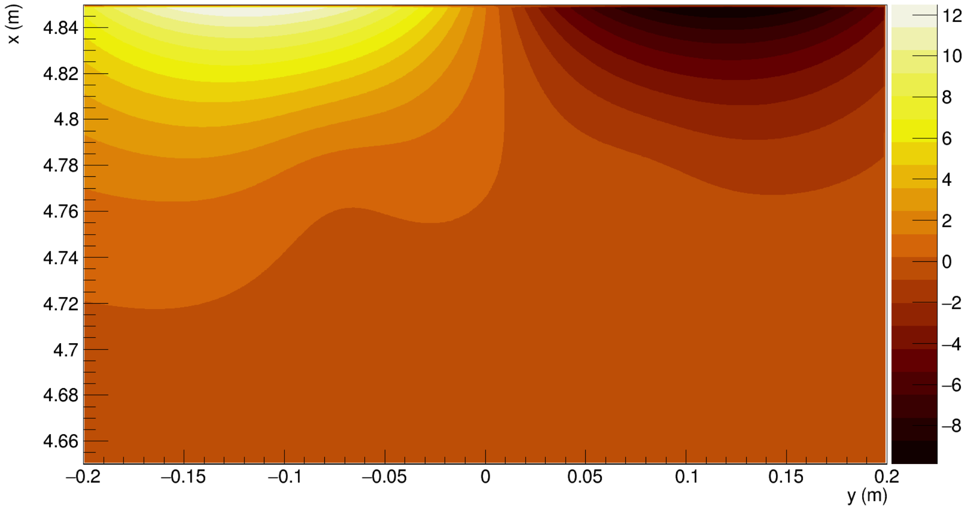

Figure A.14.: Electric field contour map at the vessel wall in the xy-plane. At global KATRIN main spectrometer coordinates $-0.2\,\mathrm{m} \leq y \leq 0.2\,\mathrm{m}$ and $4.65\,\mathrm{m} \leq x \leq 4.85\,\mathrm{m}$. The color indicates the electric field strength $\vec{E} \cdot \hat{e}_z$ in V/m.

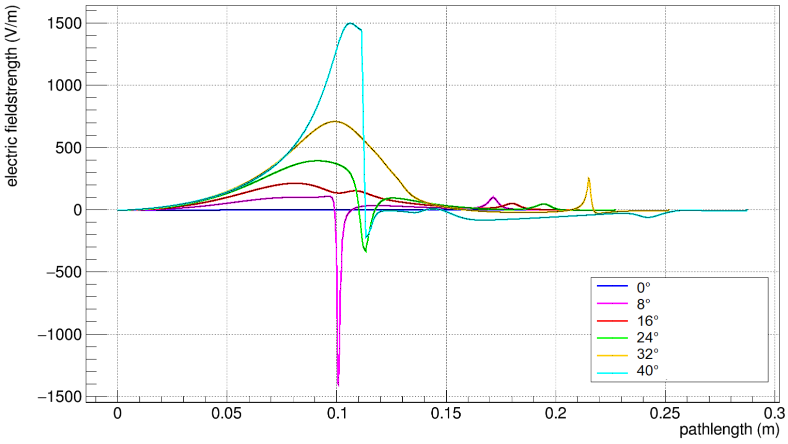

Figure A.15.: Electric field strength $\vec{E}_y$ distributions along straight paths started from $(x, y, z) = (4.85, 0, 0)$ directed into the volume under various polar angles $(0° \leq \theta \leq 40°)$.

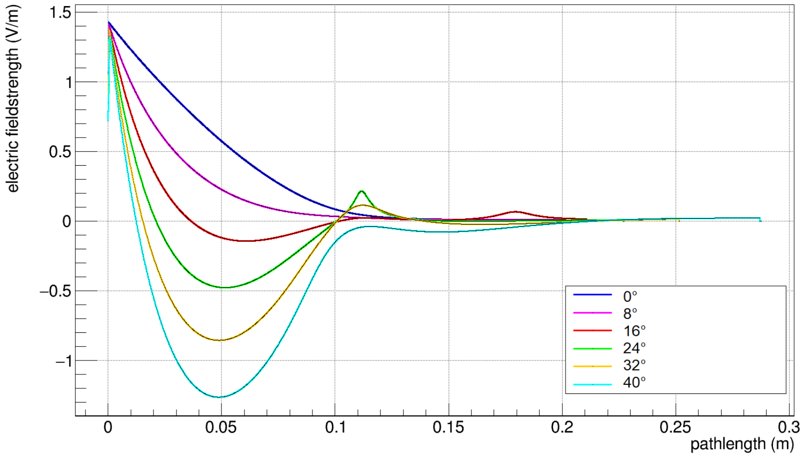

Figure A.16.: Electric field strength $\vec{E}_z$ distributions along straight paths started from $(x, y, z) = (4.85, 0, 0)$ directed into the volume under various polar angles $(0° \leq \theta \leq 40°)$.

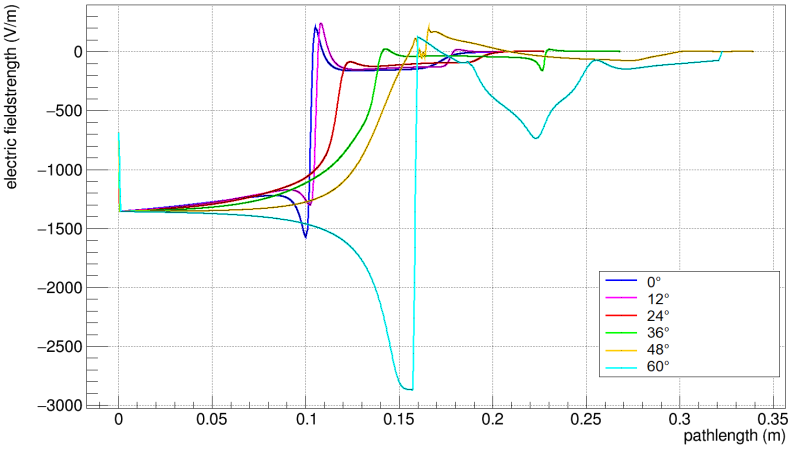

Figure A.17.: Electric field strength $\vec{E}_x$ distributions along straight paths started from $(x, y, z) = (4.85, -0.186, 0)$ directed into the volume under various polar angles ($0° \leq \theta \leq 60°$).

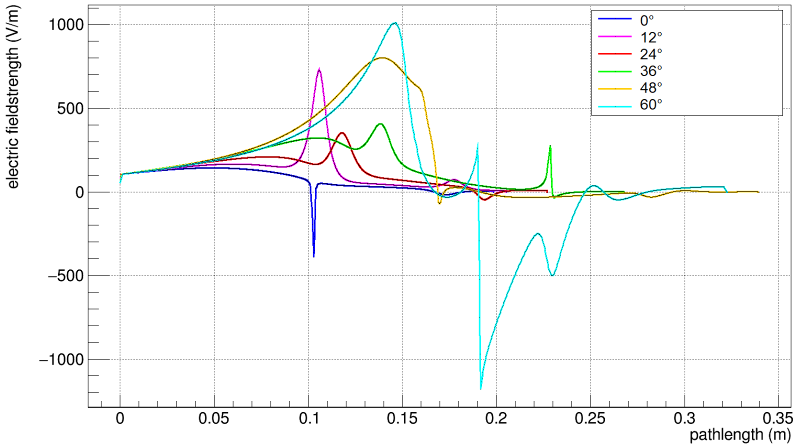

Figure A.18.: Electric field strength $\vec{E}_y$ distributions along straight paths started from $(x, y, z) = (4.85, -0.186, 0)$ directed into the volume under various polar angles ($0° \leq \theta \leq 60°$).

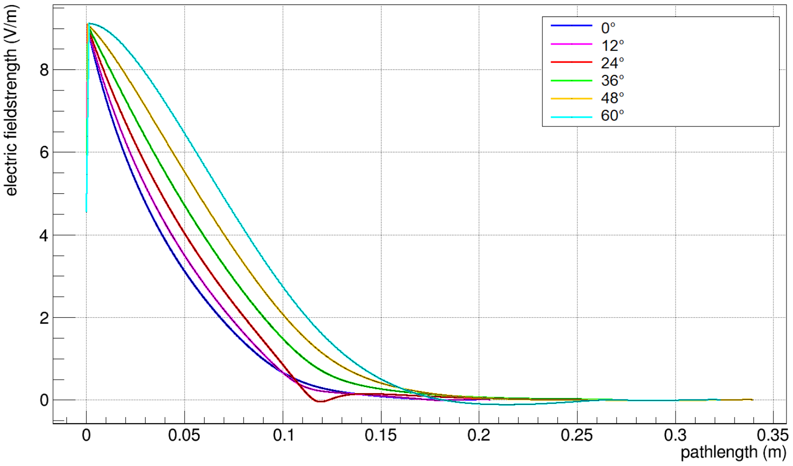

Figure A.19.: Electric field strength $\vec{E}_z$ distributions along straight paths started from $(x, y, z) = (4.85, -0.186, 0)$ directed into the volume under various polar angles ($0° \leq \theta \leq 60°$).

A.4. Autoionization

Table A.6.: Energies and assignments of atomic autoionizing states taken from Willis *et al.* [180]. Roman letters refer to peak labels in fig. 4.10b. Primes and double primes refer to the (^2D) and (^2P) core, respectively.[182]

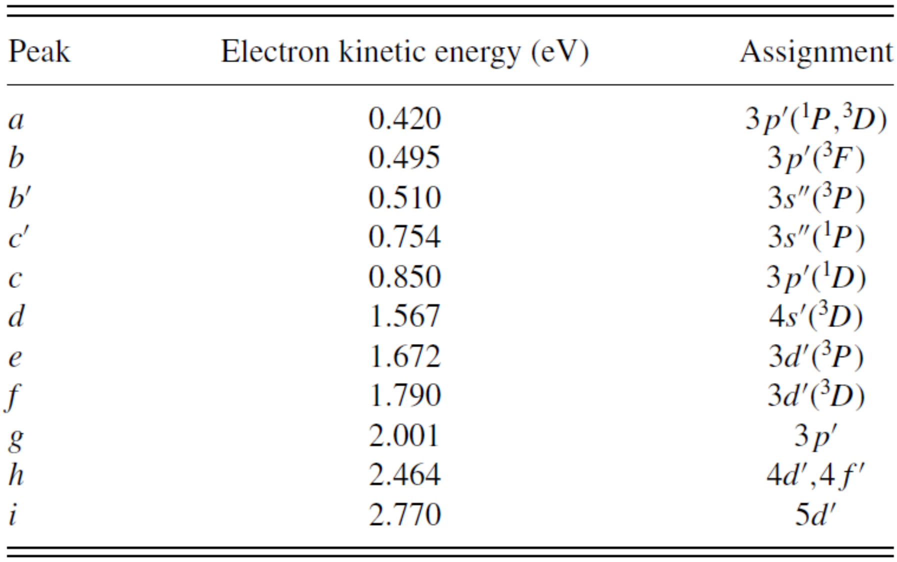

Peak	Electron kinetic energy (eV)	Assignment
a	0.420	$3p'(^1P,^3D)$
b	0.495	$3p'(^3F)$
b'	0.510	$3s''(^3P)$
c'	0.754	$3s''(^1P)$
c	0.850	$3p'(^1D)$
d	1.567	$4s'(^3D)$
e	1.672	$3d'(^3P)$
f	1.790	$3d'(^3D)$
g	2.001	$3p'$
h	2.464	$4d',4f'$
i	2.770	$5d'$

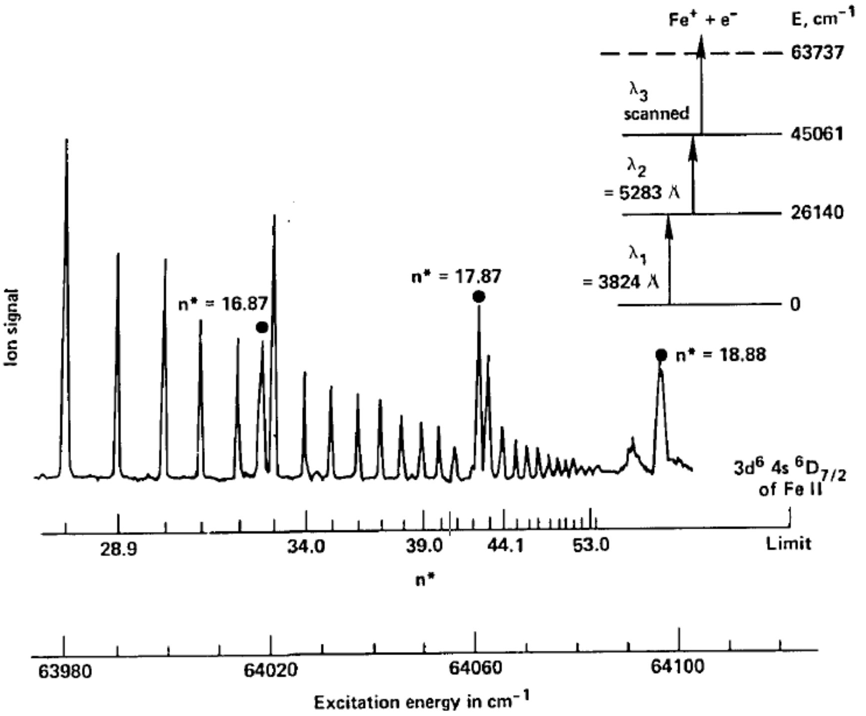

Figure A.20.: Autoionizing Rydberg series of iron from the 45061.327 cm^{-1} $3d^6 4s5s\ ^5D_3$ level that converges to the 384.77 cm^{-1} $3d^6 4s\ ^6D_{7/2}$ level of the ion. The excitation sequence is shown in the figure. The dots and effective quantum numbers 16.87, 17.87, 18.88 identify members of a series converging to the 667.64 cm^{-1} level of the ion.[185]

A.5. Radium-223 measurements

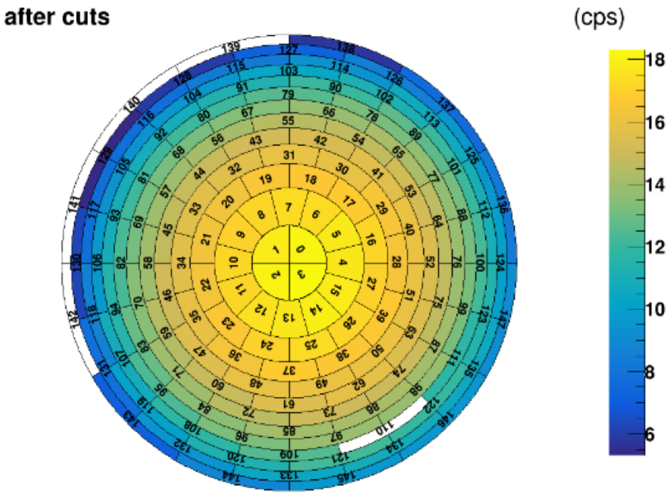

Figure A.21.: Pixel distribution of the rates after opening the valve to the ^{223}Ra source (implanted in steel). The rate of the whole detector is 1927 ± 0.5 cps. Pixel 110 and 139-142 are excluded due to anomalous behaviour.

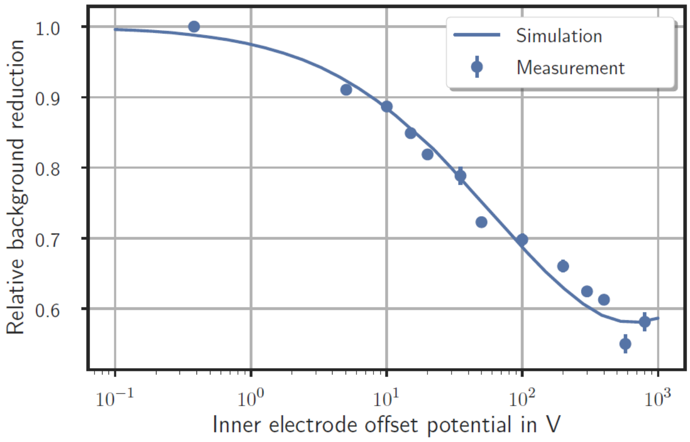

Figure A.22.: Relative background reduction as a function of the inner electrode offset potential.[128]

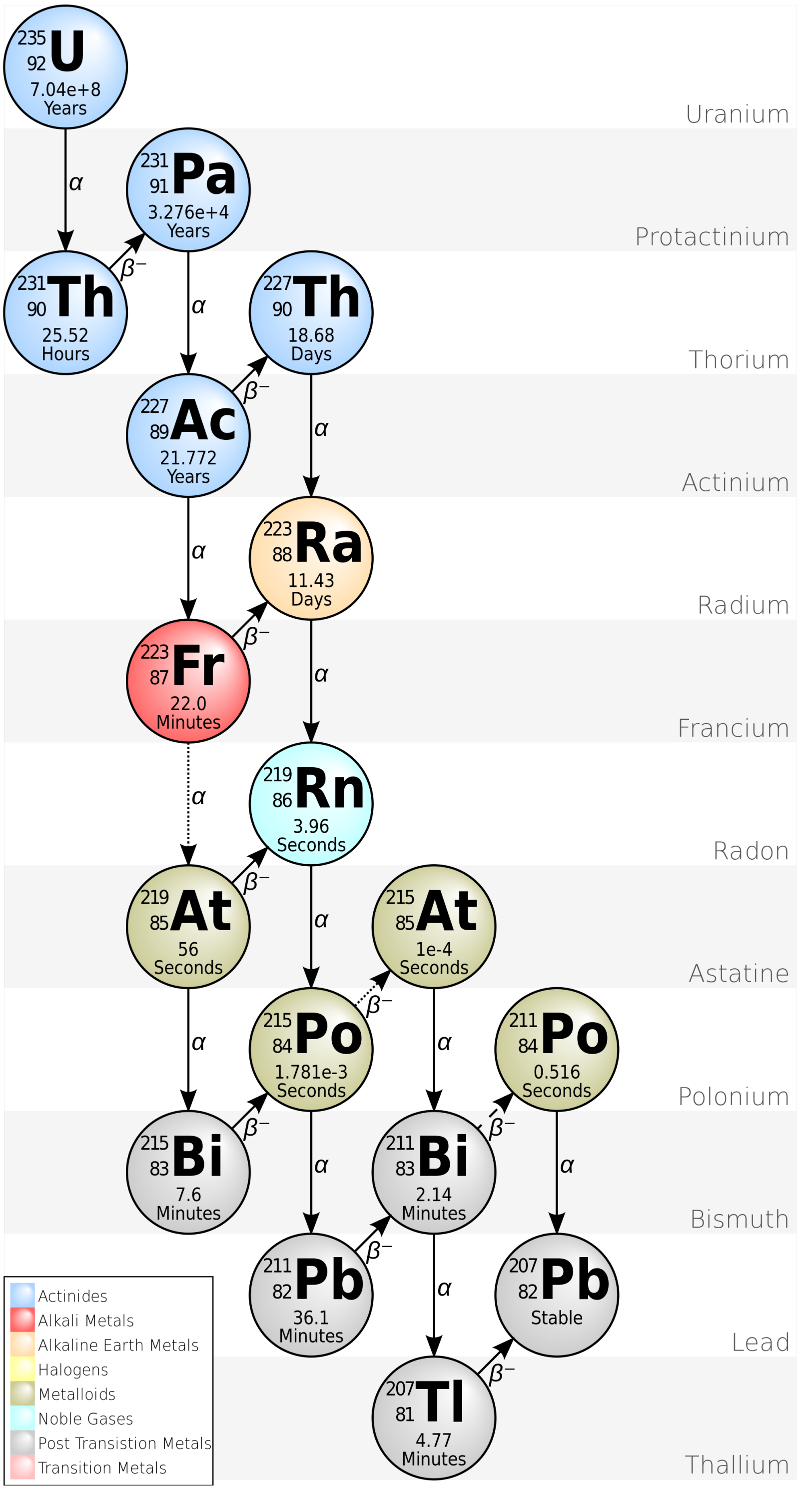

Figure A.23.: Decay chain 4n+3: Actinium series: Dashed arrow is decay mode with <1% probability. Dotted arrows are decay modes with <0.01% probability.[199]